A Study of Lateral and Longitudinal Tire Forces Produced on a Deformable Surface with Applied Traction and Braking

by

Capt. David Michael McIntyre

A thesis submitted to the Graduate Faculty of
Auburn University
in partial fulfillment of the
requirements for the Degree of
Master of Science

Auburn, Alabama
May 10, 2015

Lateral tire forces, Deformable terrain, Camber,
Tire friction ellipse

Approved by

Peter Jones, Chair, Woltosz War Eagle Motor Sports Professor of Mechanical Engineering
David Beale, Professor of Mechanical Engineering
David Bevly, Albert J. Smith, Jr. Professor of Mechanical Engineering
Song-yul Choe, Professor of Mechanical Engineering

Abstract

An investigation into the effects that changing tire characteristics have on the production of lateral and longitudinal tire forces was conducted on a test wheel that was subjected to external traction and braking forces. The test tire's slip angle, camber, inflation pressure and normal load were adjusted as the test wheel was run over a prepared piece of deformable test terrain consisting of a fine particle, remolded clay. Force data was collected using a series of load cells and tire angular velocity was collected from a Hall Effect senor and encoder wheel. The data was analyzed and several conclusions were reached about the effects that the tire characteristics have on both lateral and longitudinal force production. Tire friction ellipses were also created using the collected data to provide a more complete picture of the tire's performance during combined slip conditions i.e. a vehicle maneuvering with applied traction.

Acknowledgements

I would like to thank my family for their love and support during the time it took to complete this study and degree. I would like to especially thank my brother Joseph for his help in making my test machine a reality. I could not have completed it without him. I also want to thank my lovely wife Veverly for her love, support, and understanding during the long days and nights it took to complete this project. I know I came home very late sometimes, but she was always there to greet me. Finally, I would like to thank Dr. Peter Jones and the students of the War Eagle Motor Sports Teams for the use of their tools, tires, and facilities. The comments on my machine design and experiment procedures by Dr. Jones, Garon Griffiths, and others were most helpful and appreciated. I hope the findings prove useful and support many more new and exciting research endeavors at Auburn University.

Table of Contents

List of Tables

List of Figures

List of Symbols

S - Slip ratio (%)

V_v - Vehicle speed-over-ground (ft/sec)

V_w - Longitudinal wheel velocity (ft/sec)

r_e - Effective rolling radius (ft)

Ω - Angular velocity of the driven wheel (rad/sec)

Ω_o - Angular velocity of the un-driven wheel (rad/sec)

F_x - Longitudinal tire force (lbf)

F_y - Lateral tire force (lbf)

F_z - Normal force on the tire (lbf)

F_R - Rolling resistance (lbf)

M_x - Overturning moment (ft·lbf)

M_y - Rolling resistance moment (ft·lbf)

M_z - Aligning torque (ft·lbf)

γ - Camber angle (deg)

α - Slip angle (deg)

μ - Coefficient of friction

σ - Normal stress (lbf/sqft)

τ_{max} - Maximum shear stress (lbf/sqft)

α_f - Angle of the failure plane (deg)

c - Cohesion (lbf/sqft)

φ - Friction angle (deg)

p - Ground pressure (lbf/sqft)

b - Tire/Track width (ft)

k_c - Cohesion modulus of soil deformation

k_φ - Frictional modulus of soil deformation

n - Exponent of soil deformation

z - Sinkage (ft)

T_G - Total applied tire force (lbf)

T_N - Net force causing forward motion (lbf)

$MR_{terrain}$ - Force lost due to terrain deformation (lbf)

A - Tire contact area (sqft)

ω - Hall effect sensor pulse count

N - Number of teeth on the encoding wheel

a - Gear ratio

P_i - Probability value

S_E - Standard error

Chapter 1. Introduction

1.1 Motivation and Intent

Off-road vehicles are required to perform a variety of maneuvers on deformable surfaces with varying properties. The key component governing the vehicle's performance during these maneuvers are the tires. The tires are the only part of the vehicle that contacts the ground. Changes in a tire's inflation pressure, slip angle, camber angle, supported normal load, and amount of applied torque all have a contribution and varying effect on how the vehicle will behave on a given type of terrain. They all influence the amount of lateral force that a given tire will be able to generate. The generation of lateral force is what allows a vehicle to effectively corner and change course. A vehicle designer can use the knowledge of how lateral force will change in a given situation in order to better design key systems of the vehicle such as steering, suspension, and brakes.

The dynamics of lateral force generation have been studied most extensively on surfaces that are considered non-deformable like asphalt and concrete. The most significant research of lateral force generation of off-road tires are the studies conducted by Holloway, Wilson, and Drach [1] at the University of Maryland and by Krueger [2] at Auburn University. In both of these studies, the wheel was unpowered so all of the forces were observed at a slip ratio of zero. Significant findings from Holloway's and Krueger's research include that lateral force increases with slip angle in a manner similar to on-road cases [1], the lateral force increases with increasing tire contact area [2], and the surface characteristics affect tire force generation based upon normal load and contact patch area [2]. The data collected in these past studies will provide a useful starting point for comparing the results of tires tested while powered and unpowered.

The knowledge of how factors like camber angle and inflation pressure affect a vehicle on a deformable surface are just as important to designers of off-road vehicles as to those of on-road vehicles. The purpose of this research is to broaden the knowledge base of how the lateral force generation of a tire on a deformable surface will vary when subjected to different amounts of inflation pressure, normal load, slip angle, camber angle, and applied torque. This research will seek to provide a more complete picture of off-road lateral tire performance under traction, braking, and free rolling conditions. The first objective of the this study was to design an instrumented tire apparatus capable of measuring the variables needed to construct a plot of a friction ellipse of a tire on an off-road vehicle operated on a deformable surface. The second objective of this study was to construct a plot of a friction ellipse of a tire on an off-road vehicle operated on a deformable surface.

1.2 Background and Literature Review

1.2.1 Vehicle Dynamics

Tires are the critical link between any wheeled vehicle and the ground [3]. Tires can be thought of as deformable disks that support all of the vertical load of the vehicle as well as being the application site for the longitudinal and lateral forces acting on the ground. These forces are developed as torque is applied to the tires through the vehicle's transmission system. An important component of this process is the slip that develops between the tires and the ground. A basic depiction of these forces is shown in Figure 1. As the torque is applied to the axle, the tire contact patch begins to distort and applies a force to the ground. The force increases until it is of sufficient magnitude to overcome the friction of the surface which then causes the tire to slip and

thus roll in the direction of the applied torque. As long as the centerline of the tire is parallel to the centerline of the vehicle, the force the tire creates will be oriented longitudinally to the

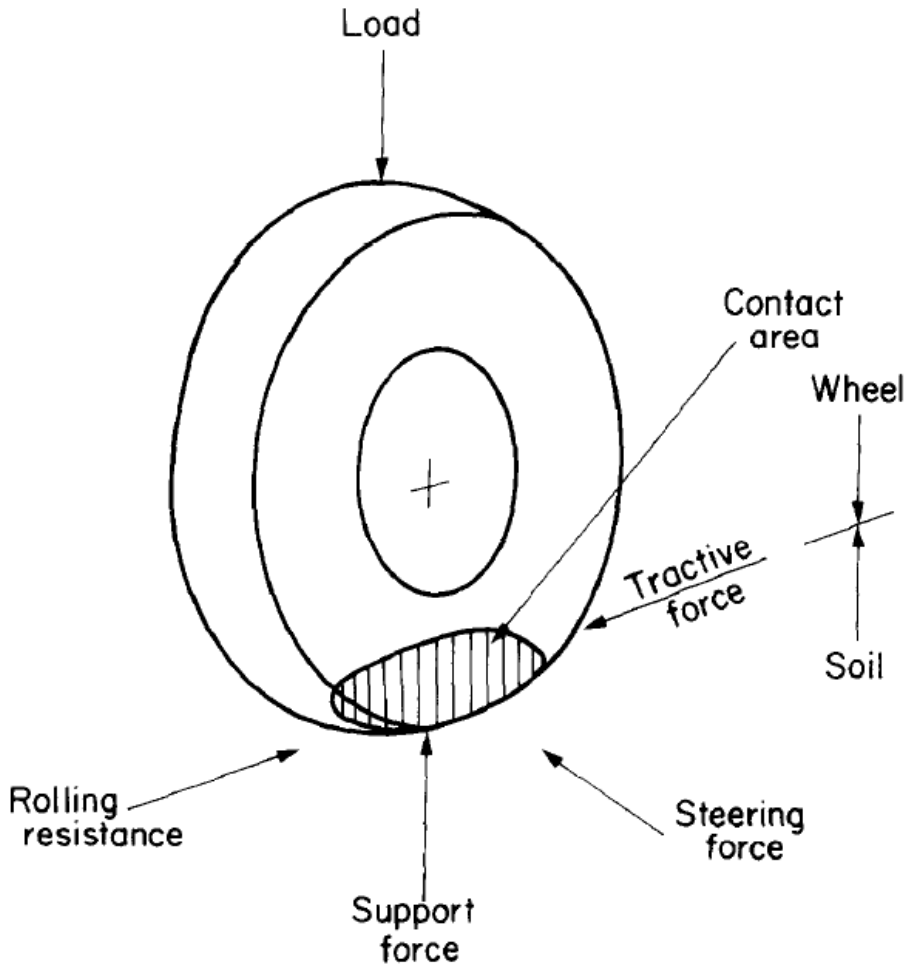

Figure 1. Forces acting on a tire as it rolls through soil [4]

vehicle. When the tire is turned using the vehicle's steering assembly, a slip angle is created between the direction the tire is pointing and the direction of vehicle travel. The slip angle causes the applied torque to deform the tire in both the lateral and longitudinal directions with respect to the vehicle. The additional lateral deformation gives rise to a force that is oriented at 90° to the vehicle's centerline. The lateral force that is produced by the tire causes the vehicle body to turn

in the direction of the force. The lateral force allows a vehicle to maneuver in the desired direction. An example of the tire deformation during straight line travel and normal cornering can be seen in Figure 2.

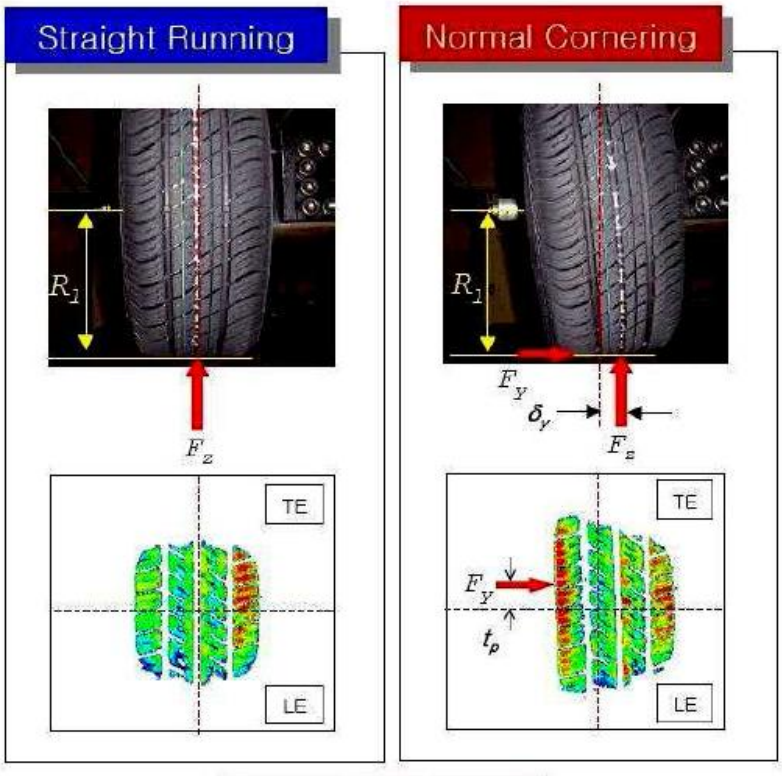

Figure 2. Tire contact deformation giving rise to the lateral force during cornering [5]

The standard vehicle coordinate system created by the Society of Automotive Engineers (SAE) will be used throughout this study. A diagram of this coordinate system is shown in Figure 3.

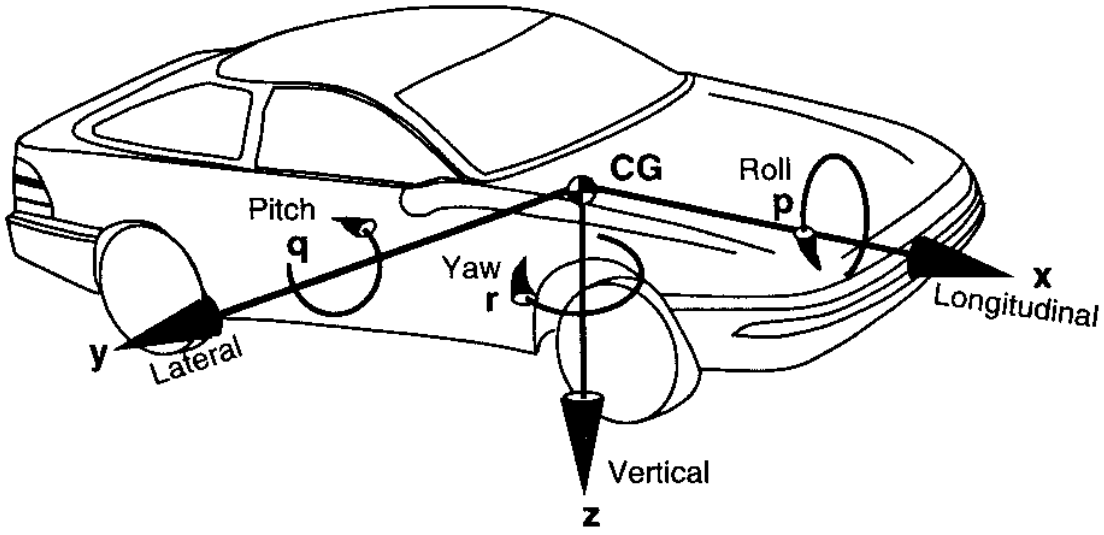

Figure 3. SAE vehicle axis system [3]

Figure 4 shows a standard tire force diagram with all pertinent quantities that will be used in this study. The diagram in Figure 4 has been expanded from Figure 1 to show all of the tire forces and moments in three dimensions. The factors quantities that will be investigated in this study are the longitudinal force (F_x), the lateral force (F_y), the normal force (F_z), the rolling resistance moment (M_y), the camber angle (γ), and the slip angle (α). The aligning torque (M_z) will be discussed briefly in the analysis of the test device. These study factors will be defined as having positive values as shown in Figure 4 [6].

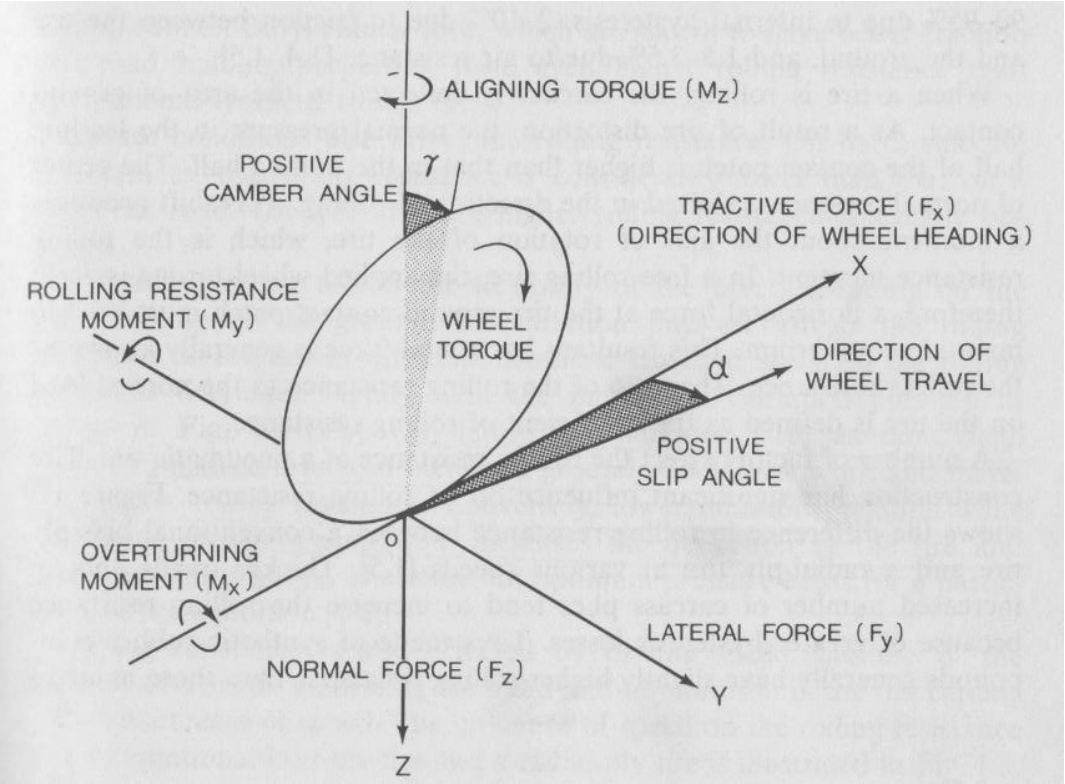

Figure 4. Tire force diagram [6]

This study will include both traction and braking forces that will be applied to the test tire. In order to account for these forces, it will be necessary to include the tire's slip ratio. The slip ratio is defined by the SAE as the difference between the longitudinal velocity of the tire and the vehicle. The slip ratio arises because of the distortion of the tire that is creating the longitudinal force. Applied torque causes the driven wheel to turn fractionally faster than an un-driven wheel because the driven wheel's contact patch is slipping relative to the ground in order to pro-

duce the longitudinal force that propels the vehicle. This relationship is expressed in the standard SAE form by Equation 1 [7].

$$S = \frac{V_w - V_v}{V_v} \quad \text{Eq. (1)}$$

where V_w is the longitudinal velocity of the wheel and V_v is the speed-over-ground of the vehicle. V_w can be expanded according to Pacejka [7] and Shoop [8] into

$$V_w = r_e \Omega \quad \text{Eq. (2)}$$

where r_e is the effective rolling radius of the tire and it is defined as

$$r_e = \frac{V_x}{\Omega_0} \quad \text{Eq. (3)}$$

and Ω is the measured angular velocity of the driven wheel. Ω_0 is the angular velocity of the un-driven wheel. The slip ratio will be positive when the tire is producing a traction force and it will be negative when the tire is braking. The effective rolling radius is distinct from the static tire radius caused only by the vehicle's normal load. The effective rolling radius will vary according to the angular velocity of the tire. The traction and braking forces are also influenced by the tire pressure, camber angle, contact area, and the tire's supported normal load. These characteristics will be more thoroughly explored in the following section.

The traction and braking force on a tire can be more useful as force coefficients by dividing each set of force data by the normal load on a tire. The resulting force coefficients are more useful than straight force values because they allow easy comparison of vehicles with different weights. Examples of plotted curves of longitudinal forces of traction and braking versus slip ratio on a hard surface can be seen in Figure 5 and Figure 6.

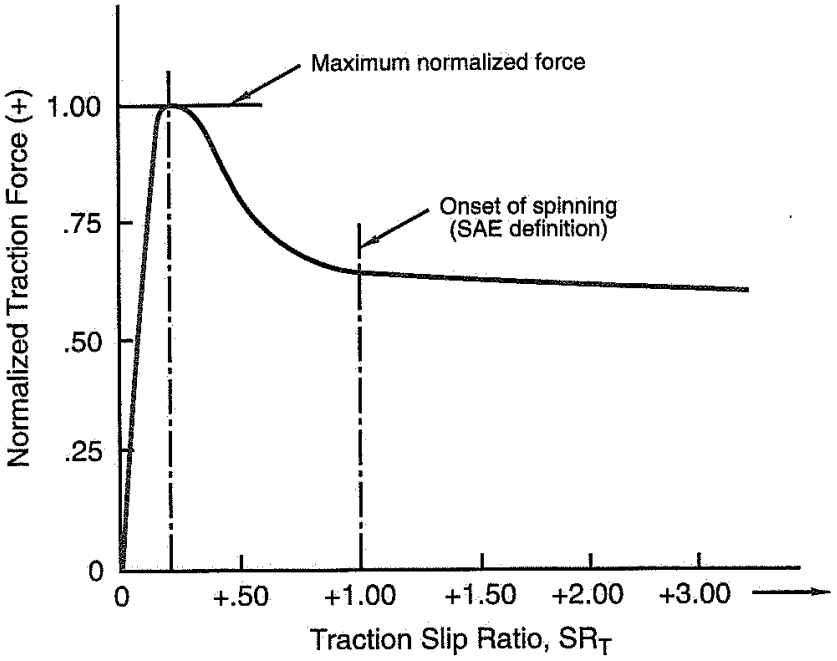

Figure 5. Traction versus slip ratio on a hard surface [3]

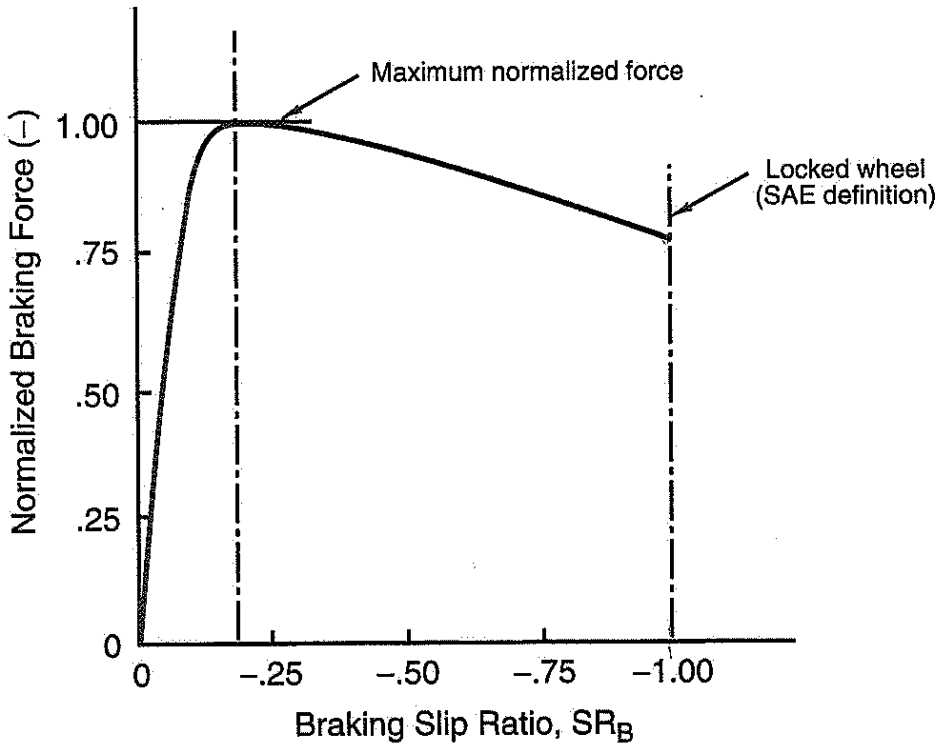

Figure 6. Braking versus slip ratio on a hard surface [3]

Both the traction and braking coefficients increase in a linear fashion up to a maximum at a slip ratio less than ±1.0 [3]. The force then decreases gradually as the slip ratio approaches ±1.0 at which point the wheel is spinning or locked during traction or braking respectively. Determination of the point of maximum force generation would be especially useful to a designer to ensure that maximum performance is obtained for a given configuration. The general behavior of traction and braking coefficients observed with non-deformable surfaces has also been observed on most deformable surfaces [4, 9]. The main difference is that on a deformable surface the maximum force and the slip ratio at which it occurs is greatly influenced by the shear strength and friction angle of the surface [9, 10]. The higher the shear strength, the more force that can be generated [2].

An understanding of the functions of lateral force on a tire is another critical part of this study. The lateral force generated by a tire is what allows a vehicle to maneuver. The application of a slip angle through a vehicle's steering assembly gives rise to a lateral force in the contact patches of the tires that causes the vehicle to yaw in the direction of the slip angle. Empirical data and a useful mathematical model that would allow a designer to accurately assess and predict a given tire's lateral force generation would be quite useful when optimizing a vehicle's performance. A general case of lateral force versus slip angle on a non-deformable surface is shown in Figure 7 [3].

Key aspects of Figure 7 to note are how the lateral force will increase linearly and then move into a transitional area before reaching a point of maximum lateral force at a certain slip angle. After this maximum is reached, the lateral force will then decline for increasing slip angles. Determination of the point of maximum lateral force is another key area for ensuring a vehicle can achieve its best possible performance.

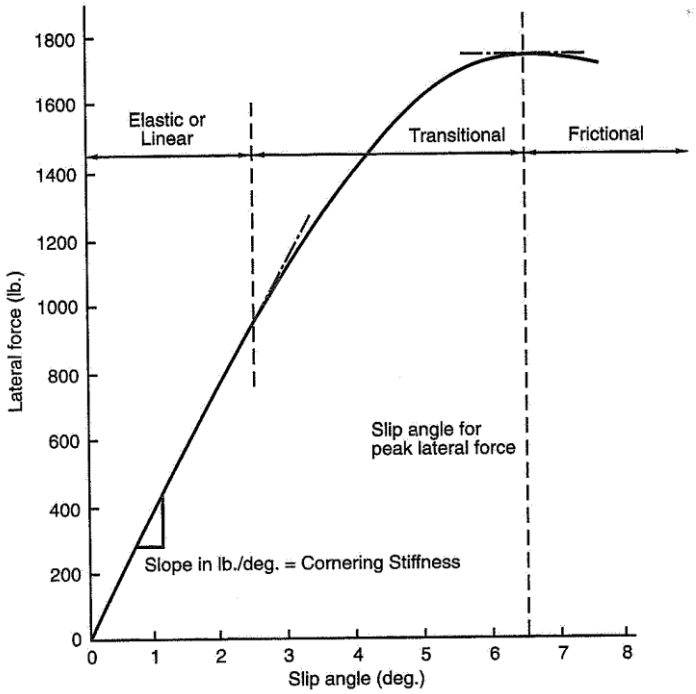

Figure 7. A general example of lateral force versus slip angle for a racing tire [3]

A linear, transitional, and maximum lateral force point also occur for tires on off-road surfaces [4, 9]. As was the case with traction and braking, the shear strength of the surface greatly impacts the amount of lateral force that can be generated on a given surface. Again, the higher the shear strength of the surface the more force that can be generated on it [2].

The friction ellipse, or tire force ellipse, is a useful way to combine the lateral and longitudinal force data into one chart of a vehicle's performance. The basic theory of the tire force ellipse is that there is a limited amount of traction that a tire can produce for a given normal load and operating surface conditions [5]. An example of the concept represented by the friction ellipse can be seen in a passenger car traveling on an icy road. The car can travel in a straight line with relative ease and can increase in speed. However, if the car attempts to maneuver at a higher speed, such as a lane change or turn, its tires will lose traction and begin to skid. The car will also lose traction if it attempts to accelerate quickly. The car though will still be able to perform

these maneuvers at lower speeds. The reason that the car can only perform maneuvers at speeds less than would be normally expected is because the surface characteristics are limiting the maximum lateral and longitudinal forces that can be produced by the car's tires for a given slip ratio and slip angle. When the car maneuvers, a resultant force is created that is a combination of the lateral and longitudinal force that the tires are producing. If this resultant force is higher than can be supported by the surface for the vehicle's normal load, the tire will lose traction and slide. The tire force ellipse is the maximum sustainable force envelope that is described by the friction ellipse. The supportable traction force is divided between the lateral and longitudinal force of the tire, which means that the theoretical maximum lateral and longitudinal forces cannot occur at the same time. When viewed graphically, the maximum resultant force will create a generally circular shaped performance envelope where the vehicle will be able to maintain traction. A good understanding of the tire's performance envelope can greatly improve a vehicle's design for performance and safety. Figure 8 shows a graphical representation of the simplest form of the friction ellipse model.

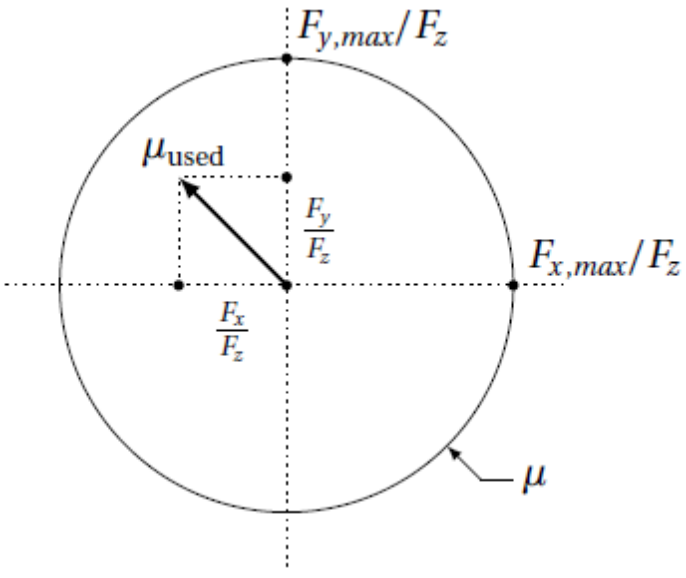

Figure 8. Idealized friction circle [11]

Through numerous experiments and observations, it has been determined that the tire performance envelope is generally elliptical in nature and is most influenced by the slip ratio, slip angle, and the frictional interaction between the tire and the surface [7, 12]. The most basic representation of this relationship is a circle that is defined by the following equation (Equation 4).

$$\mu F_{z,max} = \sqrt{\left(F_{x,max}\right)^2 + \left(F_{y,max}\right)^2} \qquad \text{Eq. (4)}$$

The circular representation assumes that the coefficient of friction is the same for both lateral and longitudinal motion of a tire. In reality, the coefficient of lateral and longitudinal friction are not equal and depend on surface properties, slip ratio, slip angle, and the normal load, which gives rise to the elliptical nature of the graph [12]. A general form of the friction ellipse can be expressed as shown in Equation 5.

$$\frac{F_y^2(\alpha,s)}{\mu_y^2 F_z^2} + \frac{F_x^2(\alpha,s)}{\mu_x^2 F_z^2} \leq 1 \qquad \text{Eq. (5)}$$

Equation 5 indicates that skidding will not occur as long as the inequality is true [12]. Figure 9 shows how the idealized friction circle under predicts the force limits for a tire. The dark curve shows the idealized friction circle and the dashed line represents the more realistic force limit indicated by experimental data collected by Salaani [12].

A more detailed version of the friction ellipse is shown in Figure 10. The graph in Figure 10 was taken from Milliken [3] and was constructed using data collected by Sakai [3]. The outer most line in the graph depicts the performance limit as shown in the simplified circle. The plots of constant slip angle and constant slip ratio were fit to the experimentally collected data. The data necessary to construct a friction ellipse graph for a given vehicle can be hard to find,

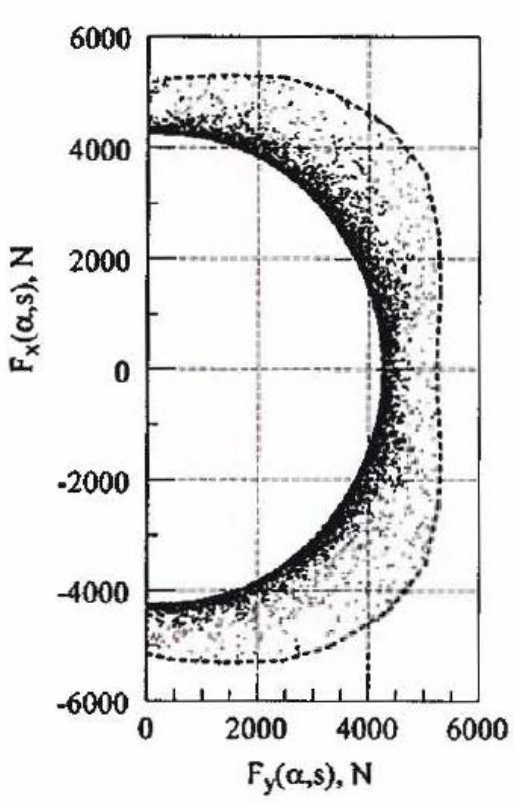

Figure 9. Idealized tire force circle underestimation of tire forces [12]

but once it is collected useful performance data for a variety of conditions can be extracted from it. The most useful data is found off axis which represents the combined lateral and longitudinal force for a particular slip angle and slip ratio. Reading the force data at a particular point on a graph shows what the expected lateral and longitudinal force will be at that slip angle and slip ratio. With enough data input, it can be possible to use the friction ellipse to predict the vehicle's performance for any combination of slip ratio and slip angle. Construction of a friction ellipse diagram for a particular vehicle would provide a designer great insight into the expected performance of a vehicle all the way out to the edge of the ellipse [3].

A key characteristic that has been missing in the previous research conducted with vehicles with off-road tires is the slip ratio caused when the tire is powered [1, 2]. The data collected

from a free rolling tire only describes a portion of the tire's performance envelope. A complete friction ellipse, and therefore a complete picture of a given vehicle's performance, cannot be constructed with only the forces recorded on a free rolling tire. The forces from a free rolling tire recorded at different slip angles, as was done by Holloway, *et al.* and Krueger [1, 2], will only give a designer the portion of Figure 10 that is near the x-axis. All of the points farther away from the x-axis will not be measured from a free rolling tire. The slip ratio is the critical variable that allows the farther away portions of the performance envelope to be constructed. As can be seen in Figure 10, the majority of the friction ellipse's data lies beyond the free rolling tire zone. The data contained beyond the free rolling tire zone is of importance to the designer because this region is where the resultant force will be located when the vehicle is maneuvering under power. Returning to the car on the icy road example, that vehicle's performance was being dictated by the amount of slip ratio that the tires were subject to. A reduced slip ratio is why the car could accelerate and turn slowly, but it could not do so at speed. The car's tires were creating a resultant force that was beyond the friction ellipse when higher slip ratios were applied. It is important for the designer to remember that vehicles will be subjected to maneuvering under power for a large portion of their operating time

The friction ellipse does have limitations however. Experiments have shown that the ellipse is just an estimate of the tire's total performance envelope [12]. The actual recorded data tends to indicate an elliptical shape but it is not perfectly symmetric. The coefficients of friction have been shown to change with slip ratio and will be different in the longitudinal and lateral directions [5]. It must also be noted that the studies discussed so far have been conducted on non-deformable surfaces. A deformable surface adds more variables in the surface characteristics that can greatly influence the amount of force a tire can generate [2].

1.2.2 Tire Characteristics

There are several key characteristics that influence a tire's performance. The first characteristic that will be considered is the tire's inflation pressure. Being pneumatic, inflation pressure can greatly affect how a tire behaves. At high inflation pressures, the tire will approach the behavior of a rigid wheel with only negligible carcass deformation [4]. From the works of Bekkar [10], El-Razaz [9], and Wong [6], a lower inflation pressure will increase the traction coefficient as the contact area and therefore the shearing surface area is increased. The work of Ageikin points towards an optimum tire pressure for a given surface that maximizes traction but keeps excessive tire wear due to carcass deformation to a minimum [13]. A reduction in tire pressure also increases the amount of soil compaction, so it will show the greatest effect on frictional soils [13].

The next tire characteristic that will be examined is camber. Camber is defined as the degree of tilt of a tire from the vertical. The effects of camber are most noticeable on tires that have a higher inflation pressure, a lower normal load and are cambered at eight degrees or less. The effects of camber on lateral force generation tend to taper off at angles higher than eight degrees and as the normal load increases [2]. The addition of camber to a given tire can help optimize the lateral force generation for a certain surface type.

The tire's contact area is another very important characteristic that will impact a tire's performance. The contact area is the only part of the tire in contact with the soil at a given time, so it is the area through which all of the longitudinal and lateral forces act. The contact area also controls the amount of shear and sinkage that will occur at the soil tire interface [10, 15]. According to Krueger [2] and Wong [15], the contact area will increase with increasing normal load and with decreasing inflation pressure.

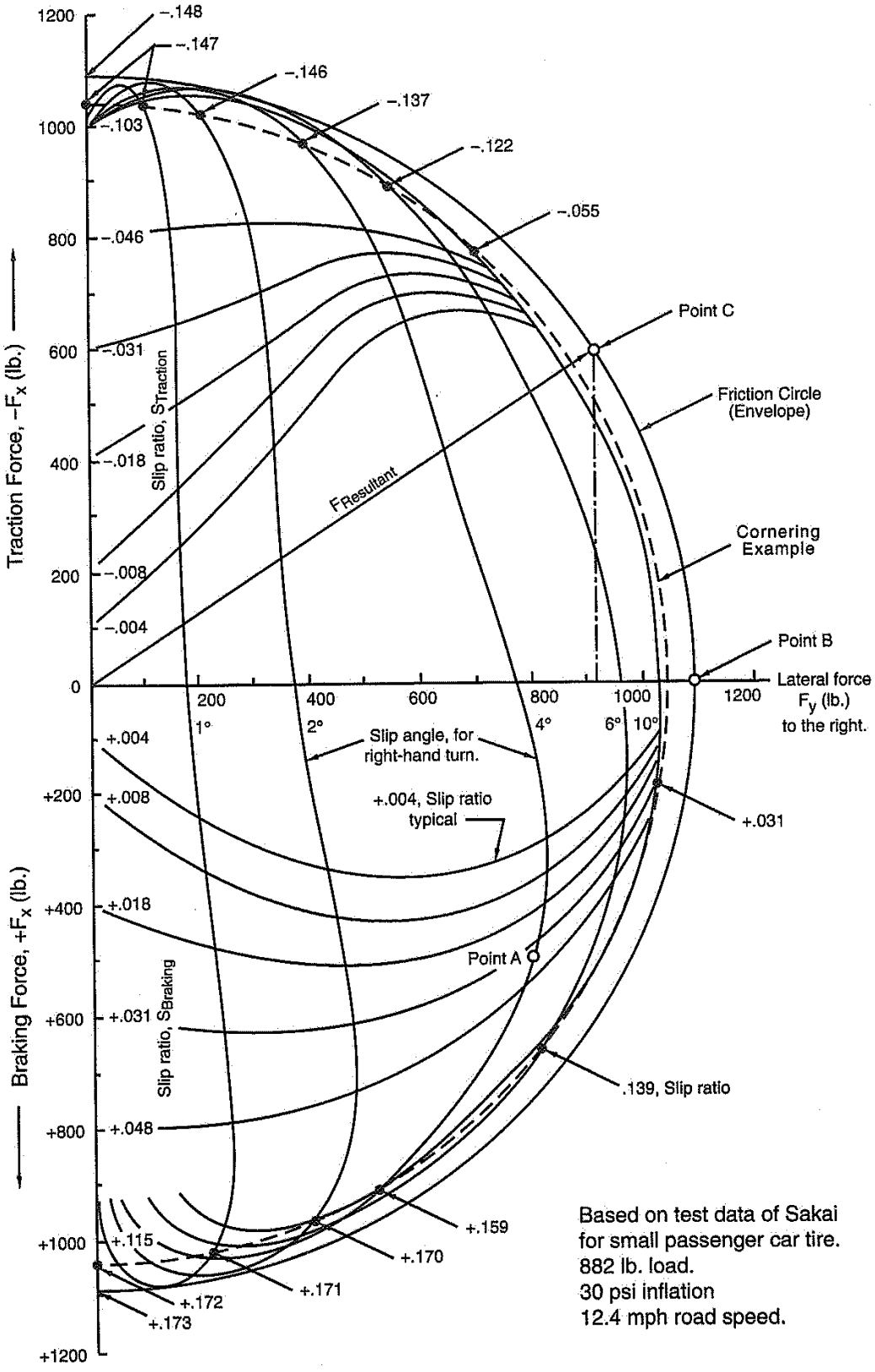

Figure 10. Example of a friction ellipse diagram [3]

The contact area is also influenced by the carcass stiffness of the tire as well as the tread design. The carcass stiffness affects the effective rolling radius which will in turn affect the traction or braking coefficients [13].

Tread design is especially important to off-road tires. The tread design will affect the overall carcass stiffness, but it will more importantly affect how the tire interacts with the surface. Since the surface is deformable, the soil can be compacted between the tire's lugs. Compaction can increase the amount of traction or braking produced especially on soft soils. The increase in forces is caused by the compaction of the soil increasing the shear stress that can be placed on it before the tire shears the surface particles [13].

The final tire characteristic that will be considered is normal load. Normal load is simply the amount of weight that the tire is supporting. Normal load has great influence on the contact area and effective rolling radius as the tire carcass is forced to spread out as the load that it is supporting increases. As stated earlier, changes in the tire's contact area will effect lateral and longitudinal forces as well as other parameters such as the depth the tire will sink into the surface and rolling resistance [13, 15]. An increase in normal load will also generally decrease the vehicle's lateral force and traction coefficients. A decrease in lateral force and traction coefficients is a phenomenon known as load sensitivity [1-4].

1.2.3 Operating Surface

An adequate understanding of operating surfaces is vital when designing off-road vehicles. Unlike asphalt or concrete surfaces, off-road surfaces are deforming as the tire rolls over them creating a highly dynamic interface between soil and tire where compaction and shearing are occurring simultaneously. The characteristics that control behavior of soils are important because ultimately they will influence the maximum traction that is available for acceleration, maneuvering and braking. One of the objectives of this study is to determine how surface characteristics combine with tire pressure, camber, normal load, and applied torque to affect the total force a tire can produce. In order to better understand, it is necessary to know key parameters of specified surfaces.

Cohesion of a soil is defined as the intrinsic attraction between soil particles. Soil cohesion depends upon soil particle size and particle material properties which effects the attraction forces between particles that hold the soil together [14]. The soil's cohesiveness will have a great impact on how much shear stress a surface can withstand before it fails. Cohesive soils like clay will plastically deform and will be able to generally support more shear stress than a non-cohesive frictional soils like sand [2].

The friction angle is defined as the orientation of the failure plane relative to the principle stresses [14]. An example of the failure plane and principle stresses is shown in Figure 11.

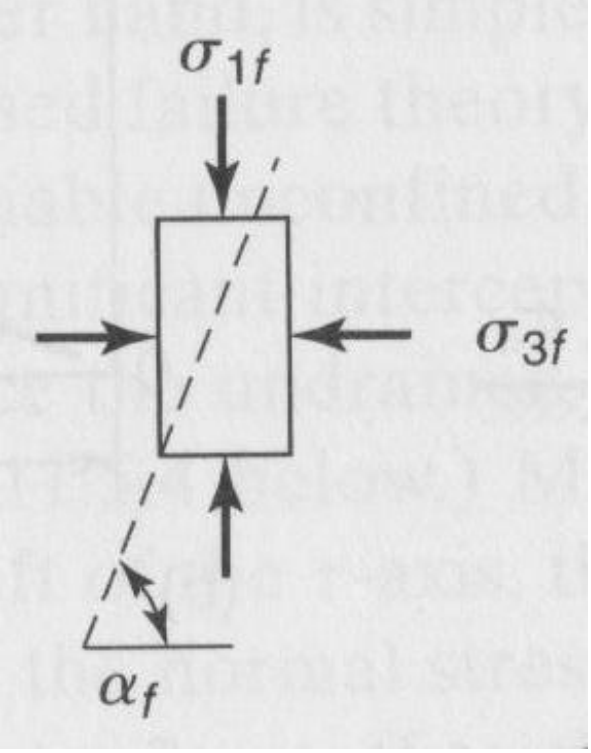

Figure 11. Principle stresses and the failure plane [14]

The friction angle affects both cohesive and frictional soils, but it is the most important property for a non-cohesive soil like sand. The friction angle will help define the strength envelope and give a designer the conditions under which the soil will shear.

When combined together, the cohesion and friction angle of a soil forms the Mohr-Coulomb failure criterion or strength envelope [14]. The strength envelope is defined by the following equation (Equation 6)

$$\tau_{max} = \sigma tan\varphi + c \qquad \text{Eq. (6)}$$

where τ_{max} is the maximum shear stress, σ is the normal stress, c is the cohesion, and φ is the friction angle. An example of the Mohr-Coulomb strength envelope is shown in Figure 12.

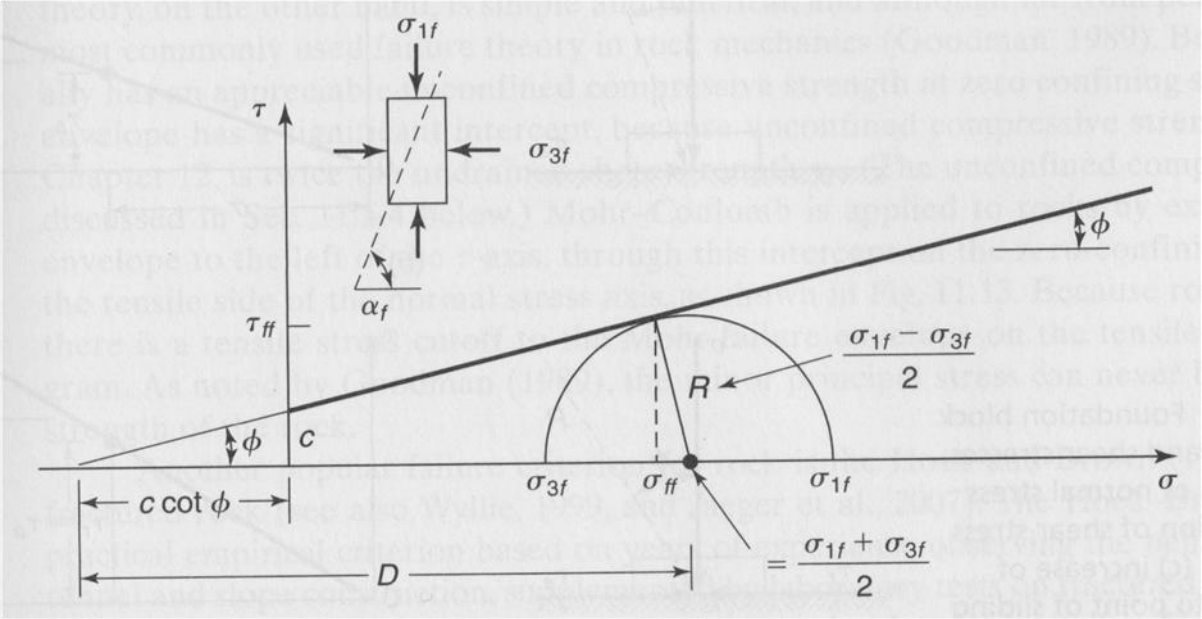

Figure 12. The Mohr-Coulomb strength envelope with a Mohr's circle at failure [14]

As can be seen in Equation 6, if a soil has a cohesion of zero the Mohr-Coulomb failure criterion will only be governed by the friction angle. Dry frictional soils like sand is only governed by the friction angle where the soil particles are only held together by the inter-granular friction. In most cases however, there will be at least some cohesion as even a small moisture content will cause the soil particles to have some degree of adherence to one another [14].

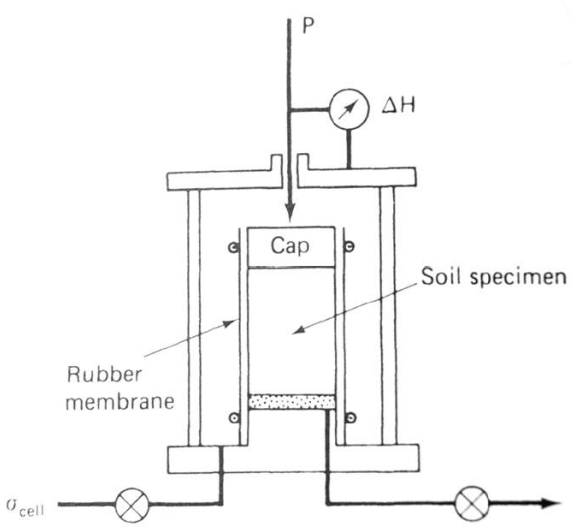

Figure 13. Diagram of a triaxial shear strength test [14]

There are several methods that have been created in order to determine the properties of a given surface. Some of the methods, for instance the triaxial shear strength test, are laboratory based and require careful collection of a soil sample to be tested [14]. The triaxial shear strength test involves taking a soil sample and placing it in a rubber membrane and then immersing the sample in a water filled chamber to provide a confining stress. An increasing normal load is then applied and recorded and the test ends when the soil sample develops a failure plane. A diagram of the triaxial test is depicted in Figure 13. The triaxial shear strength test is the standard soil strength test used in civil engineering projects. The main drawback to the triaxial test is that it cannot be performed in situ and in order to build up a characterization of a large area of terrain many samples have to be collected and tested. The triaxial test does however provide an important laboratory check on the accuracy of the in situ soil testing methods that will be described next.

The simplest of the in situ surface testing methods is the cone penetrometer as depicted in Figure 14 [16]. The cone penetrometer test consists of a simple metal cone with an attached

proving ring or load cell to show the amount of force necessary to push the cone into the soil. The data collected from the test can then be used to calculate the cone index which is the applied force divided by the area of the cone base. Several derivatives of the cone index can be obtained by analyzing the data collected with the cone penetrometer. For example, the quantity called the "vehicle cone index" is defined as the minimum cone index for a given surface that would allow a specific vehicle to traverse it without being immobilized due to sinking [15]. The example shows how the cone penetrometer is mainly designed to be used in vehicular mobility studies. The device is also simple to use and is easily transportable to any area that can be accessed by vehicle. However, the cone index is of limited value to a study involving tire force generation. The cone index does not allow for individual soil properties to be easily extracted from it and it has been shown by Wong [15] that the assumptions required to extract the soil strength properties make their accuracy suspect. The cone index's best use is mainly for fast "go/no-go" tests for construction or military operations in undeveloped areas.

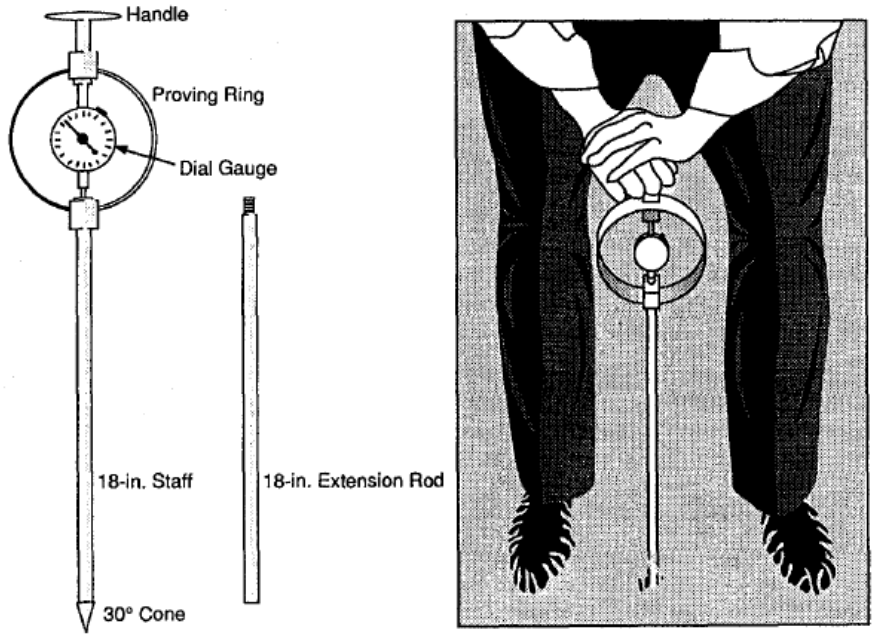

Figure 14. Cone penetrometer [16]

A more advanced technique for determining soil properties is the Bekkar Value Meter or bevameter. The bevameter is a device developed by M.G. Bekkar [10] that sought to better simulate the tire soil interaction by incorporating both a compression and a shearing test. The first part of the bevameter test is a plate sinkage test that records the applied pressure and the depth that a metal plate is pressed into the test surface. The second part of the test is a shearing test that uses a shear annulus that is pushed into the surface with a known normal load and then the amount of torque necessary to turn the annulus is recorded. The results from these two tests combined with Equation 7 below developed by Bekkar [10] allows for the soil strength properties of a surface to be extracted and the Mohr-Coulomb failure criterion for the surface to be determined. An example of a bevameter test setup is shown in Figure 15. A close up of the shear annulus is shown in Figure 16.

$$p = \left(\frac{k_c}{b} + k_\varphi\right) \cdot z^n \qquad \text{Eq (7)}$$

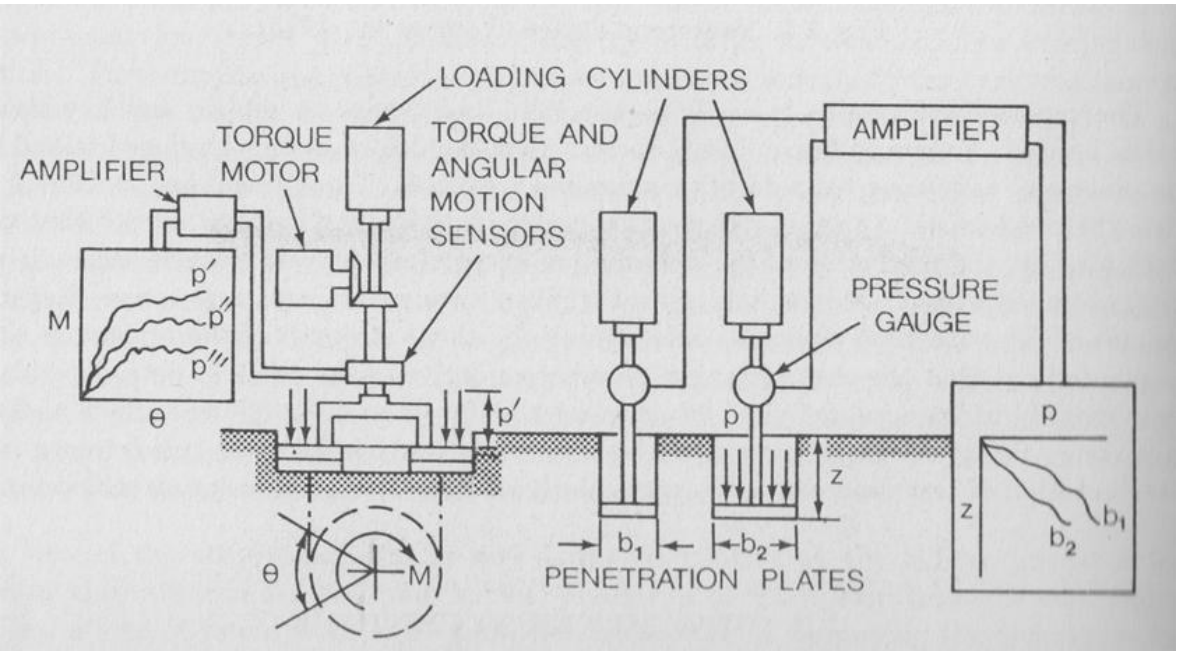

Figure 15. Schematic of a Bevameter [15]

The bevameter test is not without its drawbacks though. The best results are obtained from the test if the diameters of the pressure sinkage plates and the shear heads are matched to the diameter of the tire contact patch on a specific vehicle [15]. The diameters of the plates will have a great influence on the values that Bekkar's equations will produce. The requirement to match diameter limits the applicability of the results to vehicles that are of similar size with similar tires. The bevameter test also treats the sinkage due to the normal load and the shearing of the surface as occurring independently of one another.

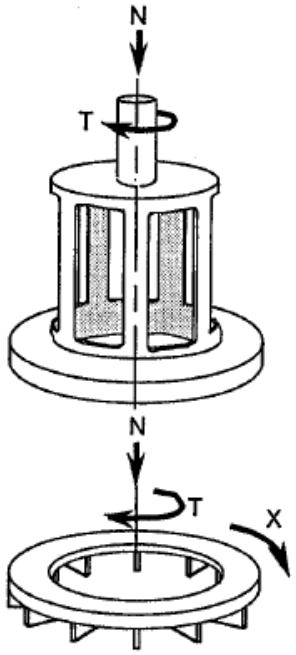

Figure 16. Diagram of a shear annulus [16]

As was shown by Ageikin [13], the process of compression and shearing of the surface is quite complex with varying amounts of compression and shearing occurring simultaneously. One does not get a good simulation of the process by testing compression and shearing independently. Karafiath and Nowatzki pointed this out in their work [17]. Karafiath and Nowatzki noted that

since the plate sinkage test does not induce any shear stress as a vehicle tire would, the pressure-sinkage relationship comparison between the two cases is inherently unequal. They contend that the smooth exponential relation created by Equation 7 is purely coincidental or the result of after the fact manipulation of the sinkage parameters. It is also important to note that the pressure-sinkage curves for different sized plates will cross over one another which can result in the parameter of k_c becoming negative which is physically impossible. Also, Karafiath and Nowatzki found that the shear annulus portion of the bevameter test can sometimes produce false readings if the bottom plane of the annulus and the actual failure plane of the soil do not coincide. Shoop [16] showed that the results of the bevameter tests do not follow the same trends as the results obtained from triaxial shear tests. As can be seen in Figure 17, while the data from the bevameter test (the shear annulus line in this case) does cross the data from the triaxial test, it does not follow the same trend and it indicates a much more rapid increase in the shear stress than is actually occurring [16].

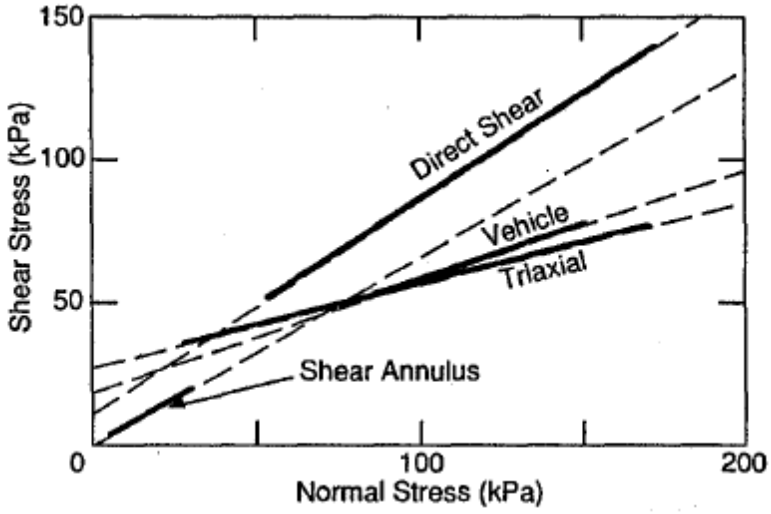

Figure 17. Results of Shoop's comparison of various methods of obtaining soil shear strength [16]

A better alternative to using independent shear and sinkage tests to determine the soil properties, is to use an instrumented wheel. The wheel is outfitted with a Hall Effect sensor to measure wheel speed, a motor to apply a torque, and load cells to measure the force that the wheel is exerting on the ground. Data of speed, torque and exerted force combined with a measurement of the wheel's contact area allows for the stress at the soil tire interface to be determined. Once the stress is determined, it is possible to construct the Mohr-Coulomb failure criterion for a given surface. This method can be referred to as the "gross traction method" as it takes into account both the force being applied to the wheel and the actual force that the tire is generating on the ground. The gross traction method was first described by Shoop [18] for use in an Army Corps of Engineers vehicular mobility study. Equation 8 shows the basic principle of this method.

$$T_G = T_N + MR_{terrain} \quad \text{Eq. (8)}$$

T_G is the total force applied to the system, T_N is the net force causing forward motion of the vehicle and $MR_{terrain}$ is the force that is lost due to the deformation of the terrain. T_G is known from the total applied torque from the motor turning the wheel, T_N is recorded from the load cell readings and $MR_{terrain}$ is found by finding the difference between T_G and T_N. Once $MR_{terrain}$ is calculated, the stress that is causing terrain deformation can be determined by dividing $MR_{terrain}$ by the area of the tire's contact patch. Terrain deformation stress can then be used to create the Mohr-Coulomb failure criterion that allows the surface to be characterized based on cohesion and friction angle. The gross traction method helps to take into account the dynamic nature of the compression and shear at the tire soil interface since the data from this method is coming from an actual spinning tire. The method can even be used to account for carcass deformation as a separate quantity if it is deemed significant [19].

1.3 Purpose and Contribution

The purpose of this research was to expand the knowledge base of how an all-terrain vehicle's (ATV) tire lateral and longitudinal forces generation was affected by changes in the tires' slip angle, camber angle, inflation pressure, and normal load while subjected to traction and braking forces. The study was undertaken with the use of an instrumented wheel using a Hall Effect sensor to record angular velocity and load cells to record the force exerted on the test apparatus. The speed-over-ground of the vehicle was recorded through the use of the Global Positioning System (GPS). The surface properties were calculated using the gross traction method as described by Shoop [18] and were intended to overcome the difficulties described by Karafiath and Nowatzki [17]. Applied traction and braking were supplied by an attached electric motor. This research sought to find usable data on lateral and longitudinal forces for the ATV tire to allow a friction ellipse and accurate performance characteristics to be formulated. Determination of the entire friction ellipse was important because off-road vehicles spend a significant amount of time with combined slip conditions affecting the driven and un-driven wheels as the vehicle maneuvers across the terrain and around obstacles. The driven wheels are the most affected by the combined slip conditions because of the applied torque effects, but the un-driven, steered wheels are also affected because they are subject to both drag and lift as the vehicle maneuvers. Finally, un-steered, driven tires can be put into combined slip conditions by the orientation of the central vehicle axis as it is moved around by rough terrain. The broader performance impact on a vehicle is much more readily apparent when plotted in terms of combined slip and the tire's traction limits for a given set of tire parameters. Performance data with slip and traction considered is exceedingly rare for off-road tires and this study was the first to include applied traction when examining the specific tire properties mentioned.

Chapter 2. Research Tools

2.1 Tire Test Apparatus

2.1.1 Development

The tire test apparatus is the central component in the collection of the force data from the tire. The main criteria that determined how the apparatus was designed were: the accurate collection of both lateral and longitudinal forces, adjustable slip and camber angles, controllable application of traction and braking torque, sturdy construction to allow testing on off road surfaces, accurate recording of tire angular velocity, one person operation, and minimal deflection of apparatus members under load to ensure accurate force readings.

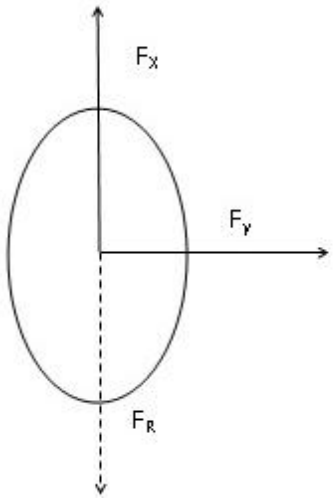

Figure 18. Forces acting through the tire's contact patch

The accurate collection of tire force readings was the most important function of the test apparatus as this information was one of the primary goals of the research. In order to effect accurate collection, a thorough understanding of the tire force application is necessary. As discussed in

Chapter 1, the forces of primary interest are the longitudinal and lateral forces that are created as the tire rolls. Figure 18 shows a simplified view of the forces created in the tire's contact patch.

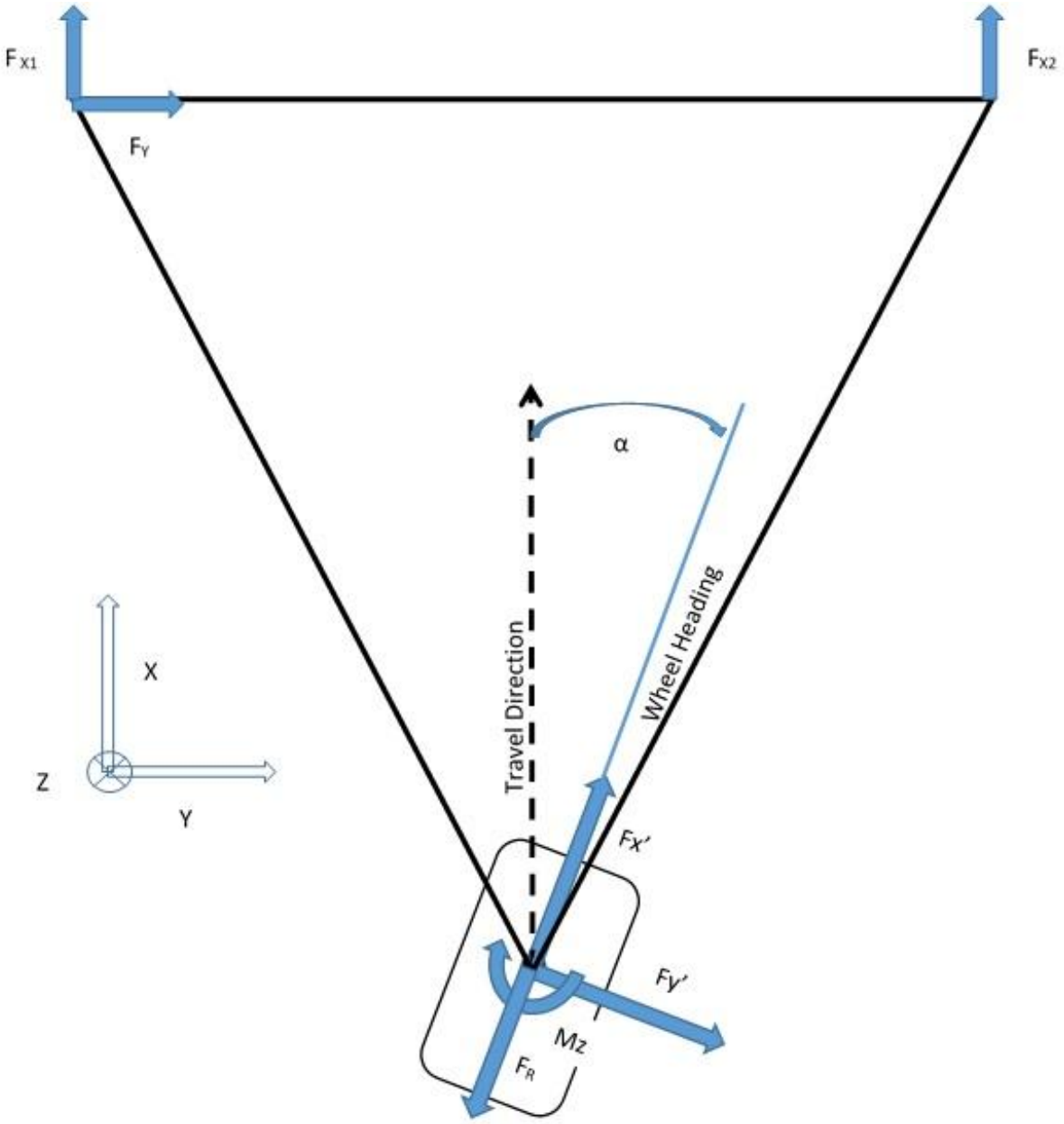

Figure 19. Tire test apparatus free body diagram

The collection process and data analysis will be simplified by limiting the test apparatus to a single wheel, so the force may be more easily resolved and the readings will not be compli-

cated by force transfer between two tires. The most logical place to locate the load cells for recording the forces is at the connection points where the test apparatus meets the tow vehicle. The load cells located at the connection points orients them along the main vehicle axes. The load cells oriented with the main vehicle axes allow the use of one simple coordinate transform to bring the forces into the vehicle's coordinates when a slip angle is applied to the wheel. A free body diagram showing the forces from the tire and their reactions on the apparatus frame is shown in Figure 19.

The basic design of the towed tire apparatus used in this study was adapted from the tire force device originally created by Holloway *et al.* [1] for the off-road tire experiment conducted at the University of Maryland. The University of Maryland apparatus consisted of a single wheel that was towed behind an ATV. The forces were recorded using analog proving rings oriented along the tow vehicle's longitudinal and lateral axes that were mounted at the interface between the apparatus and tow vehicle. A tire to be tested was mounted on a spindle attached to a hook arm which was connected to an A-frame that was in turn connected to proving rings. The position of the tire at the tip of the A-frame ensured that the forces that are being generated by the tire were transferred down the A-frame arms to the proving rings where they could be recorded. A picture of the University of Maryland device is shown in Figure 20.

The University of Maryland researchers' design was modified by Krueger [2] to incorporate load cells instead of proving rings. The use of load cells allowed a digital data collection system to be utilized. Krueger's A-frame with the three load cells, two longitudinally and one laterally mounted, formed the core of the device used in this study. Krueger's basic design has been well tested [1, 2] and capable of recording loads of up to 500 lbf (2224 N). The A-frame and load cell configurations are depicted in Figures 21 and 22.

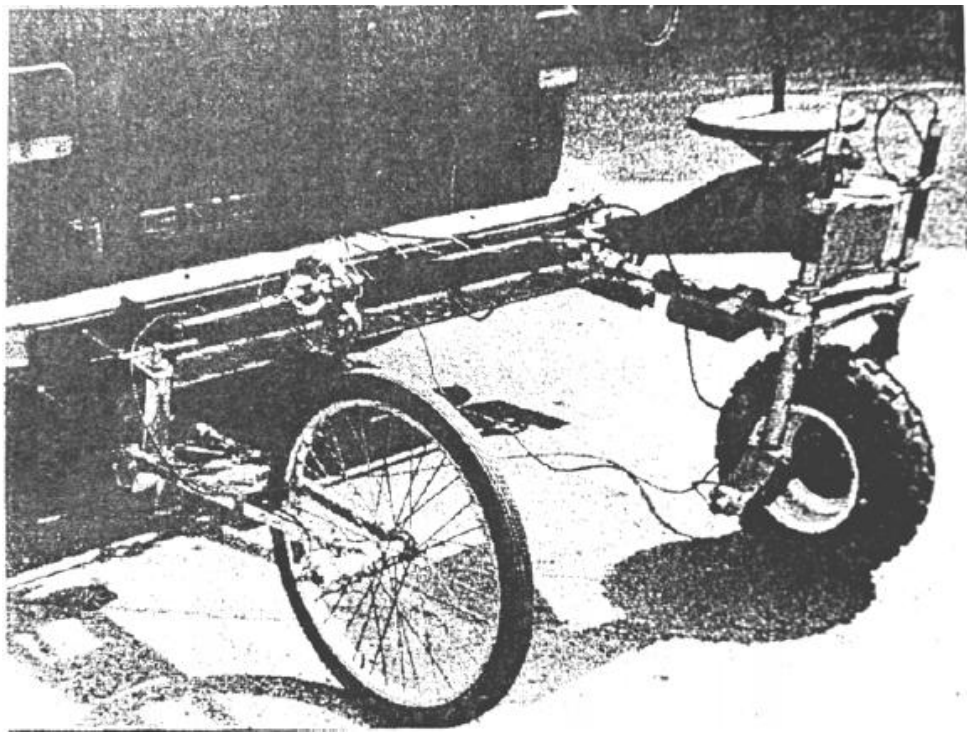

Figure 20. Tire test apparatus used by researchers at the University of Maryland [1]

Figure 21. Rendering of the test apparatus A-frame

The next aspect to be considered is the adjustment of the tire's camber and slip angles. In order to counteract the effects of the moments that can be produced by a tire especially when a slip angle is applied, the angle adjustments must be robust and able to maintain their setting when under load. The self-aligning torque will have the most impact on the slip angle adjustment. Self-aligning torque will make the tire return to a zero slip angle if not mitigated. The slip

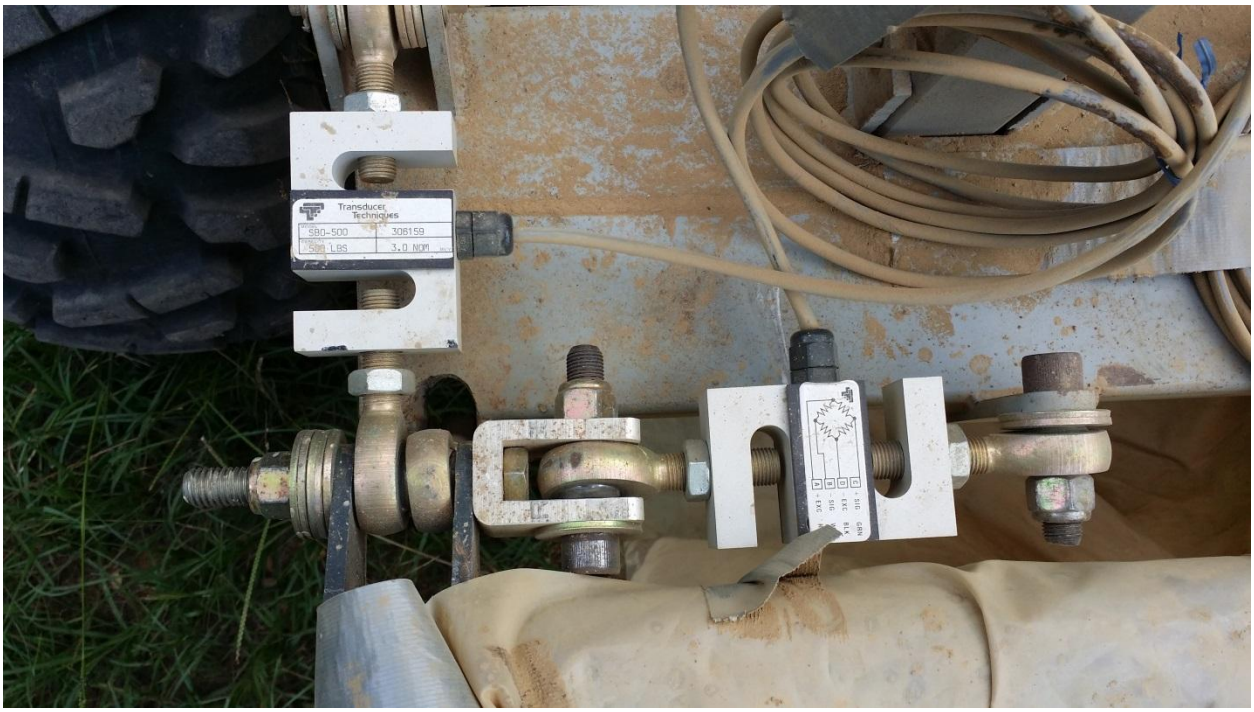

Figure 22. Longitudinal and lateral load cell configuration

angle adjustment is accomplished through the use of a series of graduated holes drilled in a metal plate. The holes increment the slip angle by 5 degree steps. An SAE grade 8, 0.5 in (1.27 cm) bolt is inserted through the hole at the desired angle and into a receptacle that is attached to the hook arm. The bolt can withstand shearing loads of up to17868 lbf (79476.864 N), which is well in excess of the maximum expected loads of 400 lbf (1779.2 N) and the maximum recordable load of 500 lbf (2224 N). A 0.25 in (0.6 cm) A36 mild steel plate was used to fabricate the slip

angle adjustor. A36 steel has a minimum yield strength of 36000 psi (248312.5 kPa) and a minimum tensile strength of 58000 psi (400059.1 kPa). The camber angle adjustment apparatus is constructed in a similar fashion to the slip angle adjustor. The primary concern for the camber angle adjustment is counteracting the overturning moment caused by the normal load no longer aligning with the centerline of the tire. The overturning moment will cause the tire to fall in the direction of the camber angle if it is not countered. The camber adjustment apparatus must also be able to support the static normal load as it is the attachment point between the A-frame and the tire hook arm. The maximum applied normal load is 270 lbf (1201.0 N) which can create forces in excess of 700 lbf (3113.6 N) due to the high instantaneous accelerations when the tire rolls over a large rock or micro-elevation change in terrain. The camber adjustment apparatus is made using a series of graduated holes to adjust camber ranging from 0 to 8 degrees positive camber. The holes are placed in two parallel 0.25 in (0.6 cm) A36 steel plates. A rectangular mild steel block was positioned at the top of the tire hook arm with three holes drilled in it that align with the holes in the parallel plates. The hook arm is secured in place with three 0.5 in (1.27 cm) grade 8 bolts. The three bolts can each support a maximum load of 17868 lbf (79476.86 N) which is well is excess of the 700 lbf (3336 N) loads that are expected. The main purpose for using three bolts is to prevent slippage and rotation of the hook arm when the tire is cambered. The University of Maryland device is capable of setting slip angles of up to 90 degrees and camber angles up to 20 degrees. Results reported by Holloway *et al*. [1] and by Krueger [2] showed that the most significant data for tire performance occurs at slip angles of less than 20 degrees and camber angles of 8 degrees or less. The design for the test apparatus for this study was changed accordingly with the camber angle adjustment stopping at 8 degrees. Reducing the overall travel of the tire hook arm ensures that a stable angle can be held when load is

applied to the device. A CAD rendering of the slip angle and camber angle adjustments apparatus is depicted in Figure 23.

Controllable application of traction and braking forces is needed to allow for the observation of tire forces under driven conditions. The design of this portion of the device is determined by the vehicle type that is being simulated. The vehicle that is being simulated is an SAE Baja all-terrain vehicle that uses a 22 in (55.9 cm) diameter wheel. Vehicles of this type typically use a drivetrain that is capable of propelling the vehicle between 30-40 mph (48-64 km/h) and have normal loads in the 500-750 lbf (2224-3113.6 N) range. From these parameters, it is possible to determine the necessary power that must be applied to the wheel in order to drive the tire at slip ratios from -1 to +1. Assuming a corner load of 150 lbf (667.2 N) for the average Baja car and a friction coefficient of the surface of 0.67, the maximum traction force that the tire can produce is 100 lbf (444.8 N). The maximum torque required on a 22 in (55.9 cm) wheel would then be 92 ft·lbf (124.7 Nm).

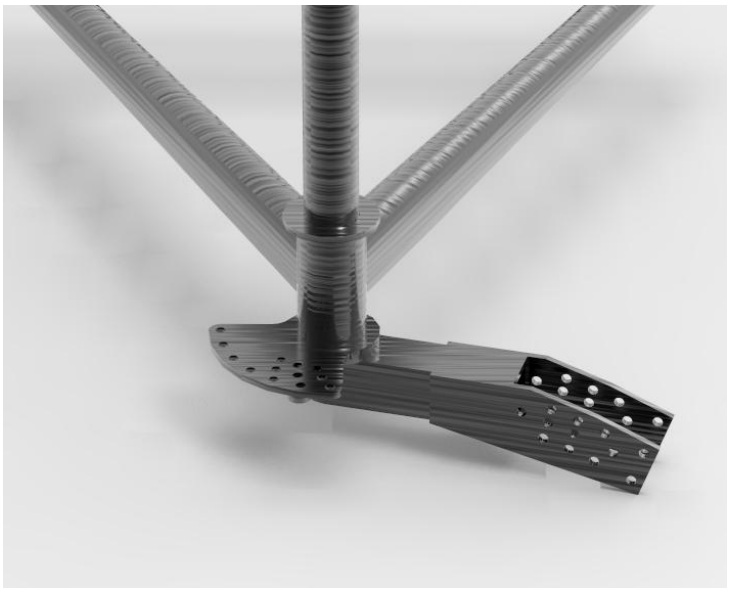

Figure 23. Rendering of the slip angle and camber angle adjustments

The vehicle has a top speed of 30 mph (48 km/h); therefore, the tire will rotate at 48 rad/s. The power input required to produce this force at 30 mph (48 km/h) is then simply the torque times the angular velocity which is 8 hp (6.0 kW). Now that a typical power requirement is known, an appropriate powertrain can be selected to cover the specified performance envelope. An electric motor and an internal combustion engine were both considered to power the wheel. Both could produce the required power output, but the electric motor was chosen because of its ease of control. The 8 hp (6.0 kW) Advanced Motors and Drives (AMD) DC series wound electric motor was chosen to provide the needed power. The motor operates on 48 volts with a maximum current draw of 400 amps. The specific model that was selected, the K91-4003, is a reversible motor so it could be used to apply traction as well as a braking force. A reversible motor eliminates the need for a separate braking system. The K91-4003 is also capable of supplying 10 hp (7.5 kW) for up to one hour. The extra power capacity allows for expanded testing possibilities with regards to applied normal load and it also makes allowances for the possibility of increased power requirements for certain test configurations (i.e. higher than expected power requirements for high slip angles, low inflation pressures etc.).The motor performance graph supplied by the manufacturer is depicted in Figure 24.

A simple cost versus power analysis was also performed on possible drivetrain configurations. The selected motor was found to be the most cost effective in terms of overall testing envelope and power supply cost. A summary of this analysis is depicted in Figure 25. The 10 hp (7.5 kW) motor shows a clear peak in the power to cost ratio.

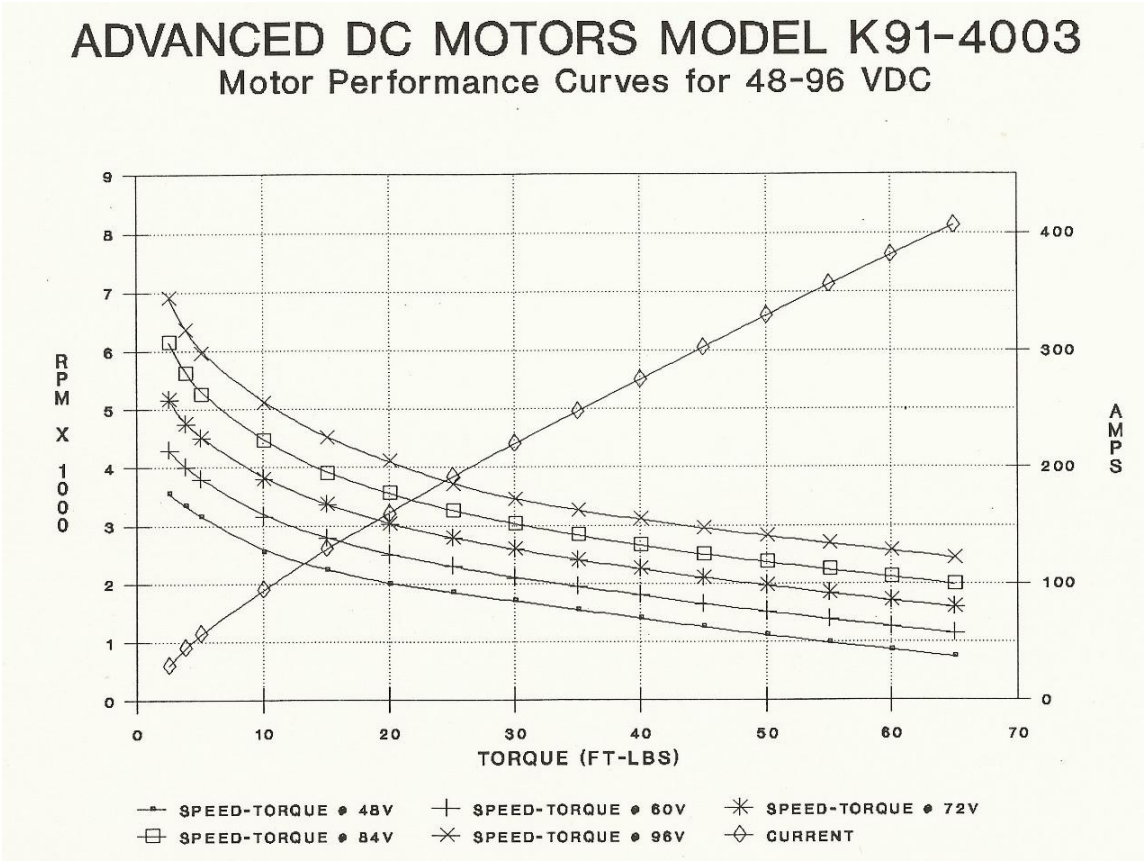

Figure 24. Motor performance graph of the AMD K91-4003

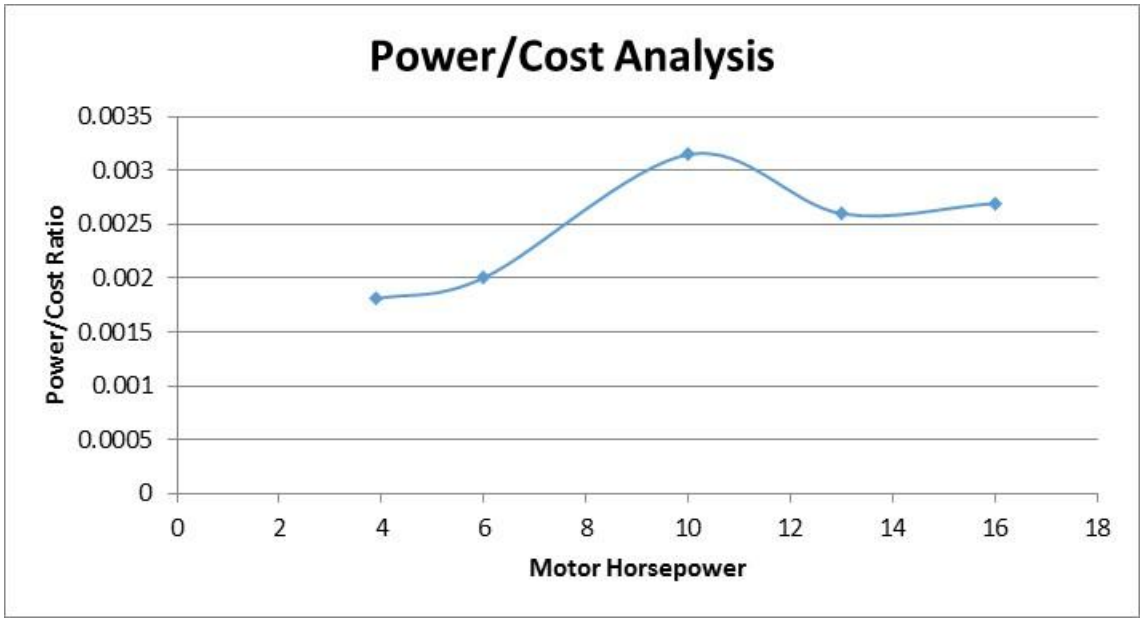

Figure 25. Power versus cost analysis for electric motors of increasing horsepower

After the motor was selected, a secure mounting method and power transmission system had to be developed. The mounting system had to be able to support the weight of the motor (approximately 50 lbf (222.4 N), resist deflection when the motor was activated, and prevent relative motion between the motor and the wheel. The tire hook arm was selected as the optimum location for the mounting system because it removed the need for synchronizing the vertical motion of the motor and wheel. Placing the mounting system on the hook arm also reduced the required length of the power transmission system. An L-shaped space frame design was created to mount the motor to the hook arm. An L-shape was chosen because it allows the motor to sit in front of the tire and makes the run for the power transmission system as short and straight as possible. A space frame concept was utilized to reduce the overall weight of the frame and to simplify construction. A CAD representation of the frame is depicted in Figure 26.

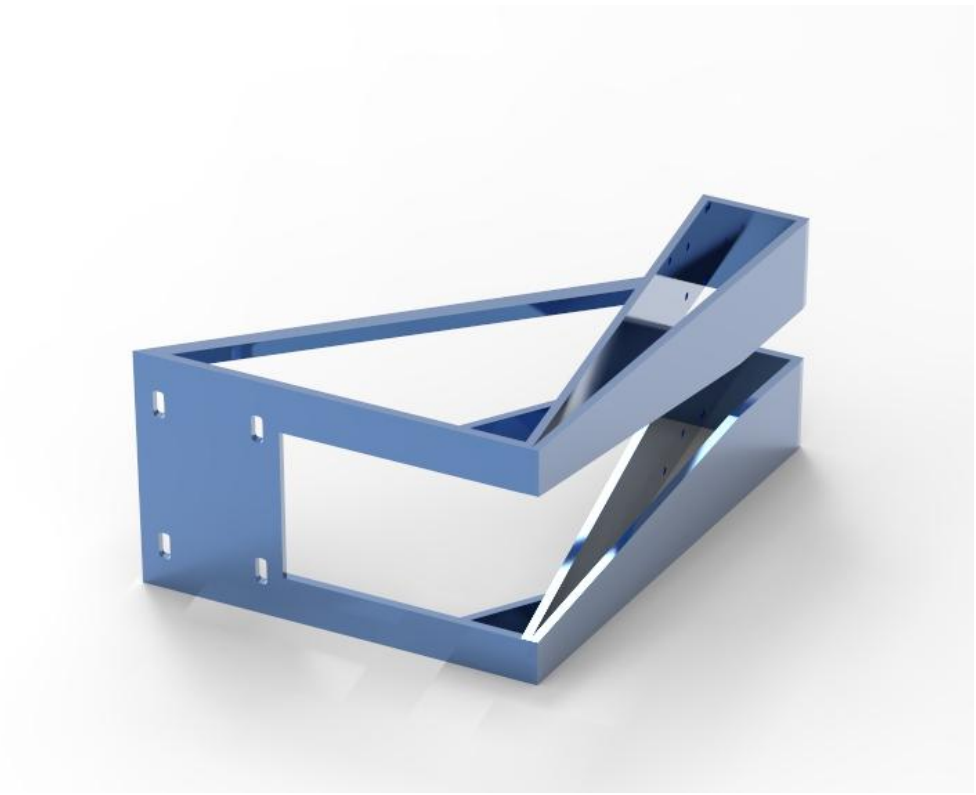

Figure 26. Rendering of the motor mount

The frame is made of 1 in (2.54 cm) square steel tubing. Steel tubing is easy to cut and weld and it possesses a yield stress of 33,000 psi (227619.8 kPa). The frame is attached to the hook arm by two 9/16th in (1.429 cm) grade 8 bolts. The completed frame is depicted mounted to the tire hook arm in Figure 27.

Figure 27. Completed motor mount frame connected to the test apparatus hook arm

The corners of the frame were reinforced with cross members to further stiffen it. The end of the frame farthest from the motor shaft was observed to deflect by 0.2 in (0.5 cm) when the drive chain was fully tensioned. An additional 0.05 in (0.127 cm) deflection was observed when the motor was activated while the wheel was suspended above the ground. No significant additional deflection was noted when the tire was on the ground and loaded.

The next component of the design to be addressed is the power transmission system. The close proximity of the motor to the wheel allows for the use of a direct drive system. Direct drive was chosen for its simplicity and its compactness. The power transmission system had to fit in the space between the tire and the hook arm. The location was chosen to take advantage of the

existing mounting holes on the wheel hub. Placing the drive system there also minimized the bending moment of the motor around the Z-axis of the hook arm. The lever arm for this moment was reduced to 3 in (7.6 cm). The total moment that can be exerted in this direction is 28.5 ft·lbf (38.6 Nm) based on the motor delivering 10 hp (7.5 kW) at 460 RPM. The drive system is also oriented to place the longest portion of the motor frame into compression, which further mitigates unwanted frame deflection. A chain drive was selected because chains have less stretch and slippage compared to the alternative of belt drives. Since the study focused on collection of accurate tire force data, it is important to ensure that force losses in the drivetrain are minimized. A gear ratio of 3:1 was selected for two main reasons. The first reason is to match the angular velocity of the test tire to the angular velocities normally encountered by the tire of a typical Baja car. It can be seen that the motor's output angular velocity ranges from 900 RPM at maximum torque to a maximum angular velocity of 3600 RPM in Figure 24. The normal range for the Baja car tire is 0 to 460 RPM assuming a top speed of 30 mph (48 km/h). To exactly match this RPM range, a gear ratio of 2:1 would be required for maximum torque output at the expected maximum RPM. The other factor that had to be considered is that the wheel sprocket had to fit around the diameter of the hook arm in order to utilize the optimum mounting position. The mounting requirement restricted the sprocket selection to ones with a bore diameter of 2.5 in (6 cm) or greater. Sprockets with such a large bore are not common, and the limited selection of tooth counts greatly reduced the number of possible drive ratios that could be selected. Sprockets of this size also require large chains of ANSI size 60 and up. A wheel sprocket with 60 teeth sized for ANSI 60 chain was selected as it was the most readily available sprocket that fit the dimension requirements. The drive sprocket provided a much greater selection to choose from with the far more common 7/8 in (2.223cm) bore. However, the drive sprocket must be matched with the

wheel sprocket so only sprockets for ANSI 60 chain could be considered. The available drive sprocket choices had between 10 and 20 teeth, which give a range of gear ratios from 6:1 down to 3:1. The 20 tooth sprocket was selected because it is the closest to the optimum ratio that was available. A gear ratio of 3:1 will produce output wheel RPM's in the desired testing range. The wheel sprocket is mounted on a custom fabricated axle that fits over the hook arm and connects to the wheel hub. The axle extension is made of 0.25 in (0.6 cm) mild steel plate and a 2.5 in (6.4 cm) mild steel pipe. The axle extension is connected to the wheel sprocket by three grade 8, 7/16 in (1.111cm) bolts and to the wheel hub by four bolts of the same specification. No deflection was observed of the axle extension when the sprocket was placed under load. A CAD representation of the axle extension is depicted in Figure 28.

Figure 28. Rendering of the axle extension

The control and power supply for the test apparatus were designed based on the requirements of the selected motor. The motor controller, contactors, and power cables have to be able to operate when the maximum current of 400 amps is applied. The system also has to be able to operate at 48 V. The controller has to operate in both forward and reverse and a reversing contactor is needed as well. The controller chosen to satisfy the requirements is the 1209B controller made by Curtis Instruments. The main function of the controller is to regulate the amount of current going to the motor which adjusts the speed and output torque. The current is routed to the proper terminals for forward and reverse motor operations via the reversing contactor. The output of the motor is controlled by the system operator through the use of a hand operated potentiometer. The potentiometer has a resistance range from 0 to 5 kΩ. The motor is off when the potentiometer is set to zero and it is at maximum current when it set at 5 kΩ. The potentiometer adjustment level can be easily manipulated with one hand and the desired setting can be maintained with a retaining pin. The control features allow the test apparatus to be operated while the operator is simultaneously driving the tow vehicle. Figure 29 depicts the potentiometer control. Figure 30 depicts the control systems wiring diagram.

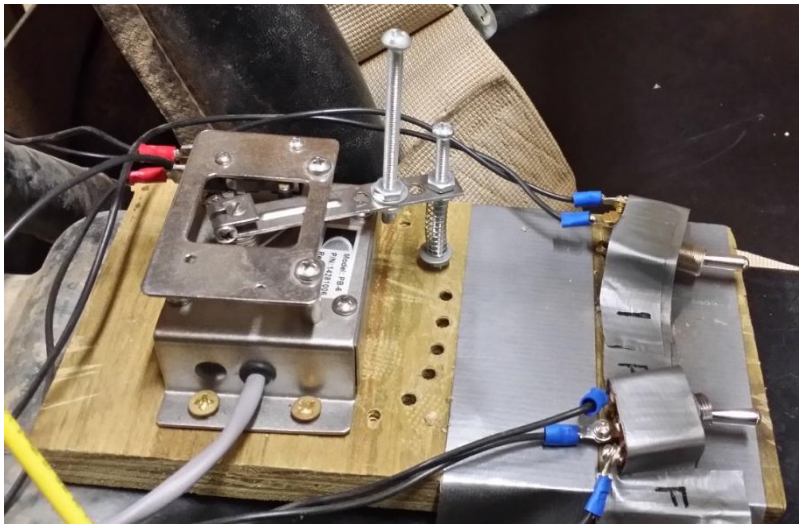

Figure 29. Potentiometer throttle and control switches

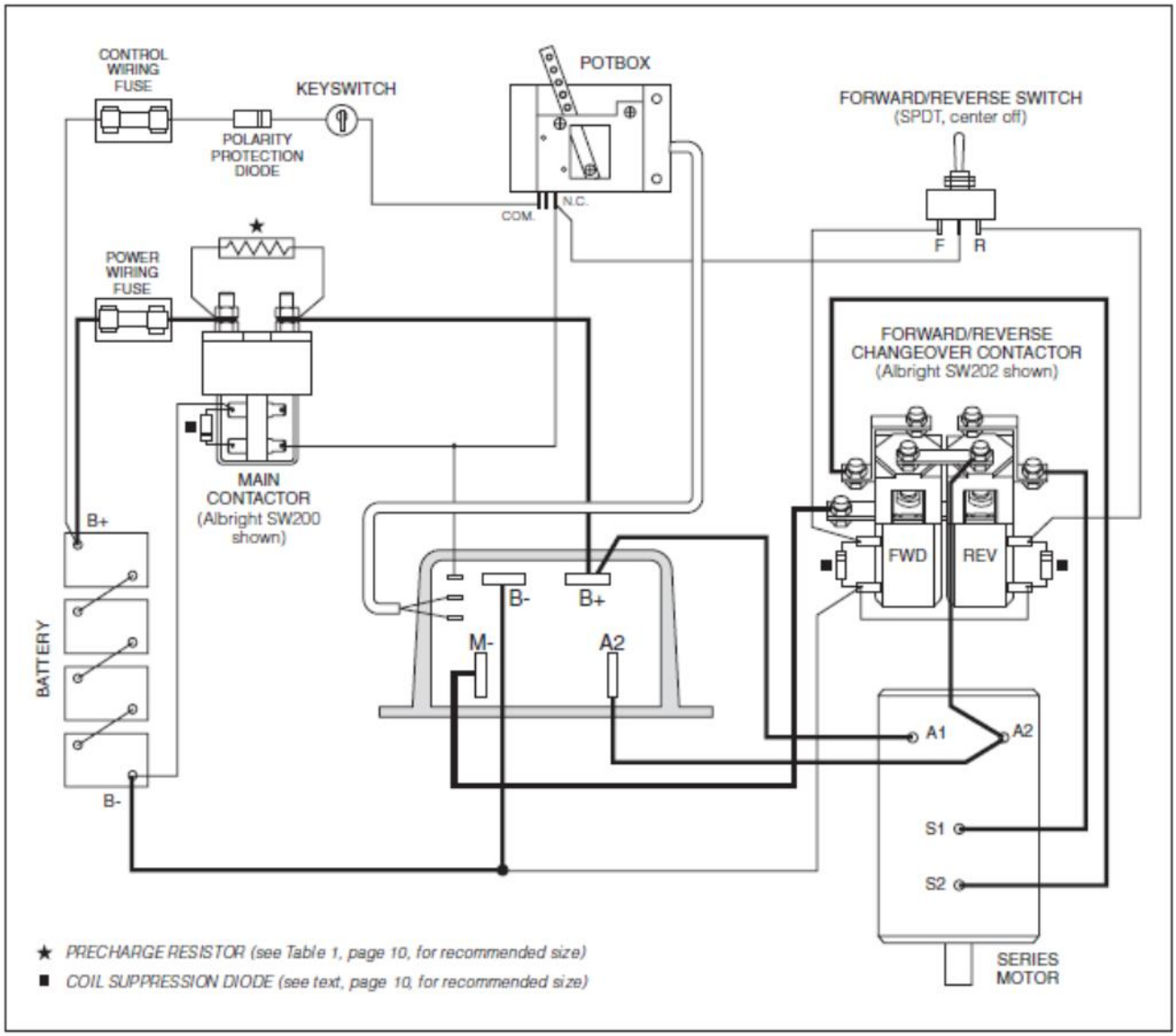

Figure 30. Control system and motor wiring diagram

The motor is powered by a battery bank composed of four 12V sealed lead acid batteries. The batteries are connected in series to supply the necessary 48V for the system. The lead acid batteries were chosen for the system because of their cost effectiveness and their ease of control. The lead acid batteries are quite bulky with the battery pack weighing over 120 lbf (533.8 N), but they cost only a third as much as an equivalent lithium-ion battery pack. The lead acid batteries

also do not need a separate battery management system to prevent over discharging and overheating. The system can be operated for 70 minutes before the batteries had to be charged.

An accurate determination of the tire's slip ratio is necessary for a usable description of the tire's forces. As previously discussed, the slip ratio is a major factor in the production of a longitudinal force in the tire's contact patch. The slip ratio can only be determined if the angular velocity of the wheel can be measured during a test run. The standard method for measuring the angular velocity in most vehicle systems is a Hall Effect sensor that either counts the teeth of the drive sprocket or a separate encoding wheel. The original placement of the sensor counted the teeth of the wheel sprocket as it rotated. This placement provided an angular velocity measurement of a part of the device that was hard mounted to the wheel, thus reducing the amount of data processing required. However, the nature of the terrain and the bouncing of the tire at higher velocities caused the sensor to crash into the sprocket as it rotated. Subsequent review of the data showed that while the data that was collected was usable, the continued impacts against the sensor would cause data loss. The Hall Effect sensor was relocated to a more solid mounting position on the motor frame. An encoding wheel was fabricated and attached to the motor shaft. The encoding wheel has 10 evenly spaced steel targets with dimensions based off of the manufacturer's guidelines for optimum sensing. The sensor records the output RPM's of the motor which could be converted into wheel RPM knowing the gear ratio. The slip between the drive sprocket and the wheel sprocket is negligible because of the nature of the direct chain drive and the short center to center distance of the sprockets (23 in, 58.4 cm). Figure 31 depicts the mounting of the Hall Effect sensor.

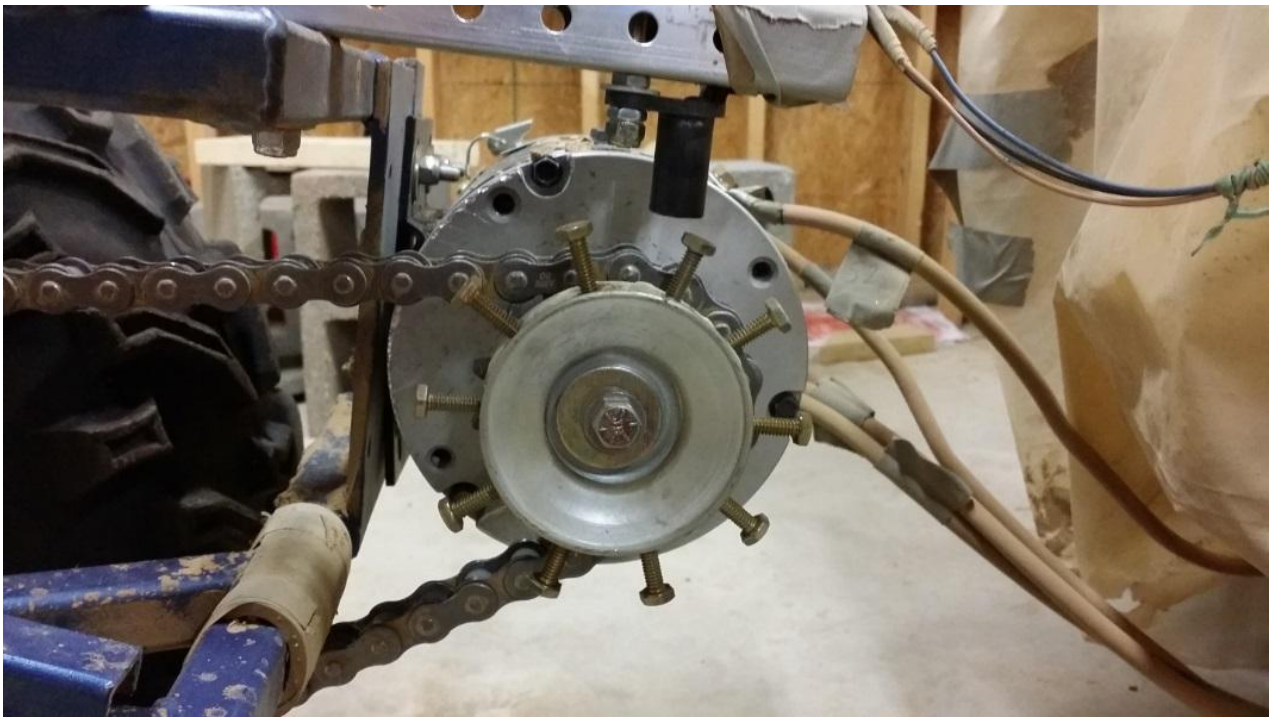

Figure 31. Hall Effect sensor mounting with encoder wheel

The speed-over-ground of the vehicle is also required to calculate the tire's slip ratio. The most effective means of recording vehicle velocity was by GPS. GPS provides greater accuracy and reliability than other methods such as integrating the signal of an accelerometer or using the tow vehicle's speedometer. The GPS signal is also easy to manipulate during data reduction and only had to be converted into the proper units for comparison to the recorded wheel velocity. The GPS device used for this study is an onboard unit in the DL-1 data recorder. The DL-1's GPS unit has a positional accuracy of 3 meters and a velocity accuracy of 0.1 mph (0.161 km/h). A CAD representation of the complete test apparatus is depicted in Figure 32. The complete tire test apparatus can be seen attached to the tow vehicle in Figure 33.

Figure 32. Rendering of the tire test apparatus

Figure 33. Complete tire test apparatus attached to the tow vehicle

2.1.2 Data Collection and Evaluation

Data collection is performed by two digital data recorders. The digital data collection system is a continuation of the system that was implemented by Krueger [2]. The all-digital system greatly simplifies the data processing and reduction stage allowing the data to be downloaded directly from the data recorders for analysis. The digital system is a major improvement over the University of Maryland [1] system that relied on an analog system that had to be transcribed by hand for computer processing. The force data from the three load cells (Transducer Techniques SB0-500) is recorded by a DATAQ-710 data recorder. The DATAQ-710 records the output voltage of the load cells and writes them to files stored on a removable SD card. The DATAQ-710 has an accuracy of ± 0.05% full scale range and a resolution of 12.2 μV. The range of the load cells used in this study is -30mV to +30mV, so the data recorder's measurements are accurate to ± 0.3mV. The sample rate for the load cells was set to 75 Hz. The 75 Hz sample rate was chosen because test runs that were recorded at higher sample rates showed many large transient force readings that lasted for 0.5 seconds and less. Setting a lower sample rate helped reduce the number of transients and more accurately display the steady state force readings. An example of the original load cell data is shown in Figure 34. The original data still appears quite noisy, but the data smooths considerably when it is converted into forces and then filtered through a Matlab program created for data reduction. Data processing will be discussed in detail in a following section.

The GPS signal and Hall Effect sensor measurements are recorded by a DL-1 data recorder. The DL-1 operates in a similar fashion to the DATAQ-710. The data recorder logs the voltage output of the Hall Effect sensor and writes it and the GPS data to a removable SD card.

Figure 34. Original voltage data from the load cells

The Hall Effect sensor is a Honeywell 1GT101DC model with a switching rise time of 15 µsec and a fall time of 1 µsec. The sample rate of the Hall Effect sensor is 100 Hz. An example of original data from the Hall Effect and GPS sensors is depicted in Figure 35. Figure 35 depicts the recorded frequency readings (blue) from the Hall Effect sensor plotted with tire speed-over-ground (red) recorded by the GPS unit. Hall Effect data and ground speed data will be combined during data reduction to calculate the slip ratio of the test tire.

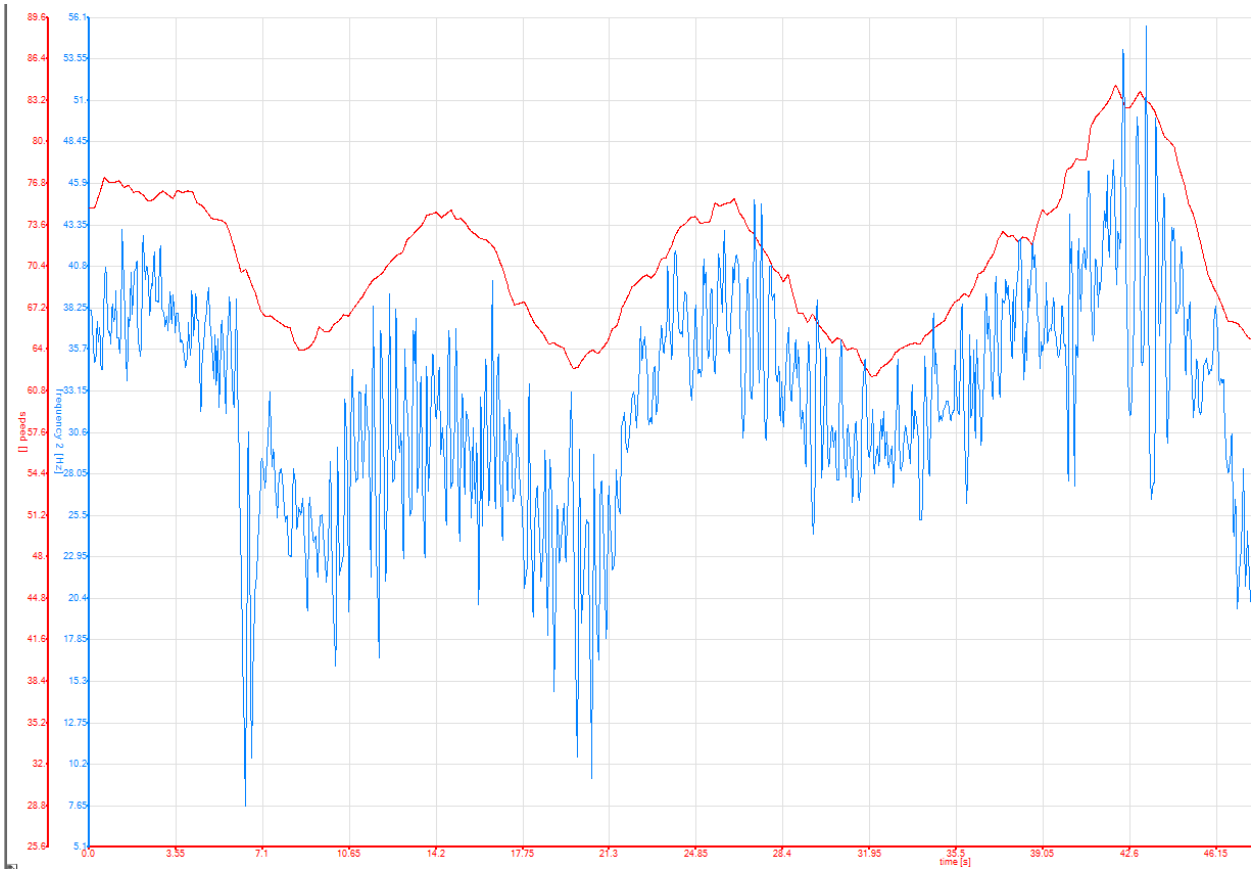

Figure 35. Original data from the Hall Effect sensor(blue line), speed-over-ground(red line)

2.1.3 Tire Test Apparatus Operations

The tire test apparatus was designed to be operated by one person who will be simultaneously driving the tow vehicle. The tow vehicle is a Yamaha Rhino which uses an automotive style control arrangement. The first step in operating the test apparatus is to set the desired slip and camber angles for a test run. The tire pressure is also checked at that point to ensure that it is the desired value. Once the apparatus is properly configured, a test run may begin. The test apparatus and tow vehicle were started approximately 20 ft (6.1 m) from the start of the test surface to allow the tow vehicle to accelerate to 10 mph (16 km/h) before the electric motor is activated.

The data loggers are set to start recording as the tow vehicle crosses the start line of the test surface. The electric motor is then activated and the potentiometer is set. The test apparatus then travels down the test surface for 120 ft (36.6 m). The motor and data loggers are then deactivated as the tow vehicle crosses the end of the test surface. The tow vehicle and test apparatus are then turned around and the process is repeated. A complete test run consists of the combined data for a down and back traverse of the test surface.

2.1.4 Calibration

The test apparatus had to be calibrated to ensure that the recorded data is an accurate representation of the forces generated by the tire apparatus. The device was calibrated by first placing it on level ground and initializing the data loggers. The data loggers were allowed to record for thirty seconds before they were turned off. The thirty second time period provides a good baseline reading from all of the sensors to establish what an input of zero looks like. Testing the device's output for a zero reading also helps to determine if any correction factors are necessary to adjust for any sensor offsets. No correction factors were needed as all of the sensors showed zero when the apparatus was level and stationary.

The next step in the calibration process is a test of the load cell output when a static, known load is applied to the frame. The load is applied by attaching a rope to the wheel hook and then running the rope over a smooth round bar positioned approximately 3 ft (0.9 m) off the ground. The smooth, round bar helps to reduce any friction effects from the rope. Weights are then attached to the rope and allowed to hang free. The rope is first positioned so it is directly behind the wheel which simulates only a longitudinal load pulling on the frame. The data logger

is then turned on and thirty seconds of data is recorded. The data is then analyzed to see if the longitudinal load cells are outputting the correct voltage for the added load. The lateral load cell readings are also checked to see if the sensor is outputting a zero reading correctly. After a successful check of the longitudinal load cells is completed, the rope is then oriented ninety degrees to the apparatus frame and a known load is applied to check the output of the lateral load cell. The longitudinal load cells are also checked to ensure they are reading a zero load correctly.

The final step in the calibration process is a check of the sensor readings when the apparatus is in motion. To do this, the apparatus is first set to its neutral position with the camber and slip angles at zero with no additional normal load placed on the tire apparatus. The apparatus is then towed at a constant velocity of 10 mph (16 km/h) and data is recorded over a traverse length of 120 ft (36.6 m). The motor is not activated during this traverse. The data is then analyzed to ensure that the longitudinal load cells are reading a drag force from the weight of the apparatus pulling on the ATV. The lateral load cell is also checked to ensure that it is reading zero correctly. Two more traverses with the apparatus in its neutral position are then conducted with the motor running in the forward and reverse directions respectively. The data from each of these traverses is checked to ensure that the longitudinal load cells are recording the correct pushing or drag force with the motor running. The lateral load cell is also checked again for a correct zero reading.

The Hall Effect sensor and GPS data outputs are also checked during these traverses to ensure they are functioning predictably. The test tire should have a slip ratio of near zero when being towed with its motor off. The data should also reflect a positive slip ratio when its motor is turned on in the forward direction and negative when it is reversed.

2.1.5 Test Tire

The tire being tested in this study is a K299 Bearclaw tire made by Kenda Tires. The K299 tire is a standard purpose ATV tire designed to be used on both soft and hard off-road surfaces. The tire has a chevron shaped tread pattern with a 0.6 in (1.52 cm) tread depth. The tire's dimensions are 22x8.00-10 in (55.9x20.3-25.4 cm). The tire's maximum recommended inflation pressure is 7 psi (48.3 kPa). The K299 tire is used on a wide variety of ATV's including SAE Baja competition cars. The K299 tire was selected to be the subject of this study because of its common availability and its applicability to the Auburn University motorsports program. Figure 36 shows a picture of the test K299 tire.

Figure 36. Kenda Bearclaw K299 tire

The vertical stiffness of the K299 tire at each tested inflation pressure was calculated by measuring the tire's vertical deflection when placed under load. The stiffness values are summa-

rized in Table 1. The listed normal load in Table 1 is in addition to the 111 lbf (493.7 N) that the motor and tire hook weigh. A graphical representation of the effect of pressure on the tire stiffness can be seen in Figure 37. Vertical stiffness increases linearly with the inflation pressure as is expected for a pneumatic tire. Stiffness also decreases with increasing normal load as the tire carcass undergoes more deformation due to vertical load. Figure 37 also shows there is a supported normal load where the tire stiffness decreases substantially and there is a corresponding increase in tire deflection. The Kenda Bearclaw K299 tire reaches a rapid stiffness change point at approximately 200 lbf (889.6 N). The load at which the rapid stiffness change occurs would be useful information to a designer as carcass deflection plays a significant role in the lateral and longitudinal force production. The change in the carcass stiffness after the normal load passes the critical point also becomes much smaller. A change from 225 lbf (1000.8 N) additional normal load to 270 lbf (1201.0 N) at 7 psi (48.3 kPa) inflation pressure only changed the stiffness by 43.08 lbf/in. In contrast, a change in normal load from 45 lbf (200.2 N) to 90 lbf (400.3 N) additional load changed the carcass stiffness by over 800 lbf/in (1401.01 N/cm) at the same inflation pressure. The Kenda Bearclaw K299 tire is therefore more sensitive to normal load changes when the overall normal load is less than 200 lbf (889.6 N). Load sensitivity is especially important to lighter vehicles that are operating with normal loads in the tire's critical range. A relatively small change in the vehicle's normal load could have a significant effect on the tire's lateral and longitudinal force production.

Table 1. Vertical Tire Stiffness

Additional Normal Load		Tire Pressure		Deflection		Vertical Tire Stiffness	
lbf	N	psi	kPa	in	cm	lbf/in	N/cm
45	200.2	2	13.8	0.1875	0.47625	832.00	1457.050
90	400.3			0.375	0.95250	536.00	938.680
135	600.5			0.5	1.27000	492.00	861.624
180	800.6			0.625	1.58750	465.60	815.391
225	1000.8			0.875	2.22250	384.00	672.487
270	1201.0			1.125	2.85750	338.67	593.102
45	200.2	5	34.5	0.0625	0.15875	2496.00	4371.166
90	400.3			0.34375	0.87313	584.73	1024.019
135	600.5			0.46875	1.19063	524.80	919.066
180	800.6			0.59375	1.50813	490.11	858.314
225	1000.8			0.75	1.90500	448.00	784.568
270	1201.0			1	2.54000	381.00	667.233
45	200.2	7	48.3	0.09375	0.23813	1664.00	2914.111
90	400.3			0.25	0.63500	804.00	1408.020
135	600.5			0.28125	0.71438	874.67	1531.782
180	800.6			0.46875	1.19063	620.80	1087.187
225	1000.8			0.65625	1.66688	512.00	896.649
270	1201.0			0.8125	2.06375	468.92	821.205

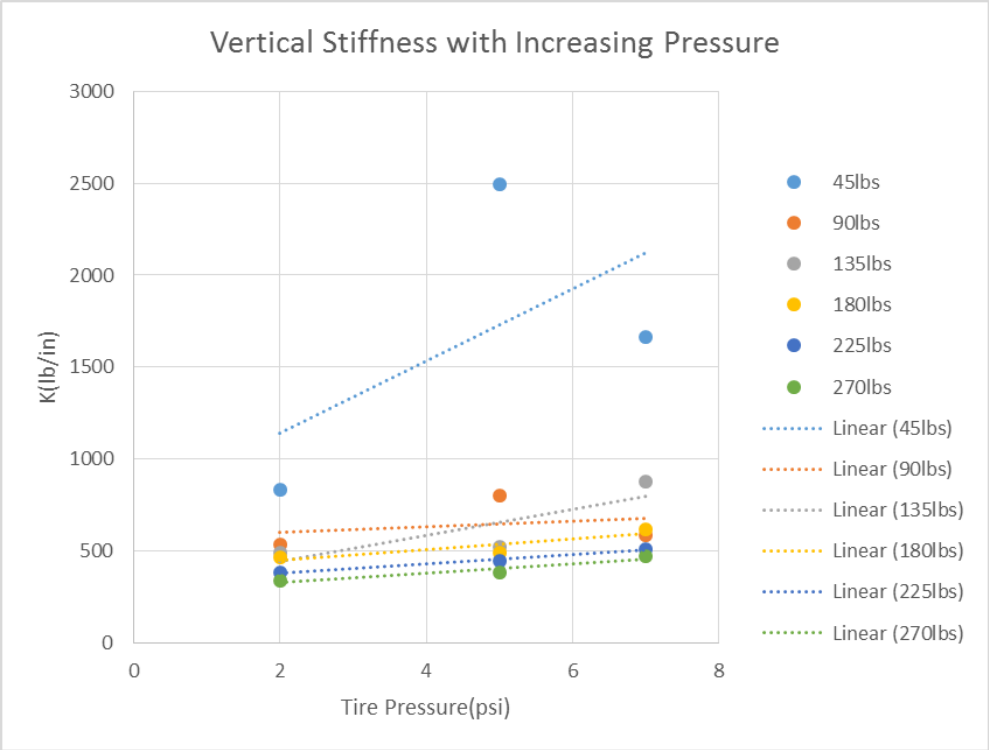

Figure 37. Vertical K299 tire stiffness versus tire inflation pressure

2.2 Surface Characterization

2.2.1 Method

Surface characterization is a critical component to any tire/soil interaction study. A detailed surface characterization allows the results to be put into context with other tire/soil interface research. The surface characterization lets the collected data be compared to results from similar and different surfaces. There are several methods that can be used to characterize the surface properties. However, most of these methods were created to allow for faster analysis of the trafficabilty of a surface for industrial and military vehicles [15]. These methods were not intended for detailed terrain studies. The method used to describe the soil surface properties in this study was the gross traction method used by the U.S. Army Corps of Engineers in cold climate mobility studies [18].

The strength properties of a given soil can vary greatly depending on a number of factors as soil moisture content, soil composition, and how a load is applied to the surface. In order to find surface properties that are of most use in a study, a careful examination of the specific kind of loading that will be observed must be undertaken. The tires of a wheeled ground vehicle will apply a surface load that will be a combination of both compression and shearing [17]. In addition, the compression and shearing occur in unequal portions throughout the motion of the tire making it extremely difficult to pinpoint exact quantities at any given moment [13]. Therefore, the best way to measure a surface's properties for a wheeled vehicle study is to use an instrumented tire. The instrumented tire can exactly reproduce the loading that will be experienced by the wheels of a ground vehicle. The addition of a motor to drive the instrumented tire allows for both traction and resistance tests to be performed on a wheel.

The surface properties are calculated using what is referred to as the "Gross Traction Method" by the U.S. Army Corps of Engineers. The method is based upon the principle the shearing of the surface is caused by the gross traction of the tire across its contact area. The gross traction is made up of what is termed the net traction, T_N, of the wheel and also the rolling resistance, $MR_{terrain}$. Equation 9 was developed by Shoop [18] to summarize the relation.

$$T_G = T_N + MR_{terrain} \tag{9}$$

In order to find net traction and rolling resistance, it is necessary to conduct two separate tests. The first test is a traction test that is conducted with the motor of the instrumented tire engaged. The instrumented tire is brought up to a constant velocity of 10 mph (16 km/h) by the towing ATV and then the motor of the instrumented tire is activated and set to drive the wheel at between 5-10 % slip. The force created by the tire at the surface interface is recorded by the longitudinal load cells. The slip ratio is recorded using the GPS sensor on the data recorder and the

Hall Effect sensor attached to the motor frame. The force recorded by the longitudinal load cells during the traction test is the net traction.

The second test conducted is a rolling resistance test. The motor of the instrumented tire is not engaged for this test. The test begins with the instrumented tire being brought up to a constant velocity of 10 mph (16 km/h) by the towing ATV. The drag exerted by the free rolling test wheel is then recorded by the longitudinal load cells. The recorded drag force becomes the rolling resistance. The quantities recorded from each test are added together and become the gross traction. It is important to ensure that each test is conducted on the same terrain course to ensure the data collected can be correctly related. Traction and resistance tests conducted over different surfaces cannot be used with Equation 9. Also, care must be taken when selecting motor speed because the two tests cannot be compared if the slip ratio exceeds 0.25 [18]. A force diagram of the instrumented wheel can be seen in Figure 38.

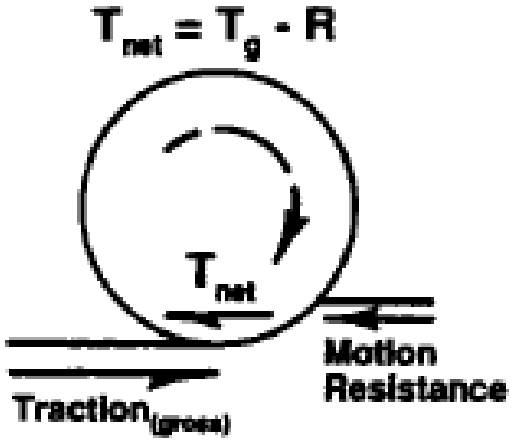

Figure 38. Tire forces used with the gross traction method [18]

The traction and rolling resistance tests were conducted with normal loads ranging from only the normal load of the instrumented tire apparatus by itself to a maximum additional load of 270 lbf (1201.0 N). The normal load was increased in 45 lbf (200.2 N) increments. The camber and slip angles were set at zero for all of the tests.

2.2.2 Surface Property Calculation

Once the gross traction was known, it was then possible to calculate the shear stress that was being applied at the soil tire interface. The only additional quantity needed is the contact area of the tire caused by the applied normal load. The contact area is measured by placing the instrumented tire apparatus on a hard surface with the normal load to be tested. A print of the tire is then made and measured to find the contact area. However, the contact area will change from the static measured size as it is rolling. The dynamic changes to contact area were determined to be small and not significant when the tests were run at low speed (<20 mph, <32 km/h) and on surfaces where the tire did not sink more that the height of the tire tread lugs [8]. After determining the contact area, Equations 10 and 11 can then be used to determine the shear stress and normal stress respectively.

$$\tau = \frac{T_G}{A} \tag{10}$$

$$\sigma_n = \frac{N}{A} \tag{11}$$

The shear and normal stress values are then used to compute the Mohr-Coulomb Failure Criteria using Equation 12.

$$\tau = \sigma_n \tan(\varphi) + c \tag{12}$$

The soil cohesion, c, and friction angle, φ, are determined by plotting the shear stress against the normal stress. From the work of Terzhagi [14], the soil's cohesion value is determined from the y intercept of the data and the friction angle is determined from the angle that is made by the linear best fit line. An example of how these properties are determined is depicted in Figure 39.

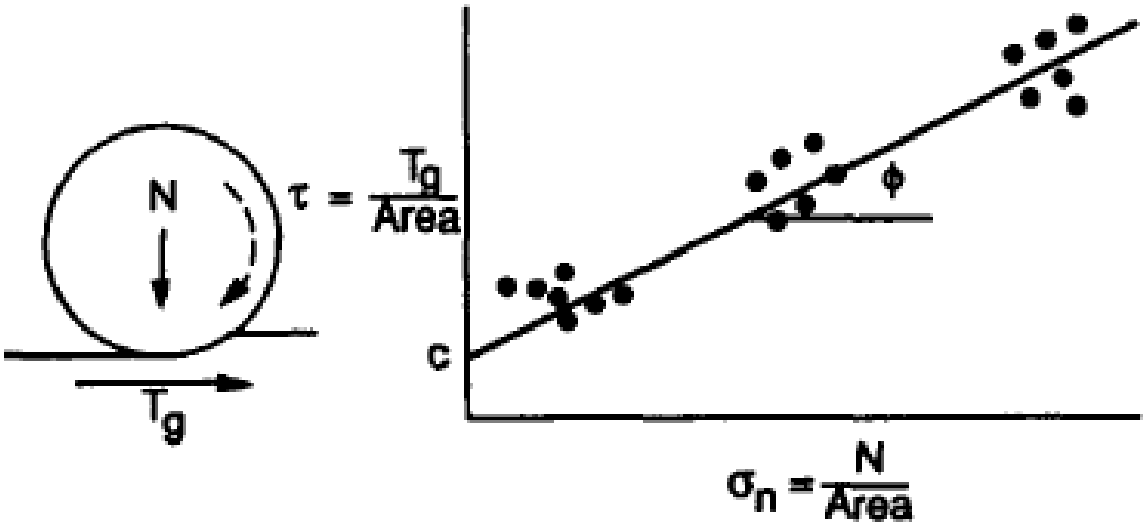

Figure 39. Example plot depicting the determination of c and φ [18]

2.2.3 Evaluation

The characterization of the soil surface must be consistent with similar data that has been collected in order to be of use. The chosen method must be compared with other accepted soil surface characterization tests to show that it can produce useable and logical results. The method comparison will be restricted to tests that report the soil's cohesion and friction angle. Soil cohesion and friction angle are considered the most significant soil properties since they have a physical meaning. Soil surface characterizations like the cone penetration index only report results in terms of a quantity that does not have a direct physical meaning. Methods that do not have a direct physical meaning will not be discussed.

The fact the soil properties of cohesion and the friction angle have a physical meaning can be easily observed allowing for quickly checking computed values. If the soil surface being tested is composed solely of loose sand, the characterization method being used must measure a cohesion of zero or very near zero. Likewise, if the soil surface is composed of compacted marine clay, a high cohesion value must be measured. If the values for the soil surface properties determined by a particular method do not fit the observable characteristics of the tested soil, then the method needs to be reevaluated or replaced.

The first method for comparison is the triaxial shear test discussed in Chapter 1. The triaxial shear test is widely considered the industry standard for the determination of soil shear strength in civil engineering practice [15]. In Shoop's comparison study [18], the results for soil cohesion and friction angle were most similar between the instrumented wheel and the triaxial shear test. The triaxial shear test being a laboratory method allows for much greater control of the test conditions that the soil is subjected to than any in situ test. The agreement between the instrumented wheel and the triaxial shear test speaks well for the accuracy of the gross traction method.

The instrumented wheel was also compared to the shear annulus test which forms one half of the widely used bevameter surface characterization method. The shear annulus is usually a portable device and is not capable of creating the normal loads and shear loading that can be measured with both the instrumented wheel and the triaxial shear test. Because of the lower normal loads, the shear annulus test tends to overestimate the amount of traction that a soil surface can support [18]. The test also reported soil cohesion and friction angle values that were lower than those from the instrumented wheel and the triaxial shear test. However, the shear annulus test can be useful for constructing the complete form of the Mohr-Coulomb failure envelope. The

lower normal loads allow the shear annulus to measure the portion of the failure envelope that is in the typically non-linear region of the graph. An example of this non-linear region can be seen in Figure 40.

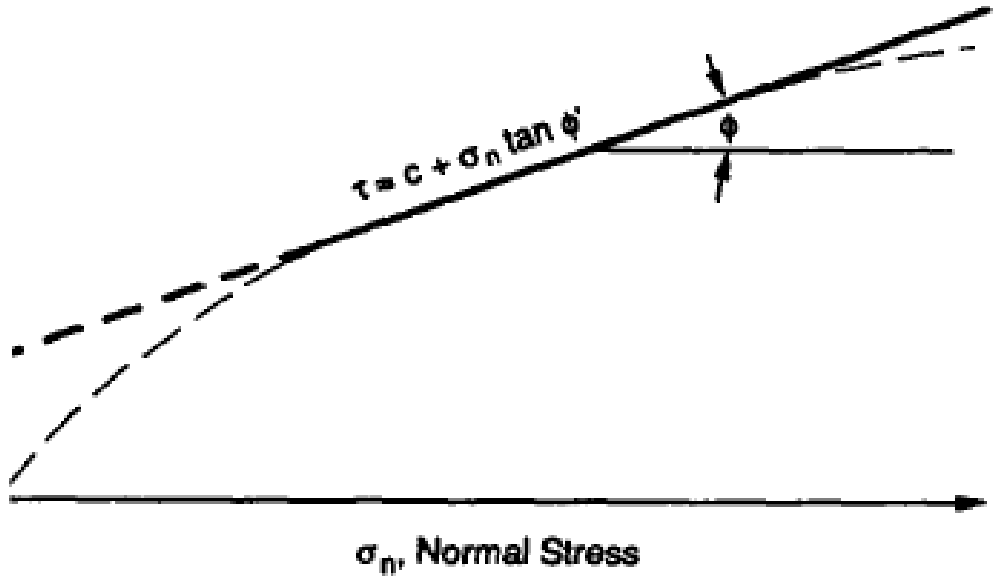

Figure 40. Example of the non-linearity found under low normal loads in the Mohr-Coulomb Failure envelope [18]

Typically, the failure region that is of interest is the linear area caused by higher normal loads. The curved portion of the graph of interest is generally approximated with a straight line. The non-linear area would only really be of interest in a study with a vehicle with low ground contact pressure.

A traction comparison study using the gross traction method for surface characterization was conducted by Blaisdell [18] in 1987 comparing the traction results predicted for an instrumented wheel and the actual results measured from a mobile ballistic missile launcher. The instrumented wheel was used to calculate the soil cohesion and friction angle of the test surface and those values were then used to predict the traction that would be expected from a vehicle of the mobile launcher's size. The predicted and measured results were within 10 % of each other

which demonstrates the gross traction method's ability to accurately quantify the surface characteristics.

2.3 Data Reduction

2.3.1 Load Cell Data

The main tool used for processing the load cell data is Matlab. An M-file was created to automate the processes of importing and analyzing the data. The recorded voltage output of the load cells is stored on an SD card. It is necessary to convert the data into useable quantities in terms of force before any analysis can begin. The transformation into force measurements is accomplished by dividing all of the voltage readings by the load cell scaling factor to obtain results expressed in pounds-force. The scaling factor was determined from Equation 13. The scaling factor for the load cells is $6x10^{-5}$ mV/lbf.

$$\frac{\left(\frac{3mV}{V}\right)(10V)}{500lbs} \tag{13}$$

After the data is converted to pounds-force, the forces are transformed from the frame coordinates into tire coordinates. The coordinate transform is accomplished using Equations 14 and 15 to produce Fx and an Fy in terms of the tire coordinates. Refer to Figure 19 for the free body diagram of the tire and apparatus frame.

$$F_x' = -F_{x1}cos\alpha - F_{x2}cos\alpha - F_y sin\alpha \tag{14}$$

$$F_y' = F_{x1}sin\alpha + F_{x2}sin\alpha - F_y cos\alpha \tag{15}$$

The data at this point is still difficult to use as the original output of the load cells can have a lot of noise as can be seen in Figure 41.

In order to reduce the noise and make it easier to find a steady state force value, it is necessary to filter the data to eliminate the high and very low magnitude transients. The filtering method chosen is a one dimensional digital filter which is also known as a moving average. The filter is a direct Form II transposed application of the standard difference equation.

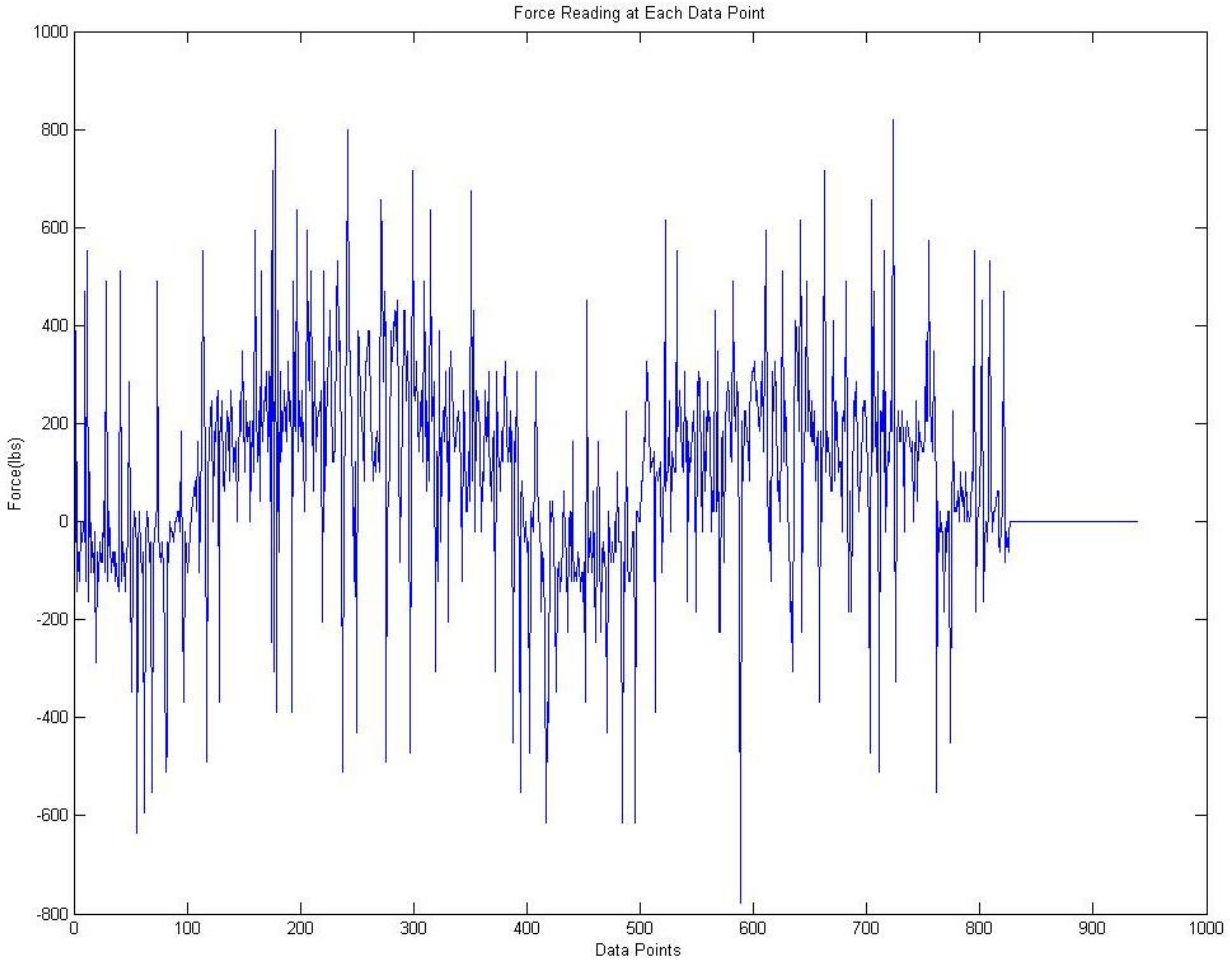

Figure 41. Unfiltered force readings

The filtering is performed using the built-in Matlab function “filter”. The filter receives the array containing the transformed force values for a particular test run and also a window size parameter that determines the number of elements from the input array that are used in each filter calculation. The greater the window size the smoother the output of the filter. An example of the filtering process can be seen in Figures 42-44. Note how the large transient values are the first to be filtered out at small window sizes and a clear average force value begins to appear as the window size is increased.

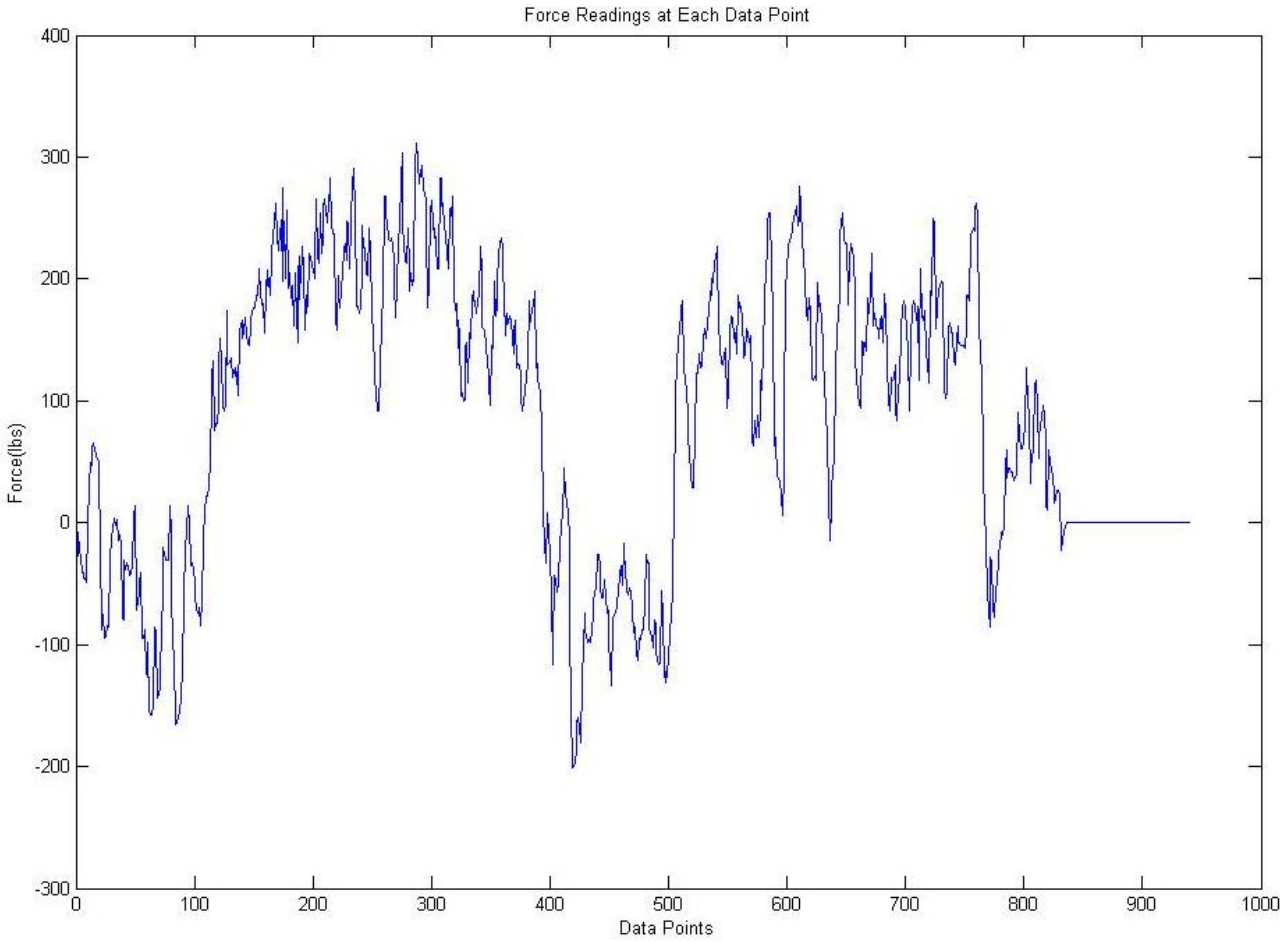

Figure 42. Filtered force data with a window size of 10

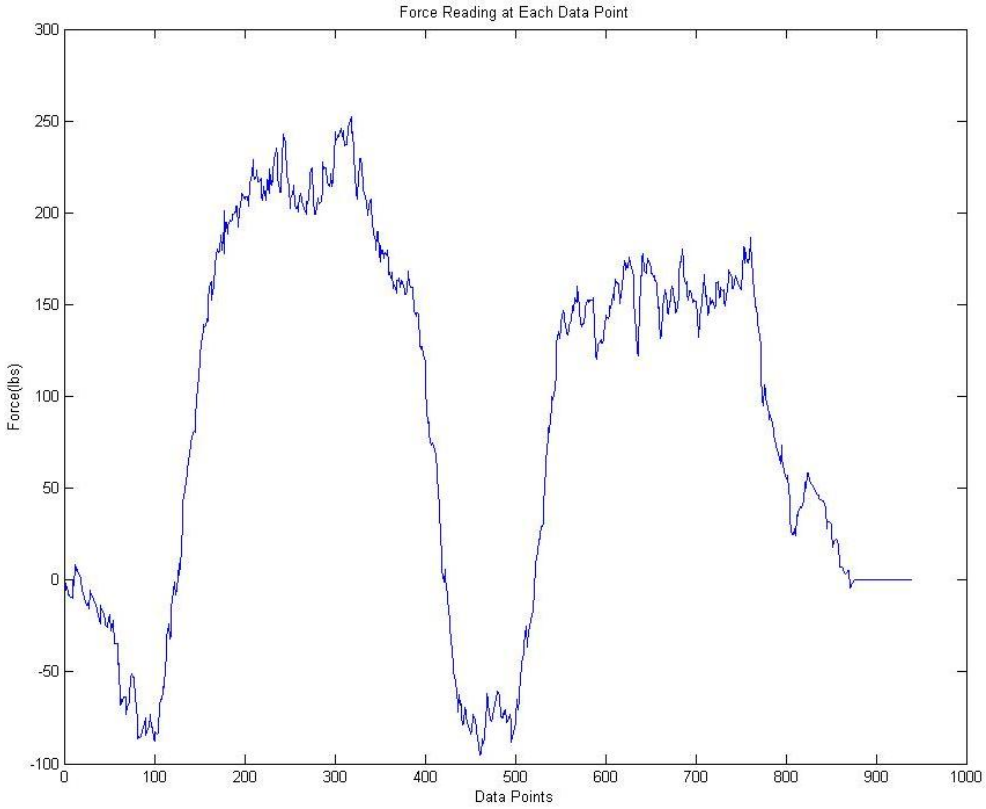

Figure 43. Filtered force data with a window size of 50

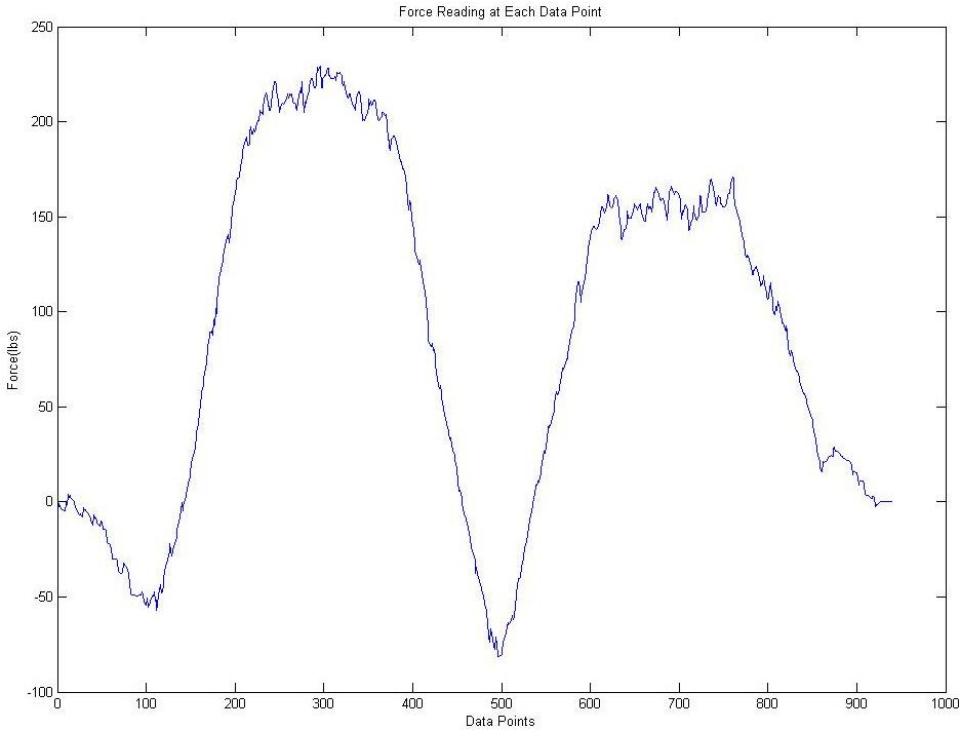

Figure 44. Filtered force data with a window size of 100

It is important not to set the window size too wide as this will cause too much rounding of the greater magnitude values and significant data points will be lost or obscured. A window size of 150 provides a good compromise between noise reduction and data resolution.

The completed graphs are then examined and an average and a maximum force value are selected. Visual inspection was used to pick average and maximum values because a purely arithmetic mean would be biased from the acceleration and deceleration portions of the graphs. An example of the processed load cell data is shown in Figure 45.

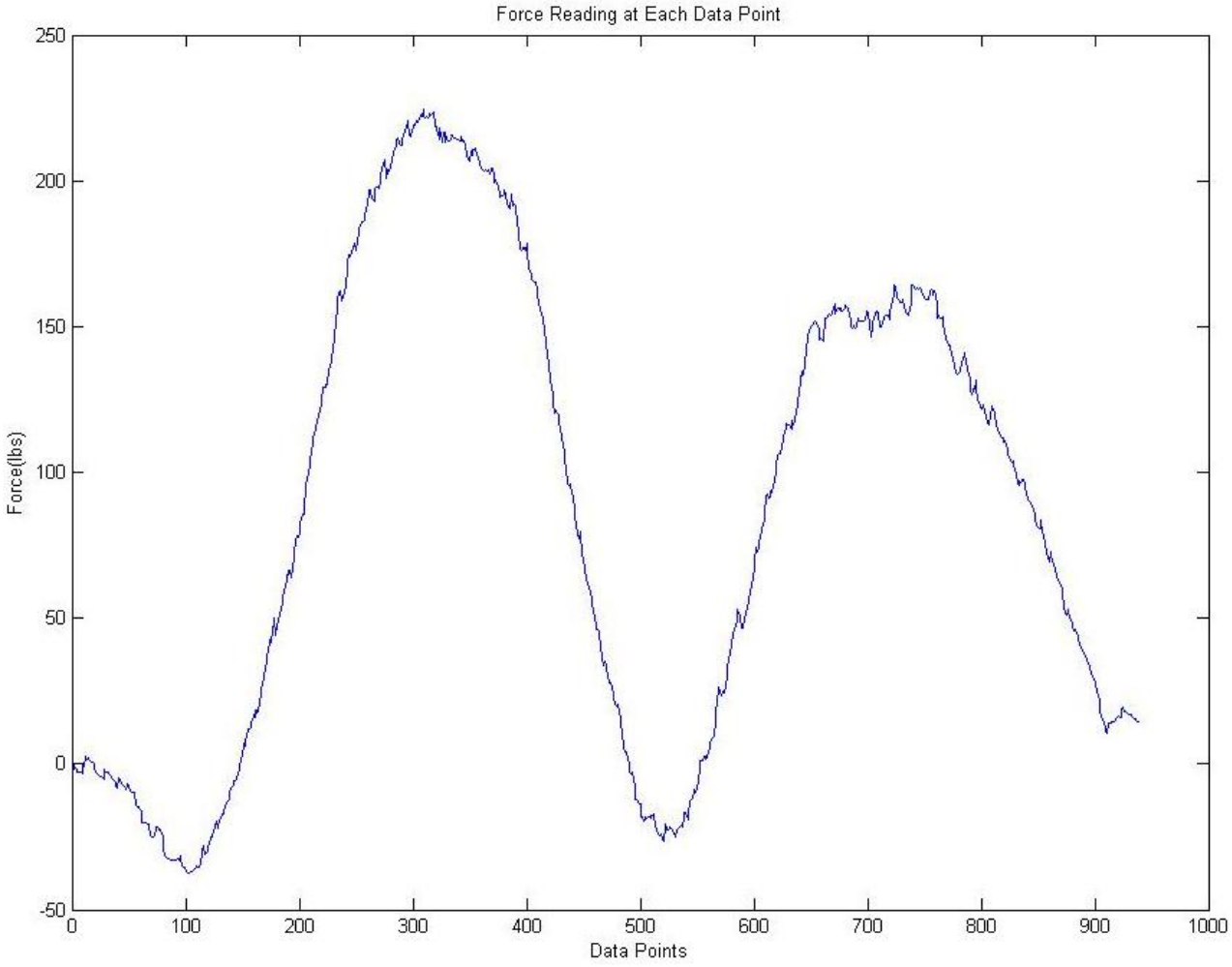

Figure 45. Fully filtered force data

As the maximum and average force values are being selected for each device setting, the information is entered into a spreadsheet (Microsoft Excel). The spreadsheet is used to create graphs for comparing the data between test runs. The values obtained from the load cell output become a single data point for each of the new plots. The values can then be organized to create graphs of longitudinal force versus slip ratio, lateral force versus slip angle, and other relationships of interest. Examples of fully processed data are depicted in Figure 46.

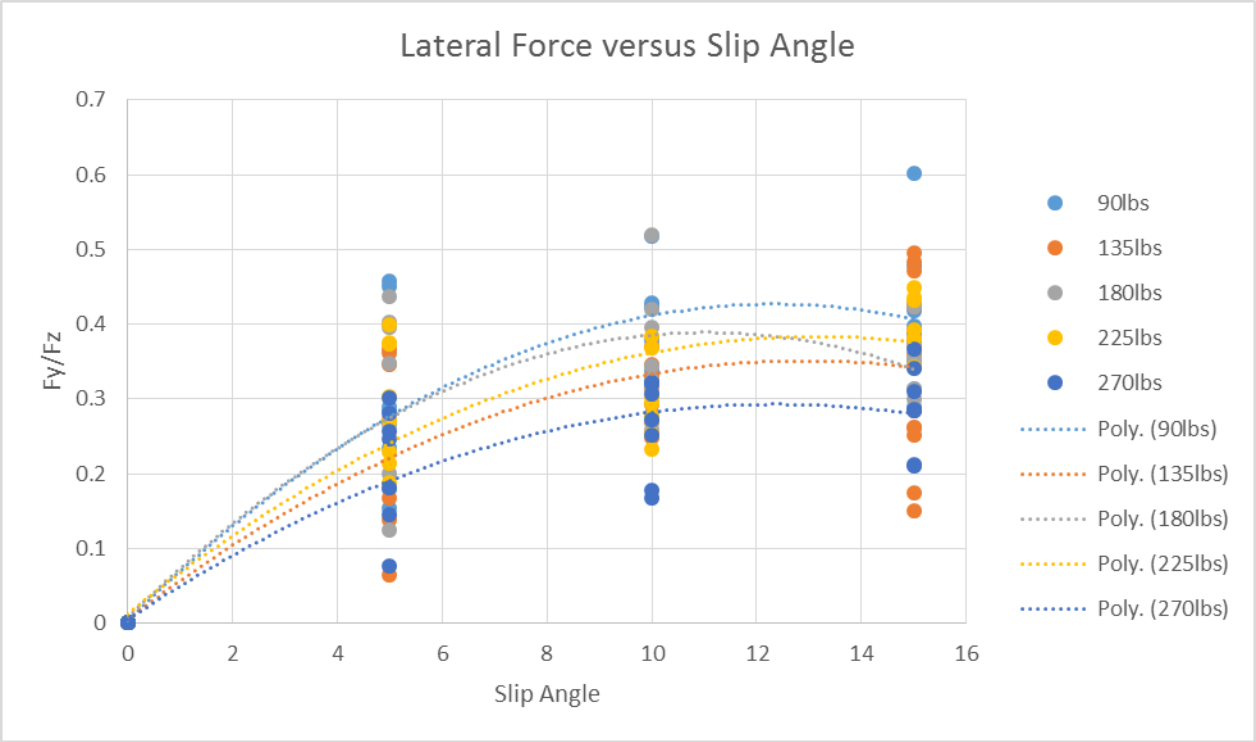

Figure 46. Lateral force versus slip angle for test runs conducted at 5 psi (34.5 kPa) inflation pressure and 0 degrees camber

2.3.2 Hall Effect Sensor Data

The data recorded by the Hall Effect sensor was reduced using the Race Technology analysis software that is included with the DL-1 data recorder. The analysis software allows for

easy importation of the data from an SD card and has many built in data post processing functions. The Hall Effect sensor data had to be first converted into units of angular velocity. The original data is composed of the sensor's pulse count as the encoding wheel turns with the motor. Equation 16 was used to convert the pulse count into revolutions per minute.

$$\frac{\omega}{N} \cdot \frac{1}{a} \cdot 60 \frac{sec}{min} \tag{16}$$

ω is the pulse count of the Hall Effect sensor, n is the number of teeth on the encoding wheel, and *a* is the gear ratio for the direct drive system. The transformed data still possesses a large degree of roughness and further processing is needed. The Race Technology analysis software has built in data filtering functions similar to the "filter" command found in Matlab. The data was filtered with a finite difference algorithm similar to the one used for load cell data. The data was smoothed over an interval of 1 second. An example of the filtered and transformed Hall Effect sensor data can be seen in Figure 47.

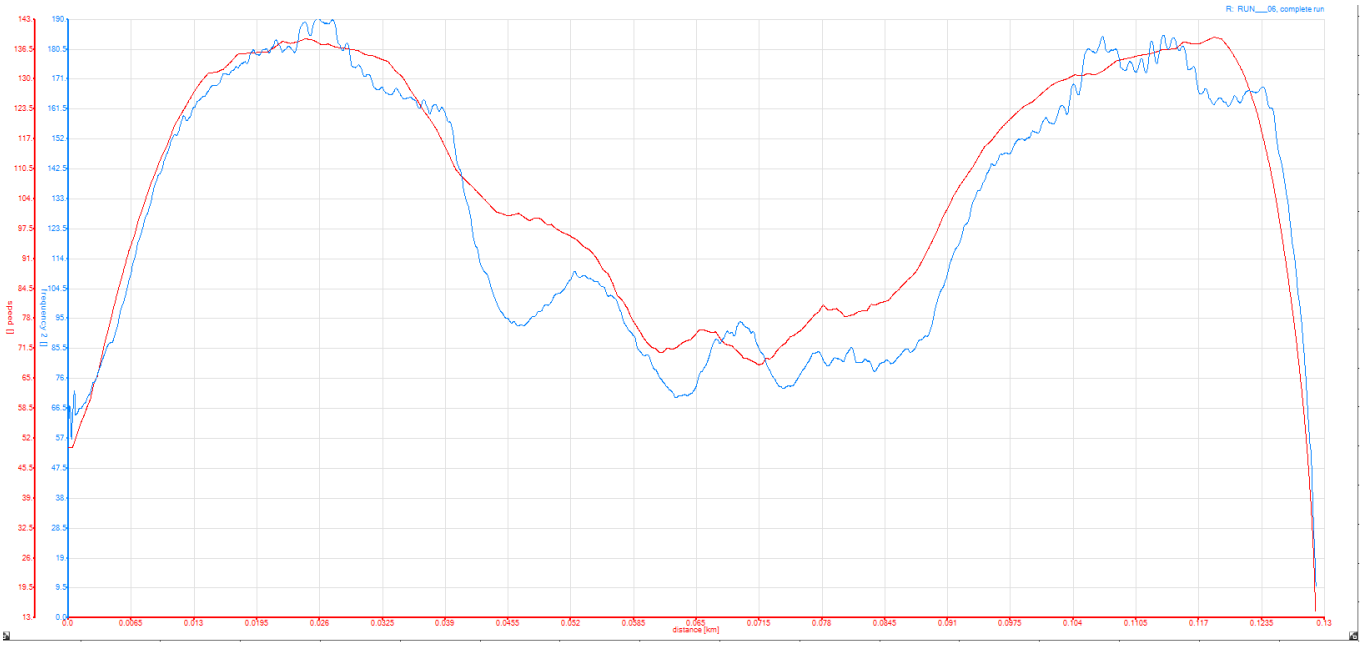

Figure 47. Smoothed and filtered data(blue line) recorded by the Hall Effect sensor plotted with vehicle speed-over-ground(red line)

Once the filtering process for the data was complete, the analysis software was used to compute the tire's slip ratio based upon over ground speed of the vehicle and filtered angular velocity of the tire. The tire angular velocity was converted into a linear velocity using the diameter of the K299 tire. The vehicle and tire velocities were then compared using Equation 1. The equations necessary to calculate the slip ratio were then entered directly into the Race Technology analysis software and no other programs were needed to process the Hall Effect sensor data. An example of the calculated slip ratio plotted with the vehicle's speed-over-ground is depicted in Figure 48.

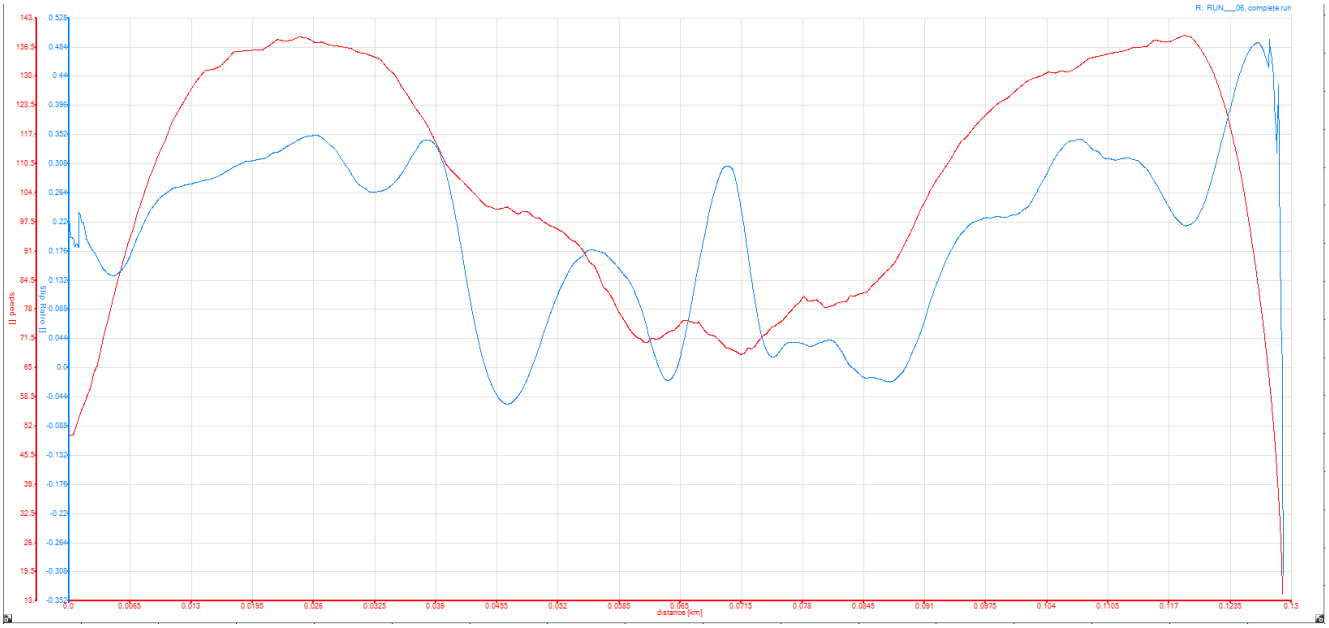

Figure 48. Tire slip ratio plotted with the vehicle speed-over-ground

The fully processed data was plotted in the manner seen in Figure 48 for each test run. The average slip ratio for each run was taken from its respective graph and the values were entered into the Excel spreadsheet along with the average and peak force data. The slip ratio values can then be used to plot the final results.

Chapter 3. Results

3.1 Data Validation

The data collected in this study was validated against both previously collected empirical data as well as theoretical models. Figure 49 depicts the results reported by Krueger [2] using a similar technique to the one used in this study.

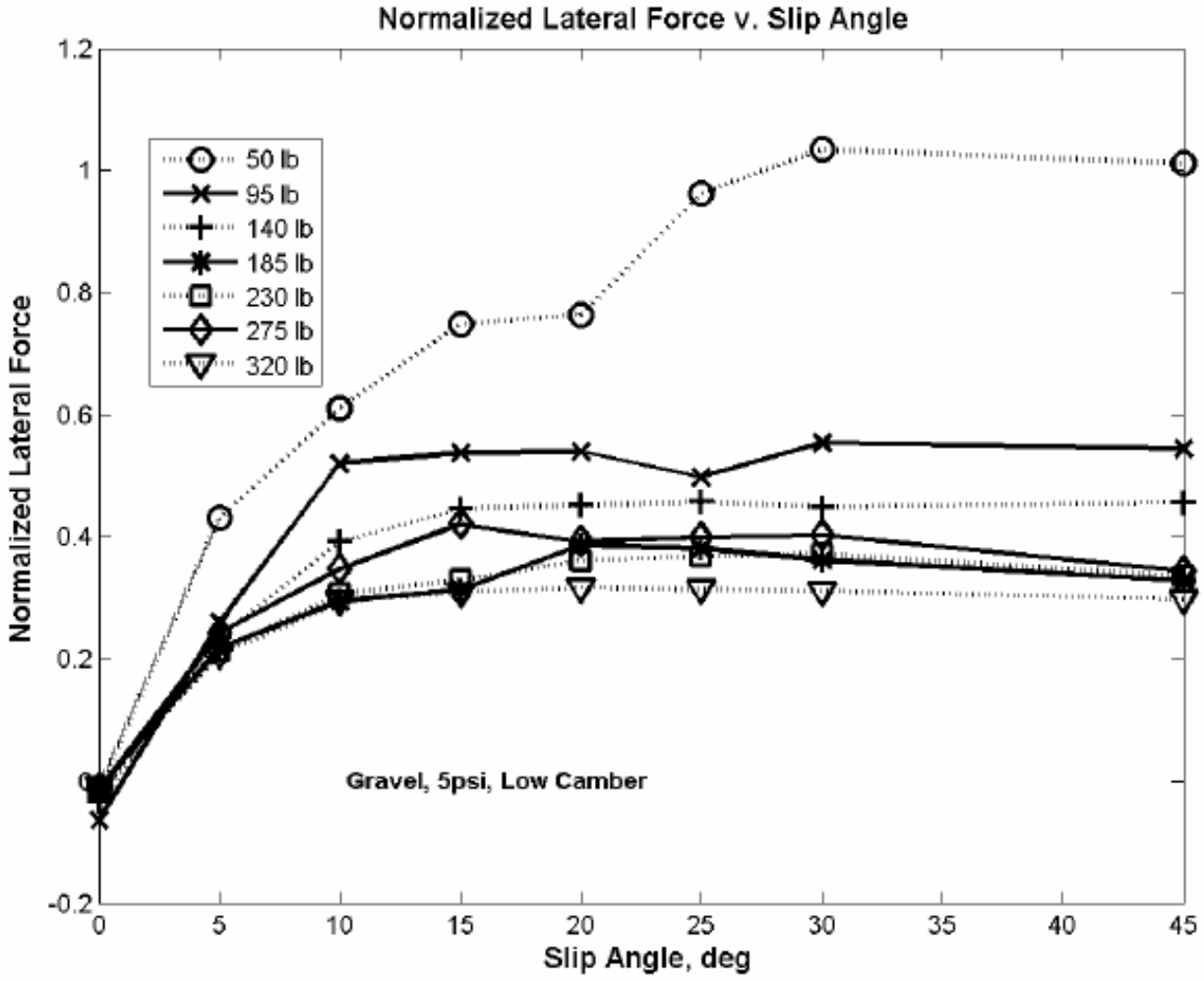

Figure 49. Normalized lateral force versus slip angle recorded by Krueger [2] for a free spinning wheel

Figure 49 depicts lateral force versus the slip angle for a free spinning wheel. Figure 50 depicts an example of data collected in this study presented in the same manner as data by Krueger in Figure 49.

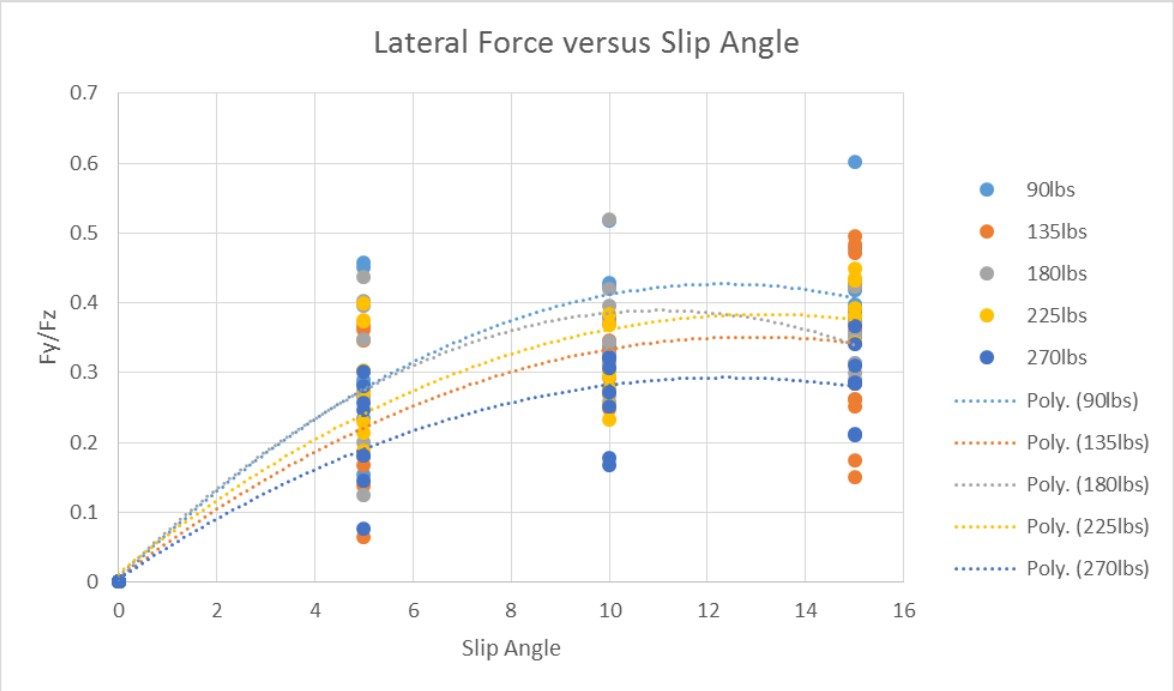

Figure 50. Normalized lateral force versus slip angle for an unpowered tire at 5 psi (34.5 kPa) inflation pressure and 0 camber

Both graphs show a linear increase and then a break point where the force increase begins to slow and then flattens out as the slip angle is increased. The results determined by the author and Krueger could not be directly compared because Krueger used a tire of a different configuration and manufacturer. Consequently, only a general comparison can be made between the two studies. An investigation of the differences introduced by just tread design alone could be a separate research endeavor. The tire behavior depicted in Figures 49 and 50 is what is expected of a typi-

cal tire's lateral force when subjected to increasing slip angle. An example of an ideal lateral force verses slip angle curve is depicted in Figure 51. The lateral force data collected by the author also fits well with the data collected by Holloway *et al.* [1] at the University of Maryland. Figure 52 depicts an example of the lateral force data collected during Holloway's study.

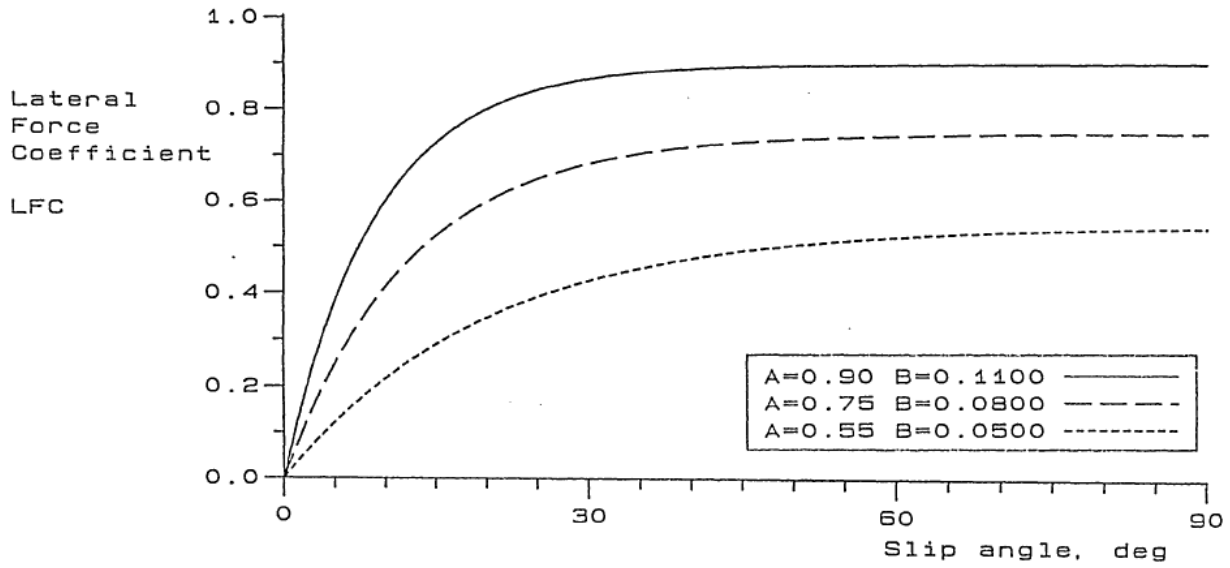

Figure 51. Idealized normalized lateral force versus slip angle for a free spinning tire on different surfaces [9]

Again, the graph starts with a linear increase and then reaches a break point where the lateral force increase slows and then assumes a near steady value as the slip angle is increased.

The longitudinal force data collected by the author also compares well to expected results. Figure 53 depicts Milliken's data of longitudinal force verses slip ratio for increasing slip angles. The force curves in Figure 53 were constructed using data collected on a Flat Trac machine under laboratory conditions. Therefore, results in Figure 53 can be considered an ideal form of the relationship for comparison to data collected in the field in this study. The key points

to note in Figure 53 are the linear force increase until the slip ratio reaches about 0.3, the peak force point after which the force decreases slightly and reaches a steady value, and the way the peak force occurs at higher slip ratios as the slip angle is increased. The longitudinal force data collected by the author also displayed these characteristics. An example of the author's data can be seen in Figure 54.

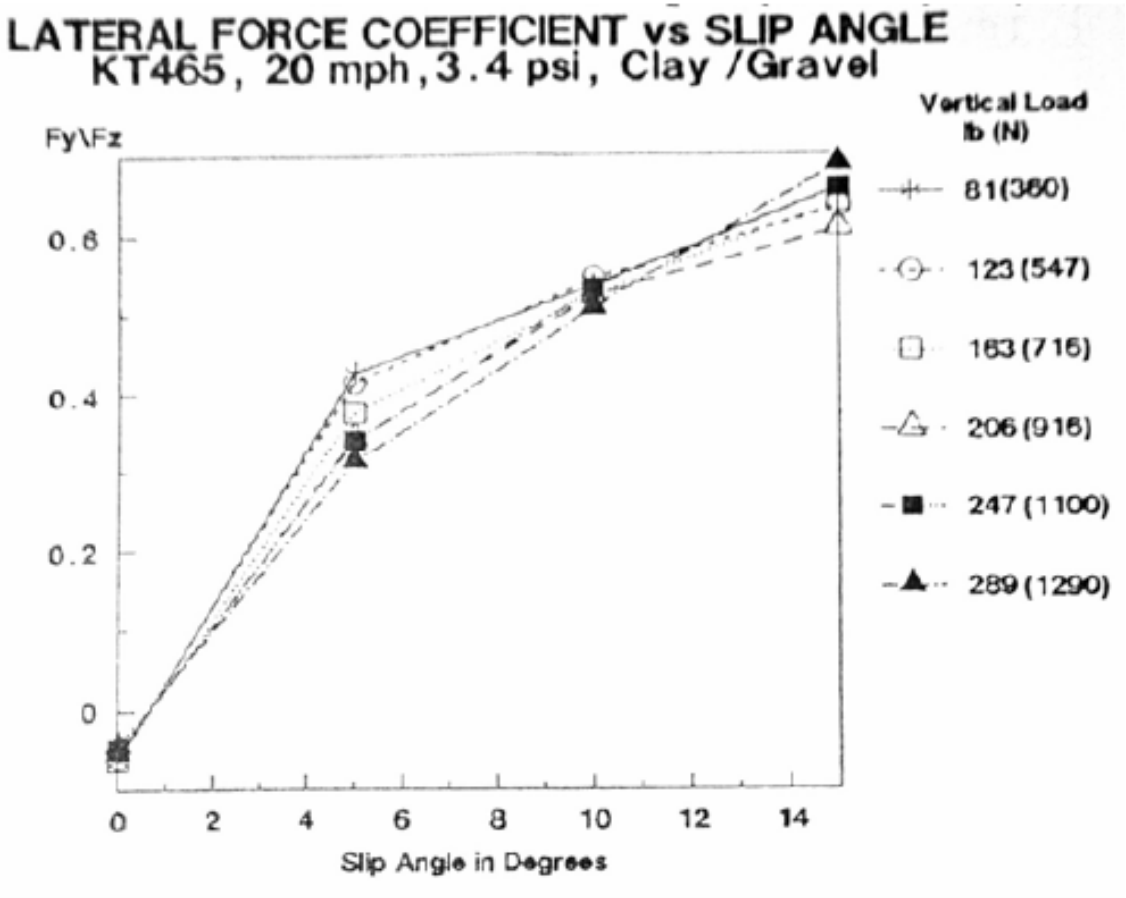

Figure 52. Normalized lateral force versus slip angle from the study by Holloway et al. [1]

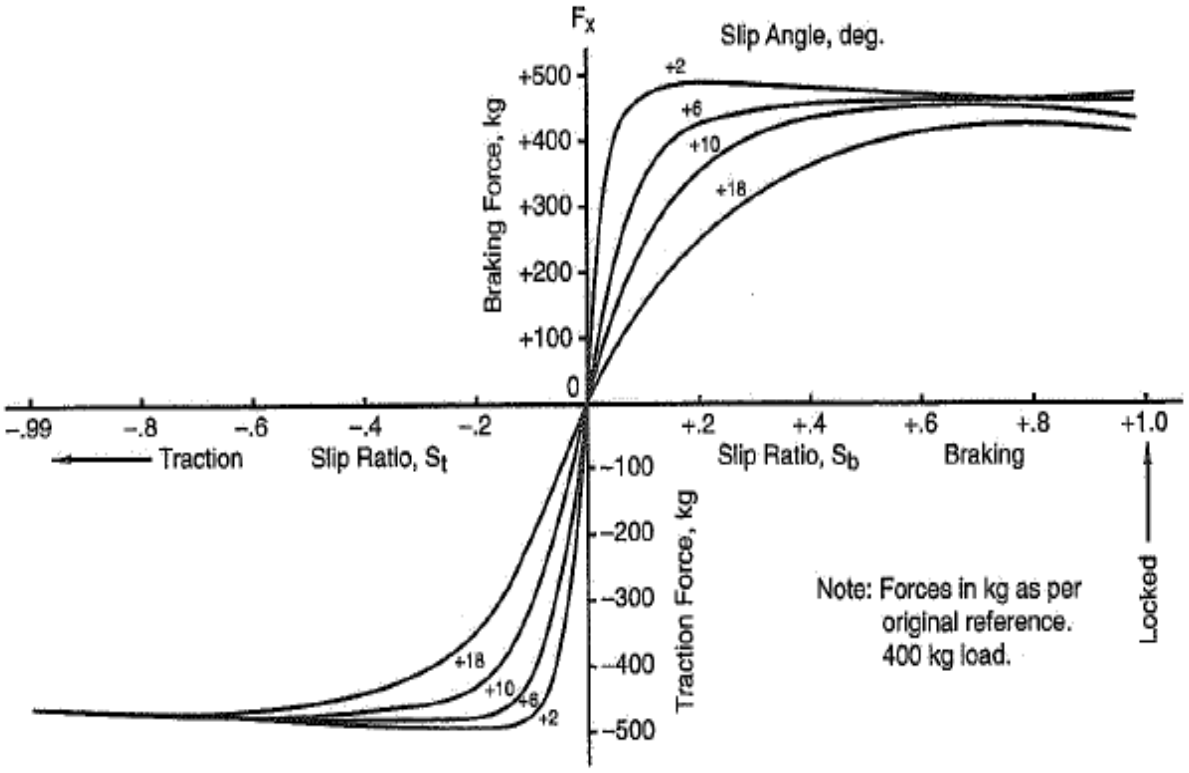

Figure 53. Longitudinal force versus slip ratio for increasing slip angle [3]

The expected linear increase to a nominal saturation value is present and increase of the slip ratio needed for the peak force value for increasing slip angle is also present. The agreement of the results of this study with results of previous studies confirm that the data collection of this study was successful and the data is usable within the context of tire force generation.

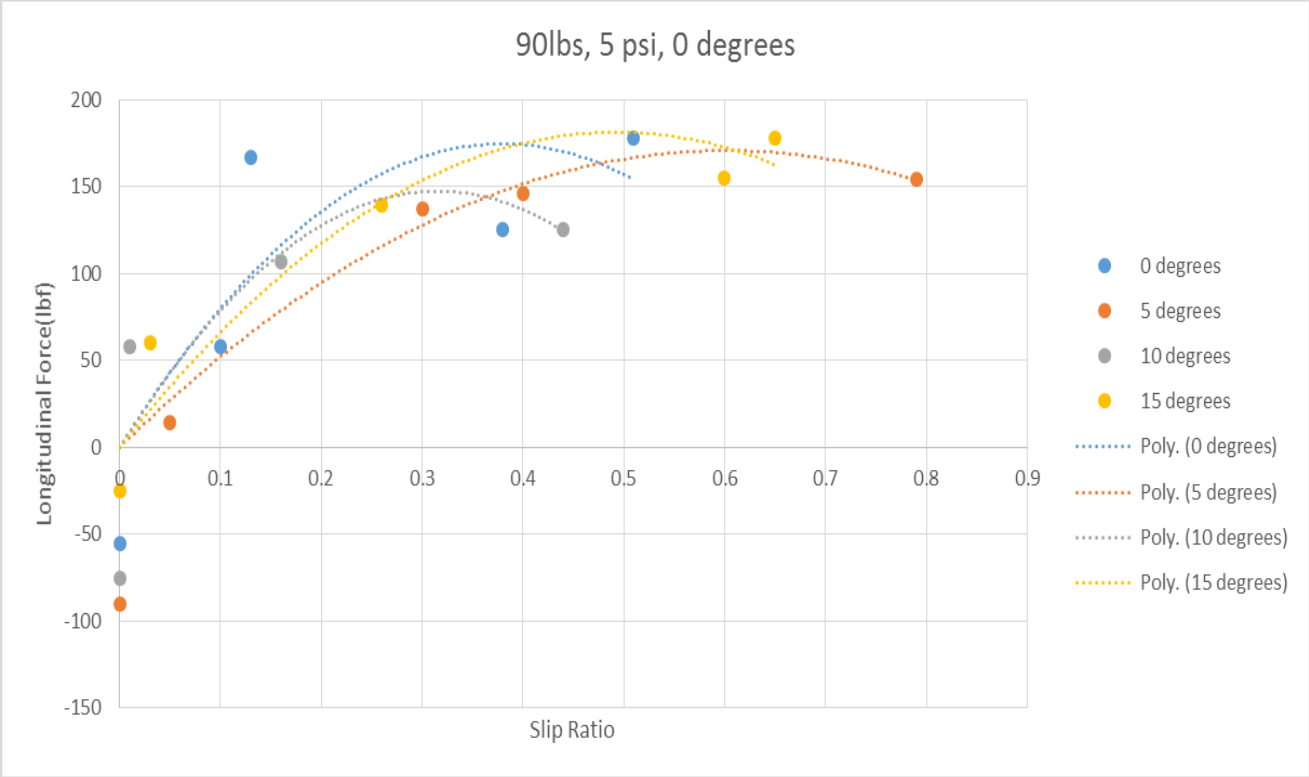

Figure 54. Longitudinal force versus slip ratio for increasing slip angle measured during this study

3.2 Uncertainty

All measurements come with a degree of uncertainty. Uncertainty arises from two main sources: random errors and systematic errors. Random errors in the context of this study will include factors such as micro changes in elevation on the test surface, rocks located just below the soil surface, uneven moisture distribution in the soil, minor day to day variance in soil moisture content, and other mainly environmental factors. Environmental factors can only be partially mitigated. The test surface was smoothed as much as possible in order to reduce the impact of sudden elevation changes and any visible rocks and debris were removed. However, the area that was chosen for the test surface has an approximately 0.5% grade running from north to south that could not be removed with the tools available. The sloping grade was compensated for by com-

bining a downward slope run and an upward slope run into each complete test run. The data collected from each portion can be easily compared and an average force value can be computed that removes any biasing that would occur if all of the runs were done in the same slope direction. The issues involving the soil moisture content were mitigated as much as possible by allowing the test track to dry for at least two days after any significant rainfall. The soil was also checked prior to commencing of any test runs to see if it felt dry to the touch. If the soil felt damp, no test runs would be conducted until the soil dried.

Systematic errors are errors introduced into research from equipment and data collection procedures. Systematic error can cause biasing in the data that must be removed during post processing or during calibration. Examples of systematic errors include zero offsets of load cells and low speed detection resolution of the Hall Effect sensors. Systematic errors in this study were mitigated using the calibration procedure described in section 2.1.4.

Error mitigation helps to greatly reduce the uncertainty in data. However, the very nature of the data collection process will always introduce some degree of variance in the data collected. This concept of data variance is illustrated in Figure 55. Figure 55 also depicts the importance of error minimization to ensure a true representation of the data's mean. After large errors from the sources mentioned above have been removed, it is necessary to quantify the remaining variance in order to fully describe experimental results. The standard error method was selected to quantify this variance.

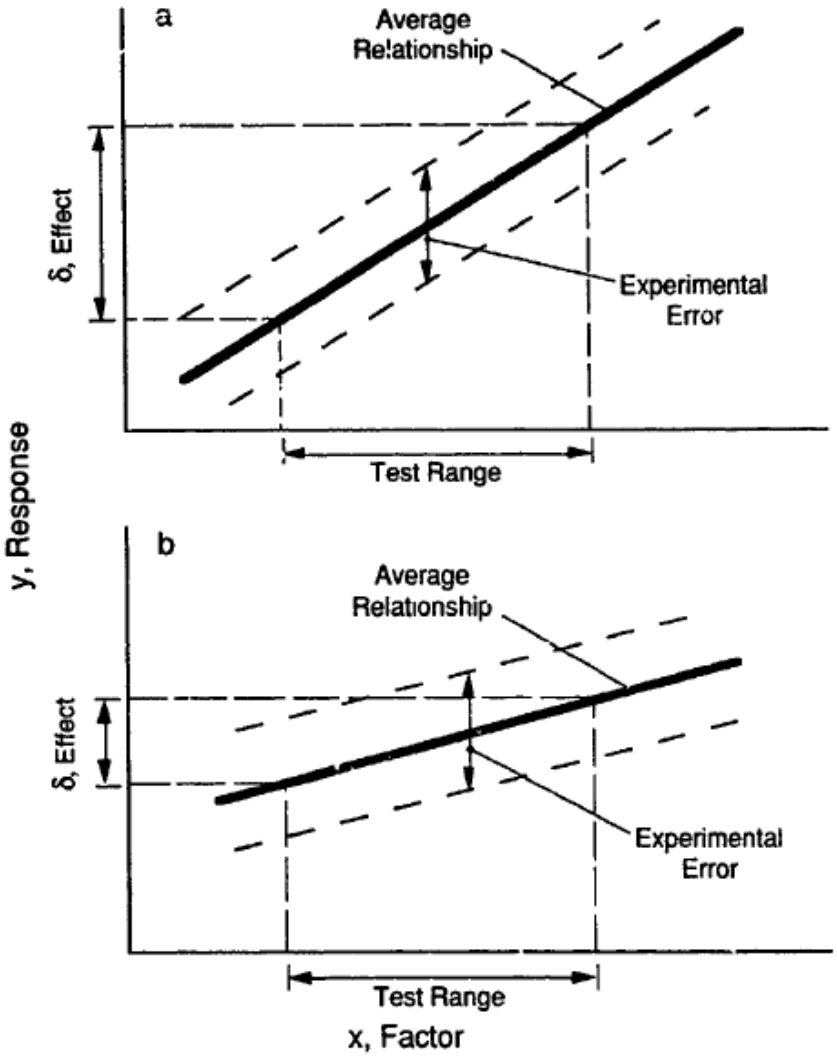

Figure 55. Data variance caused by experimental error [23]

The standard error provides an unbiased estimate of the standard deviation of the sample mean based on the population mean [22]. The standard error method is based upon the data having a Gaussian distribution. It is a robust method however, so the data being analyzed does not have to have a perfect Gaussian distribution [22]. The first step in the standard error method is ensuring that the data is close enough to a normal distribution for the method to be utilized. The normalcy of the data was tested using the graphical method described by Shoop [23]. First the

data is organized in ascending order and a *p* value is assigned to each data point. The first data point is assigned the value $\frac{100}{2n}$, where *n* is the number of data points. Each subsequent point is assigned a value based upon Equation 17 [23].

$$P_i = P_{i-1} + \frac{100}{n} \tag{17}$$

The data and the corresponding *p* values are then plotted on a semi-log graph as shown in Figures 56-58. A logarithmic best fit line is then applied to the data. The best fit lines are not perfect in any of the Figures, but the close proximity of most of the data points to the linear trend does indicate that the data is close enough to a normal distribution for the standard error method to be applied.

With the assumption of a normal distribution established, the standard deviation can be computed and Equation 18 can be used to calculate the standard error for the force readings [22].

$$S_E = \frac{\widehat{\sigma}}{\sqrt{n}} \tag{18}$$

The standard error was calculated to be ±4.4 lbf (19.6 N) for the force readings. The standard error of this study is very close to the standard error of 4 lbf (17.8 N) calculated by Krueger [2] for his force measurements collected with a similar device under approximately the same conditions. A similar approach was taken to ascertain the standard error for the Hall Effect sensor readings. Figure 59 depicts the best fit line on the semi-log plot of slip ratio versus *p* values computed from the Hall Effect sensor readings. Again, the assumption of a normal distribution is sufficient enough to allow for the use of the standard error method. The standard error for the slip ratio measurements was calculated to be ±0.05.

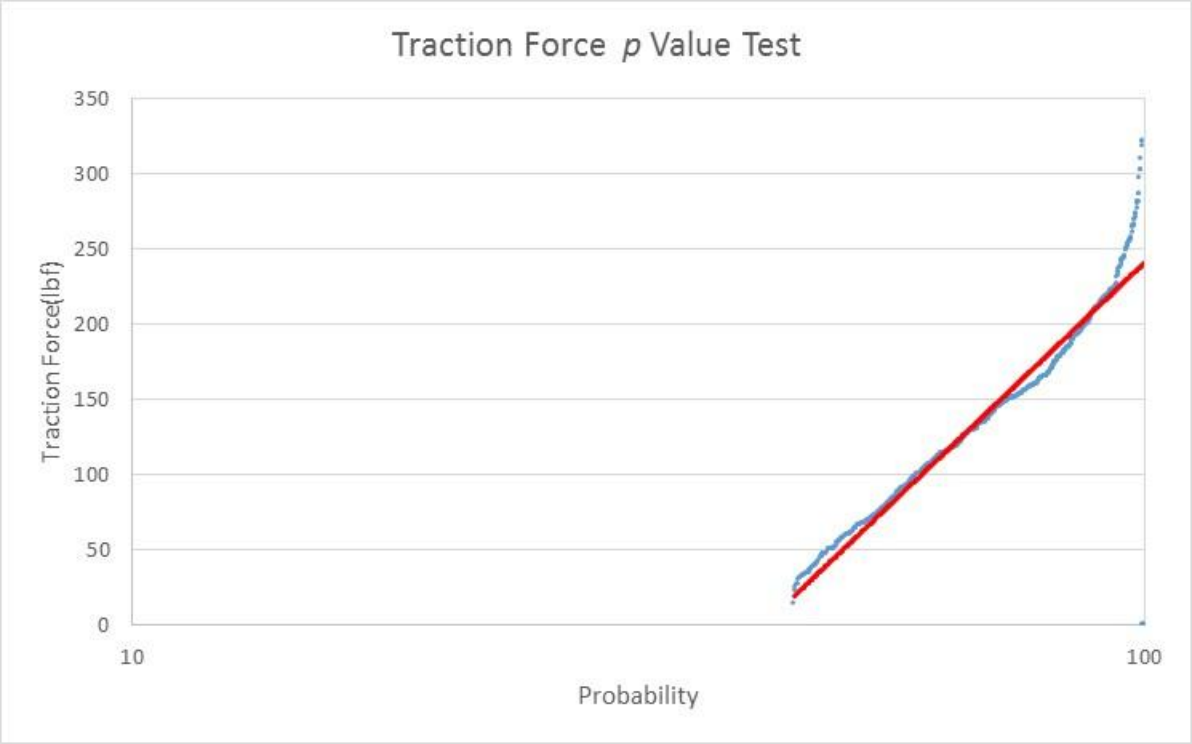

Figure 56. Traction force probability plot

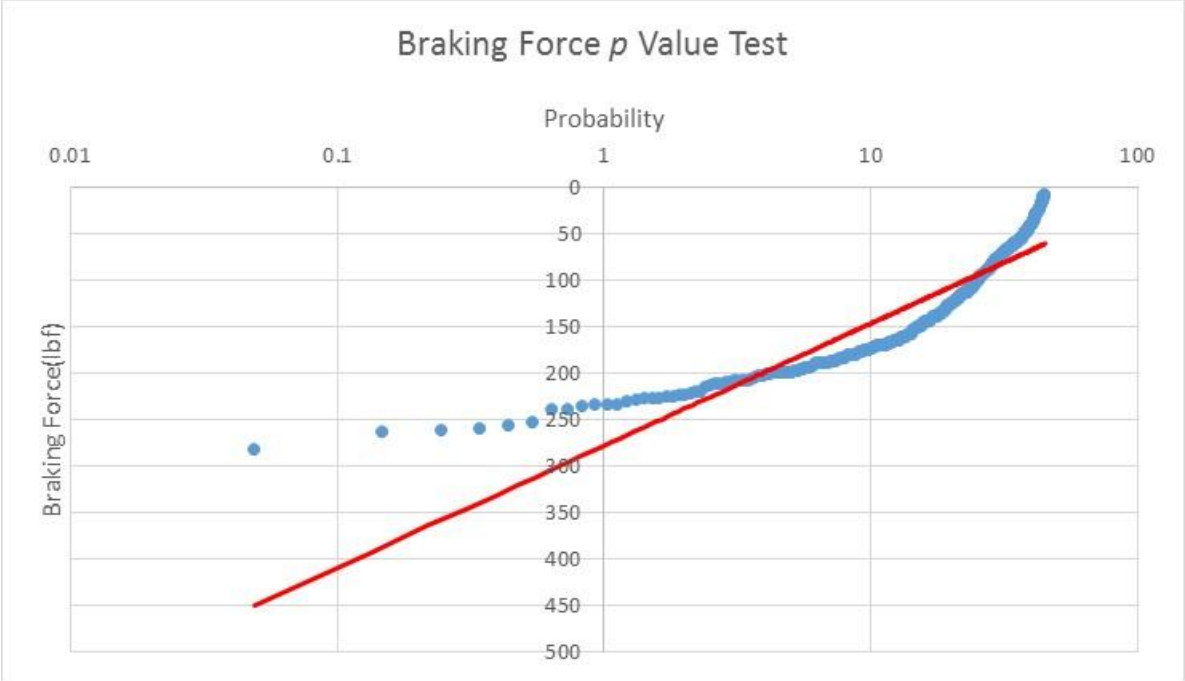

Figure 57. Braking force probability plot

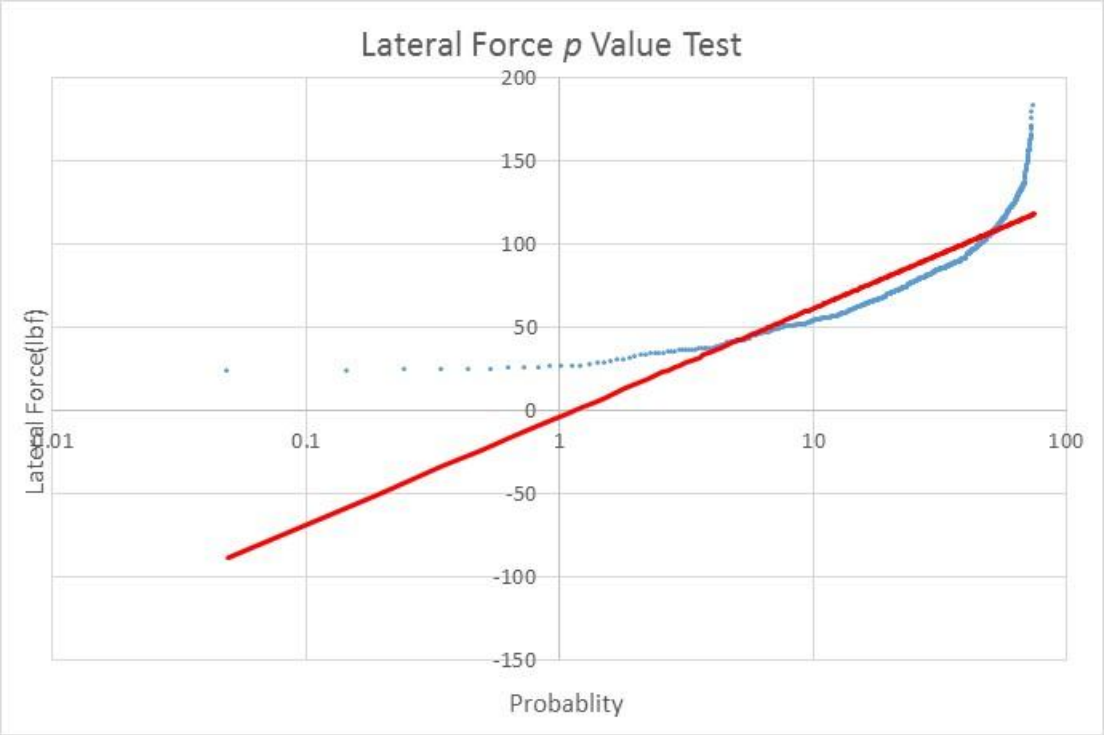

Figure 58. Lateral force probability plot

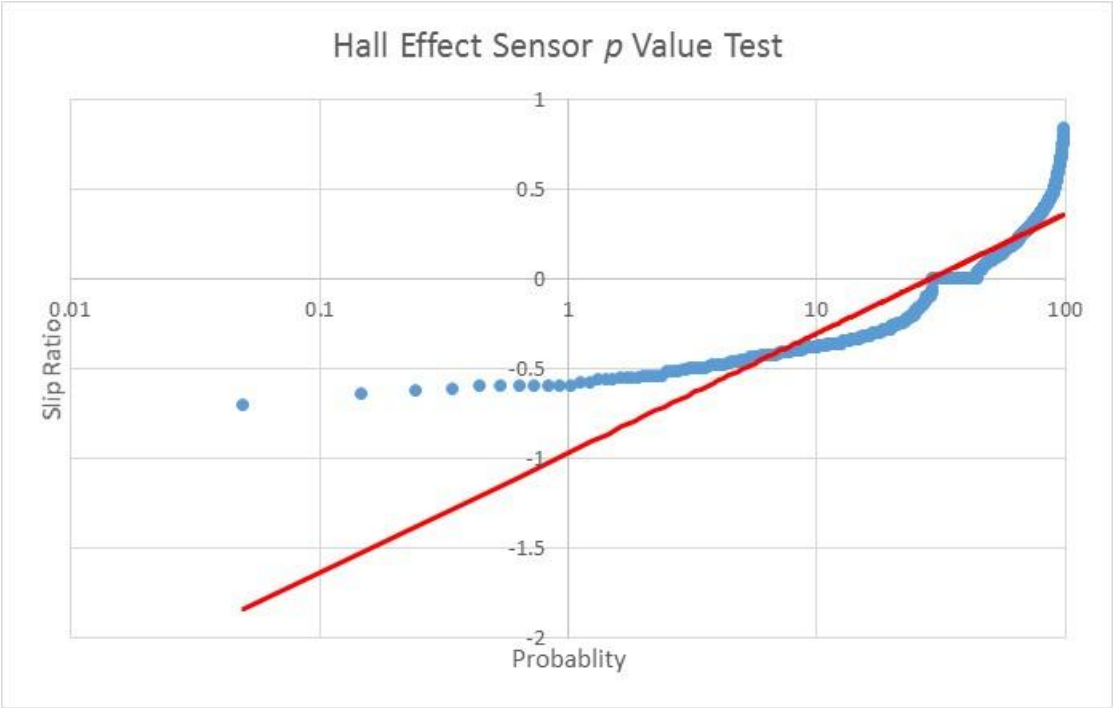

Figure 59. Slip ratio probability plot

3.3 Test Surface

The test surface soil was characterized using the method described in section 2.2. Separate test runs were conducted to measure the longitudinal force for each normal load with a free spinning tire and a tire subjected to between 10-15% slip ratio. The data from these test runs was reduced to a peak and an average force value in the same manner as described in section 2.3. The contact area for the tire under each applied normal load was measured by coating the tire in red marking chalk and then making a tire imprint on a piece of white paper. An example of these imprints can be seen in Figure 60.

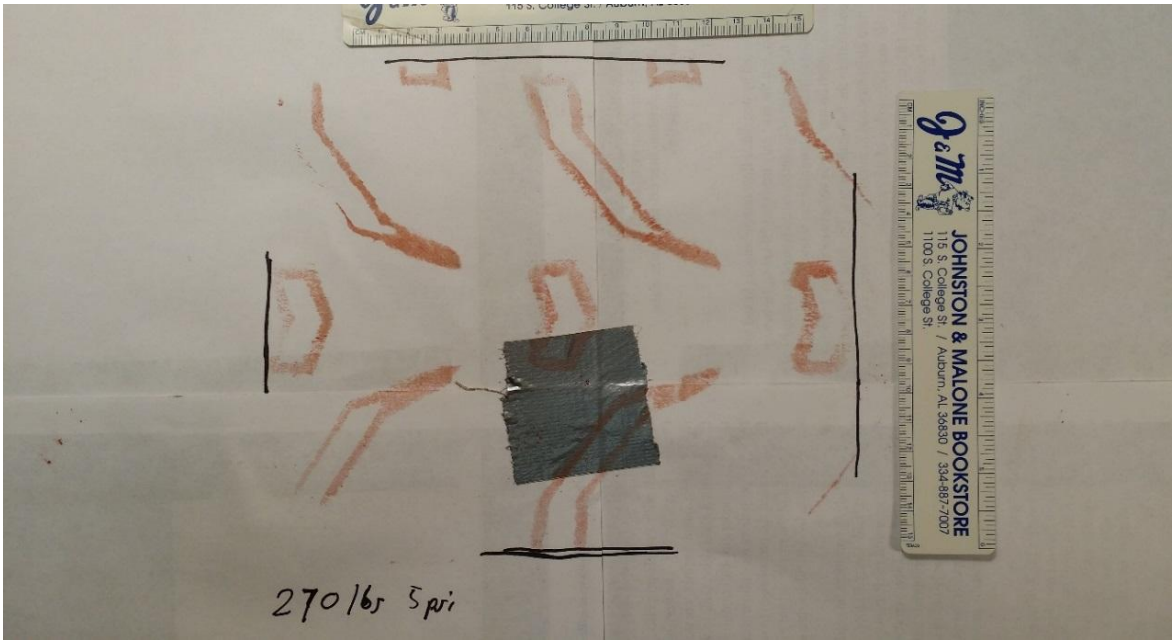

Figure 60. Tire contact print taken with marking chalk

The length and width of each imprint was then measured and a contact area was calculated. A summary of the calculated tire contact areas for each normal load is presented in table 2.

Table 2. Tire Contact Area measured for Applied Normal Loads at 5 psi (34.5 kPa) tire pressure

Additional Normal Load		Contact Area	
lbf	N	ft^2	m^2
45	200.2	0.166	0.015
90	400.3	0.245	0.023
135	600.5	0.298	0.028
180	800.6	0.322	0.030
225	1000.8	0.342	0.032
270	1201	0.363	0.034

The impressions were made with the tire inflated to 5 psi (34.5 kPa). Surface characterization test runs were also conducted at 5 psi (34.5 kPa) inflation pressure. The normal and shear stress acting at the tire surface interface can then be calculated using the contact area and the measured forces. The plot of the shear stress versus normal stress is shown in Figure 61. A linear best fit line was applied to the data and the friction angle and cohesion of the soil were calculated using Equation 6. The friction angle of the surface is 9.24 degrees and the cohesion is 203.63lbf/sqft (9.75 kPa). These surface characteristics were then compared to results reported by Holtz and Kovacs [14]. A surface with the above characteristics can be described as a semi-soft, over consolidated clay. The term soft in this case refers to the number of blows per foot of depth that are required from an industrial pile driver. The soil would be considered hard when touched, but is considered in the soft range with regards to the standard civil engineering soil characteristics. The above description fits well the test soil surface as it is composed of fine particles typical of clay soils. The test soil surface is over consolidated because it was compacted repeatedly by the Yamaha Rhino prior to commencing the test runs.

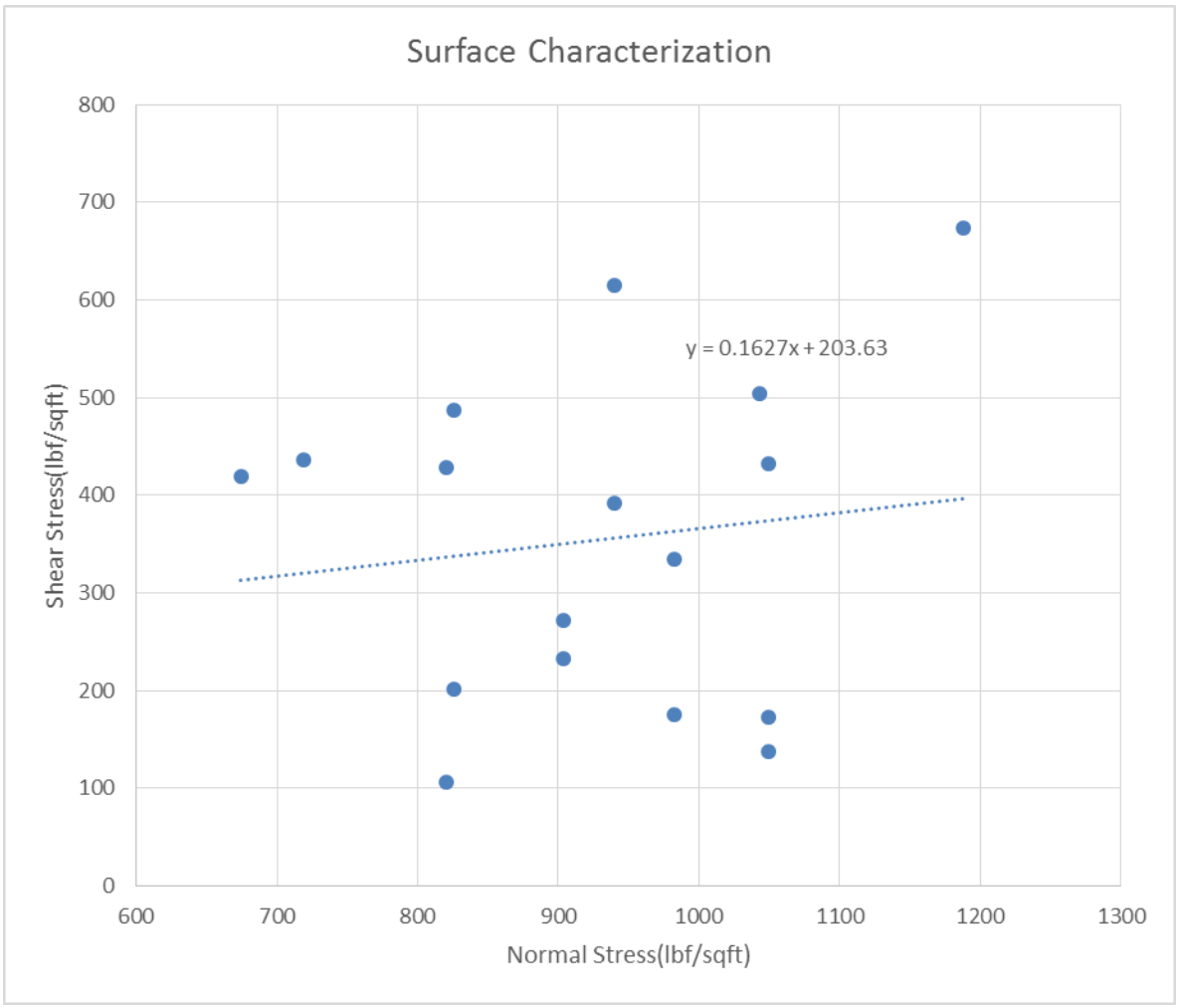

Figure 61. Shear stress versus normal stress used for the determination of the surface characteristics

The process of over consolidation packs the particles of the clay more tightly together driving out excess water, which makes the surface more resilient than a similar undisturbed clay [14].

The testing matrix of the test soil surface was constructed based upon requirements for adjusting the test setting of the instrumented tire apparatus. The easiest setting to adjust is the instrumented tire motor throttle. Each test series included seven complete test runs with two braking, four traction, and one free rolling run. The sets were all conducted at one slip angle setting in order to efficiently use testing time as the slip angle adjustment required more time and

effort to change especially at high normal loads. The test sets were arranged into blocks separated by the time required to change tire inflation pressure and tire camber setting. The tire camber setting was the most difficult to change requiring two individuals. The test matrix was organized to minimize the number of camber adjustments required to collect the necessary data. A total of 1036 test runs were conducted. The test matrix is presented in Table 3.

Table 3. Testing Matrix

Motor Setting Slip angle	Test Block 1	Test Block 2	Test Block 3	Test Block 4	Test Block 5	Test Block 6
0 0,5,10,15	7 psi* 0 degrees	2 psi* 0 degrees	5 psi* 0 degrees	5 psi 8 degrees	7 psi 8 degrees	2 psi 8 degrees
-2 0,5,10,15	7 psi 0 degrees	2 psi 0 degrees	5 psi 0 degrees	5 psi 8 degrees	7 psi 8 degrees	2 psi 8 degrees
3 0,5,10,15	7 psi 0 degrees	2 psi 0 degrees	5 psi 0 degrees	5 psi 8 degrees	7 psi 8 degrees	2 psi 8 degrees
-1 0,5,10,15	7 psi 0 degrees	2 psi 0 degrees	5 psi 0 degrees	5 psi 8 degrees	7 psi 8 degrees	2 psi 8 degrees
2 0,5,10,15	7 psi 0 degrees	2 psi 0 degrees	5 psi 0 degrees	5 psi 8 degrees	7 psi 8 degrees	2 psi 8 degrees
1 0,5,10,15	7 psi 0 degrees	2 psi 0 degrees	5 psi 0 degrees	5 psi 8 degrees	7 psi 8 degrees	2 psi 8 degrees
4 0,5,10,15	7 psi 0 degrees	2 psi 0 degrees	5 psi 0 degrees	5 psi 8 degrees	7 psi 8 degrees	2 psi 8 degrees
* 7 psi (48.3 kPa), 2 psi (13.8 kPa), 5psi (34.5 kPa)						

3.4 Tire Forces

3.4.1 Lateral Force

The lateral force production of the tire can be separated into three distinct parts. The lateral force initially increases linearly in what is referred to as the linear tire region. The linear tire region is the portion of the graph that depicts the tire's cornering stiffness, C_{α}. The lateral force then enters a transitional region where the rate of increase slows and then in the final part flattens

into a near constant value governed by the frictional forces between the tire and the soil surface. The region of the graph after the force saturation point is known as the frictional region. The lateral force results determined in this study follow the basic expected trends. Figure 62 depicts the lateral forces that were recorded from a series of test runs conducted at a normal load setting of 135 lbf (600.5 N) and a camber setting of 0.

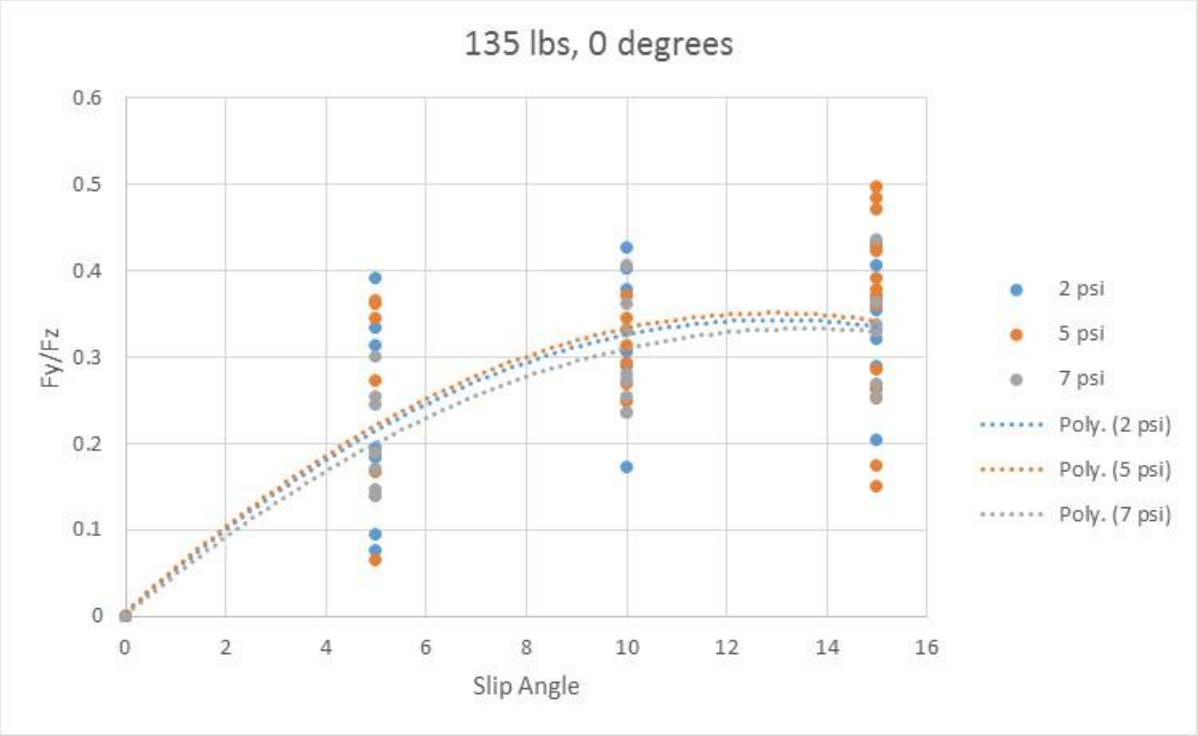

Figure 62. Normalized lateral force versus slip angle for varying pressure

Note how all of the expected force regions are present for each pressure setting. A 2nd order curve fit was applied to the data. The force increases linearly until reaching a saturation force that occurs at approximately 15 degrees slip angle. The peak force is reached at the same slip ratio for each pressure setting. Another important trend that was noticed is that the highest forces occur at 5 psi (34.5 kPa) inflation pressure while 7 psi (48.3 kPa) inflation has the lowest recorded forces. Two psi (13.8 kPa) inflation pressure produces forces between 5 psi (34.5 kPa) and 7

psi (48.3 kPa). The observed trends hold for the lateral force until the camber is changed to 8 degrees. The camber effects will be discussed in more detail in a later section.

3.4.2 Longitudinal Force

The longitudinal force or traction force produced by the tire is expected to increase as the slip ratio is increased. The longitudinal force follows a similar trend to the lateral force with a linear increase in force until a saturation force is approached. Once the saturation force is reached, the longitudinal force will then decrease as the slip ratio increases further. The tire will eventually begin to spin as the slip ratio exceeds 1. The slip ratio at which the maximum longitudinal force occurs is also expected to increase as slip angle is increased [3].

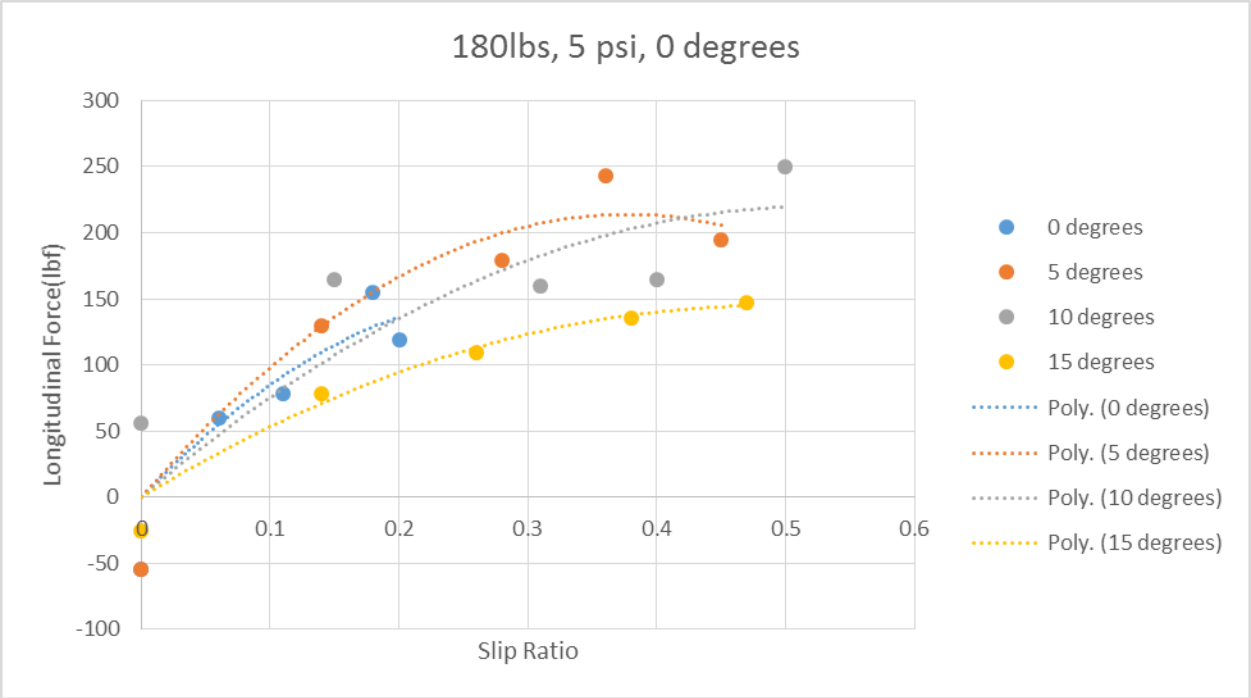

Figure 63. Longitudinal force or traction force versus slip ratio for varying slip angle

Figure 63 depicts the longitudinal force or traction force plotted against the slip ratio for the 180 lbf (800.6 N) normal load setting, 5 psi (34.5 kPa) tire inflation pressure, and 0 camber angle. The expected trends are present. At each slip angle, the force increases linearly and then reaches a saturation force where the increase stops. The saturation point occurs at higher slip ratios for increasing slip angle. The results for the traction force were overall not as uniform as the lateral force results. A clear force saturation point was not observable in some of the test settings. There is also more scatter to the data points that is most likely caused by test surface deformation and by the difficulty in maintaining a constant slip ratio. The slip ratio was observed to vary even with the motor throttle kept at a constant setting. The measured slip ratio could vary by ±0.1 within a single test run. The author had difficulty in reaching slip ratios of approximately 0.6 and greater, as the instrumented tire motor setting needed to reach these high slip angles would cause the instrumented tire apparatus to oscillate vertically. The oscillations could be large enough to damage the instrumented tire apparatus especially at lower normal load settings. An example of the variance and lack of clear saturation points is depicted in Figure 64.

The braking force that is generated by the tire is expected to display similar trends to the traction force. The braking force should increase linearly and reach a saturation point in much the same way as the traction force. The main difference observed in on-road tests [3] is the peak braking force occurs at a lower slip ratio than for a traction force and the trend holds for increasing slip angle. Figure 65 depicts the plotted braking force versus slip ratio for the test runs conducted at 225 lbf (1000.8 N) normal load, 7 psi (48.3 kPa) tire inflation pressure, and 0 camber angle.

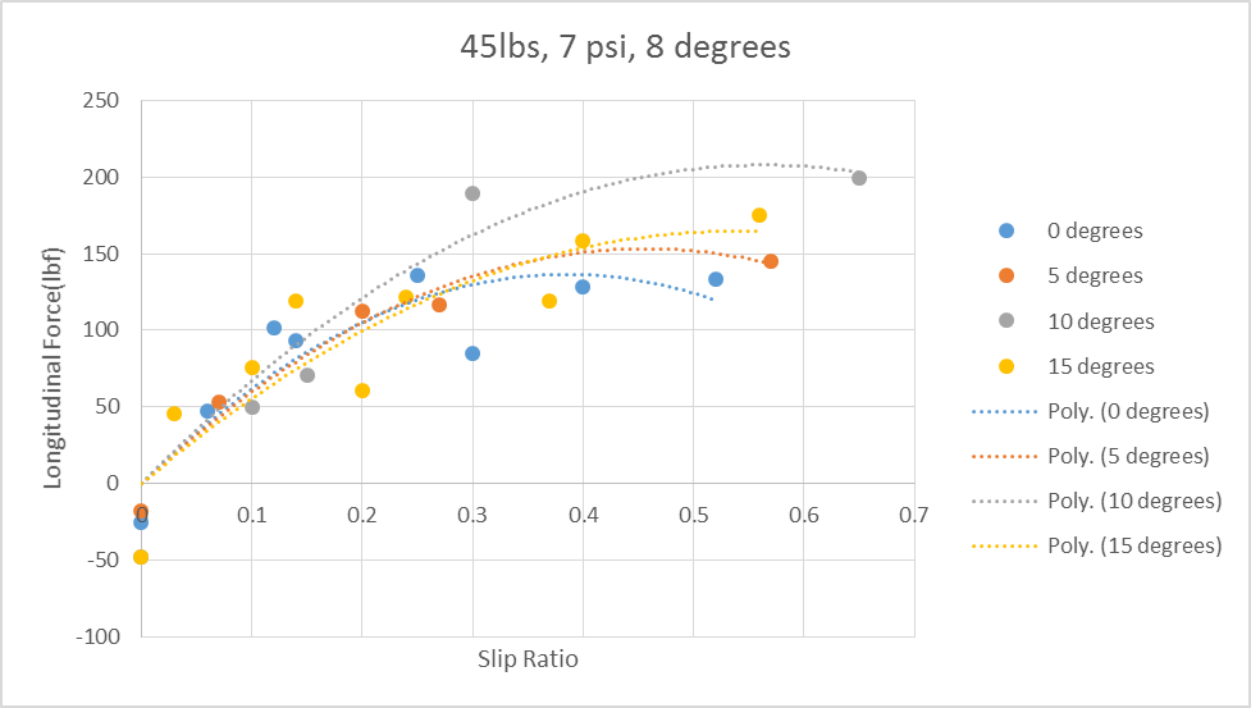

Figure 64. Scatter in the traction data caused by oscillations of the machine at low normal loads

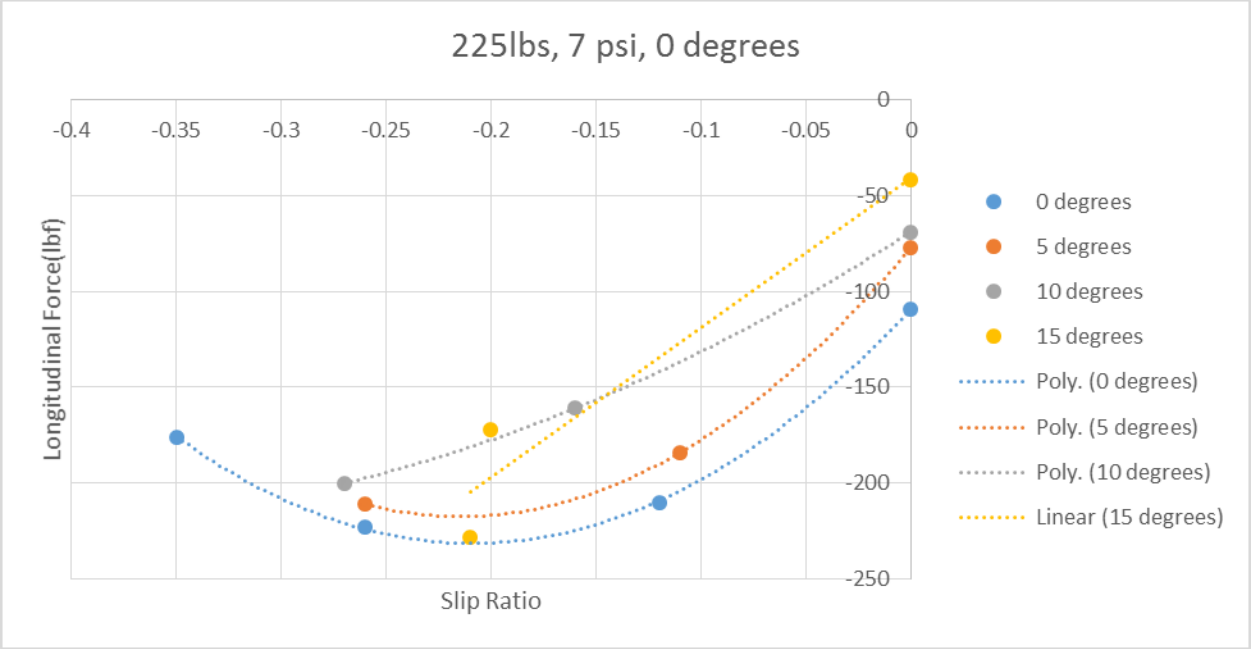

Figure 65. Braking force versus slip ratio for varying slip angle

The expected trends are present in the study braking force data. A linear increase occurred with the expected saturation point. The increasing slip ratio for peak force at increasing slip angles is also present. The braking force also decreases as the slip ratio is increased similar to the traction force. Slip ratios less than -0.5 were difficult to obtain. The tire test apparatus proved to be very sensitive to small changes of the instrumented tire motor throttle when used in the braking configuration. Full wheel lock could be achieved at all normal load settings higher than 90 lbf (400.3 N) with a throttle input of approximately 33%. A 5% increase over a 33% throttle setting would cause the tire to start rotating opposite to the direction of travel. Obtaining slip angles between -0.05 and -0.1 were also difficult to produce consistently. A throttle input change of less than 5% could make the difference between soft and hard braking. The sensitivity to changes in the applied braking force increased as the normal load was increased.

3.5 Pressure and Camber Effects

3.5.1. Pressure Effects

The tire inflation pressure has already been shown to have a significant impact to the forces that are produced by the tire in this study. The tire contact area and vertical stiffness are both dependent on tire inflation pressure. Figure 66 shows the lateral force versus the slip angle plotted for each normal load for different inflation pressures. The graph lines indicate for 0 camber angle, the 5 psi (34.5 kPa) tire inflation pressure produces the greatest lateral force and 7 psi (48.3 kPa) tire inflation pressure the least. The lateral force produced by 2 psi (13.8 kPa) tire inflation pressure falls between that of the other two tested pressures. The main reason for the observed behavior is the increase in the tire contact area as the inflation pressure is decreased. The

increased area gives the tire a larger footprint with which to push against the ground. Thus, 5 psi (34.5 kPa) and 2 psi (13.8 kPa) tire inflation pressures have higher recorder force than the inflation pressure with the smallest contact area, 7 psi (48.3 kPa). The pressure differences also highlight another aspect of the tire that can influence force production, which is carcass stiffness. At 2 psi (13.8 kPa) tire inflation pressure, the tire was observed to deform more significantly than at 5 psi (34.5 kPa) or 7 psi (48.3 kPa) . The large amount of deformation meant the tire is not receiving the full benefit of its pneumatic characteristics and the carcass stiffness is the main factor in supporting the applied normal load. The carcass stiffness also produces internal tire friction force that must be overcome in order for the tire to roll forward.

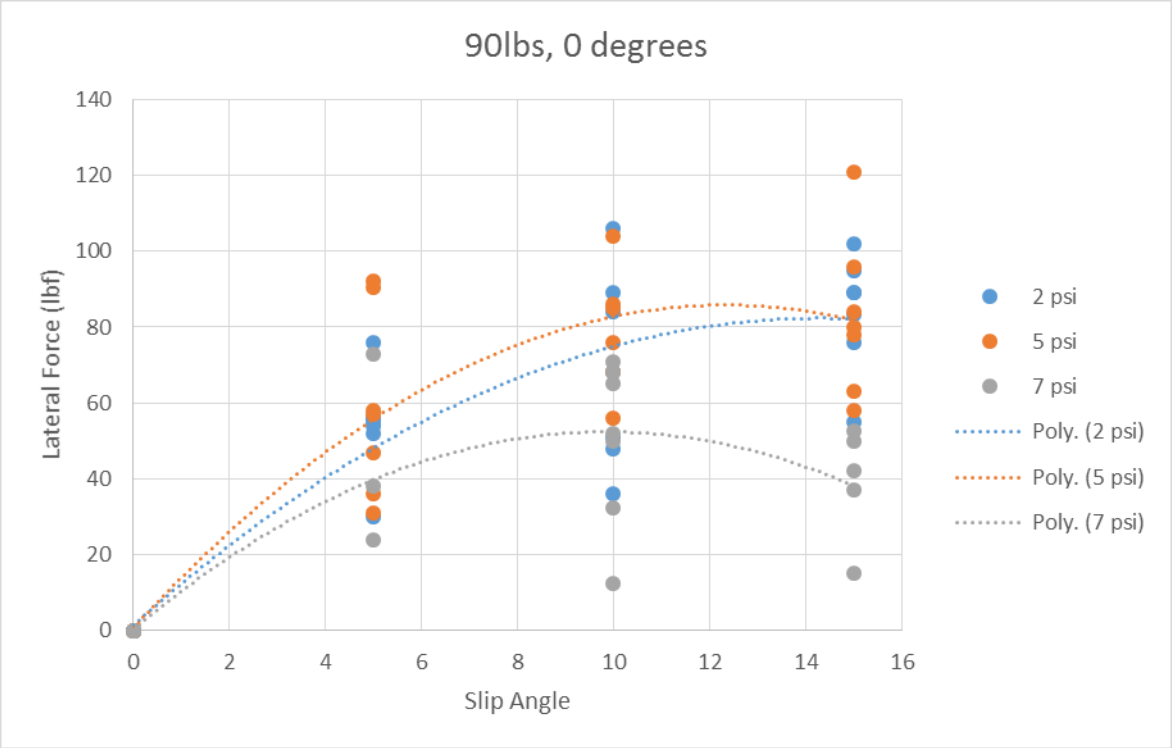

Figure 66. Change in lateral force caused by changes in inflation pressure

Internal friction is caused by the rubber the tire is made of stretching and compressing. The internal friction force cancels much of the additional force that could be produced from the larger tire contact area. Five psi (34.5 kPa) tire inflation pressure appears to be the optimum pressure of those tested at 0 camber angle since it allows for greatest observed lateral force production without having significant internal friction losses.

Tire inflation pressure has a similar effect on the longitudinal force produced by the tire as it has on lateral force. An increase in the contact area of the tire is the main factor that contributes to the increased force at lower inflation pressures for the longitudinal force as well. The internal tire friction also plays the same role as the pressure decreases past the point of effective pneumatic performance for the test tire. Internal friction begins to take away from the longitudinal force production in the same way that it does for the lateral force. Figures 67 and 68 depict changes in traction force as tire inflation pressure is changed.

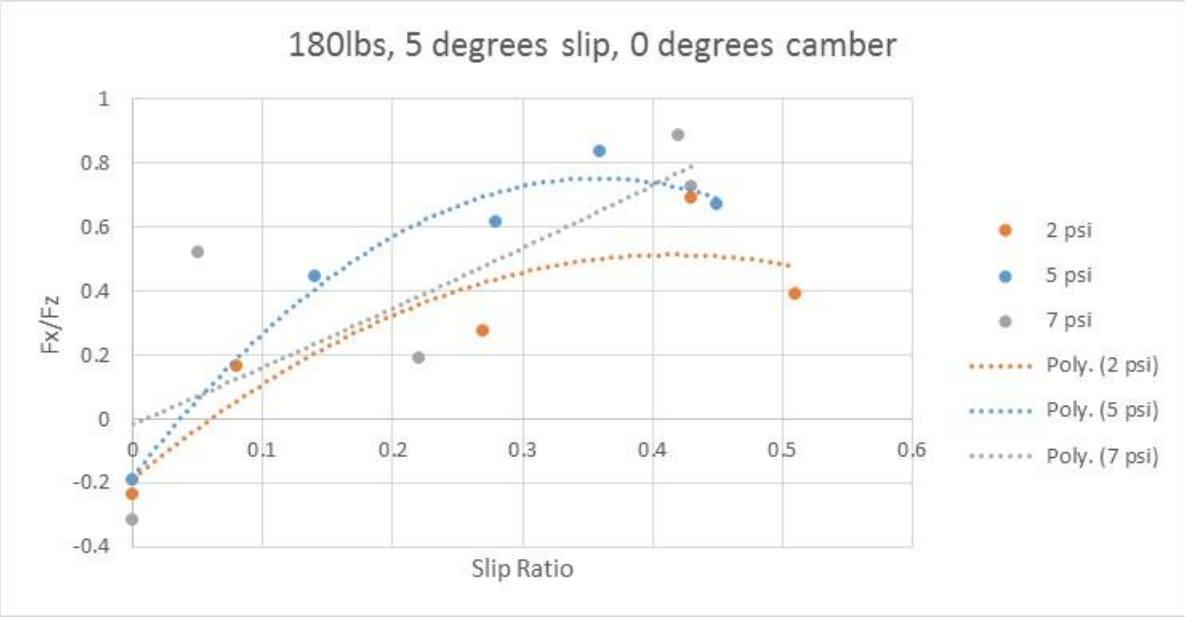

Figure 67. Changes in traction force caused by changes in inflation pressure

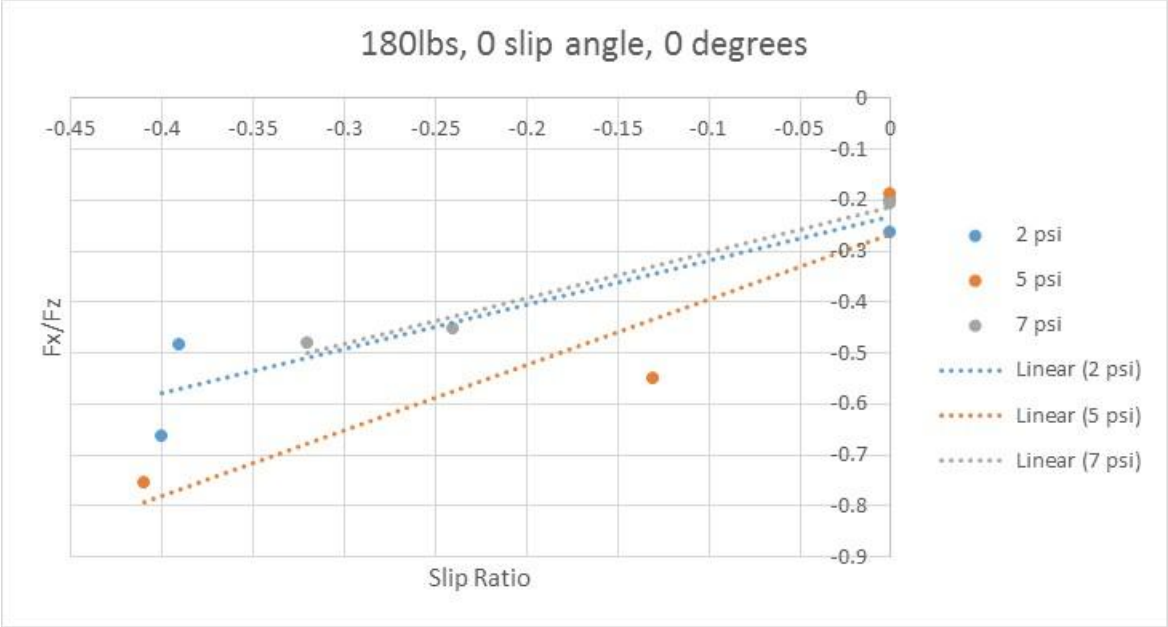

Figure 68. Changes in braking force due to changes in inflation pressure

Again, 5 psi (34.5 kPa) tire inflation pressure produces the greatest traction force with 2 psi (13.8 kPa) tire inflation pressure producing the least and 7 psi (48.3 kPa) tire inflation pressure traction forces between the other two pressures. The traction force is reduced more by the internal losses caused by carcass deformation than the lateral force. A similar trend is also observed with braking force.

3.5.2 Camber Effects

The addition of camber, or angling a tire towards or away from the vehicle body, is a well-established method of changing the performance characteristics of many types of on-road vehicles [3, 20]. The same method can be applied to off-road vehicles as well. The main effect of placing the tire at a camber angle is increasing the contact area [1, 2]. An increase in tire contact area in general gives rise to an increase in the available longitudinal and lateral forces. Increased

forces are especially true when the tire is at a higher inflation pressure and at higher normal loads. The increase in the available longitudinal and lateral force can be seen in Figures 69 -71. Note how the traction and lateral force production increases with the change in camber for a tire at the same normal load and pressure. Figures 71- 73 illustrate how changing camber can have a significant impact on the off-road vehicles performance when factors such as the normal load and inflation pressure cannot be changed. The addition of camber is less significant for tires that have lower normal loads and lower inflation pressures. Krueger [2] noted reduction in camber influence in his study on a free rolling ATV tire and it has also been observed for tires that are subject to traction and braking forces. Figures 72-74 show such a case with low normal load and low inflation pressure. The addition of camber does increase available lateral force at lower normal loads and lower inflation pressures, but it is much less significant than for higher pressures and normal loads.

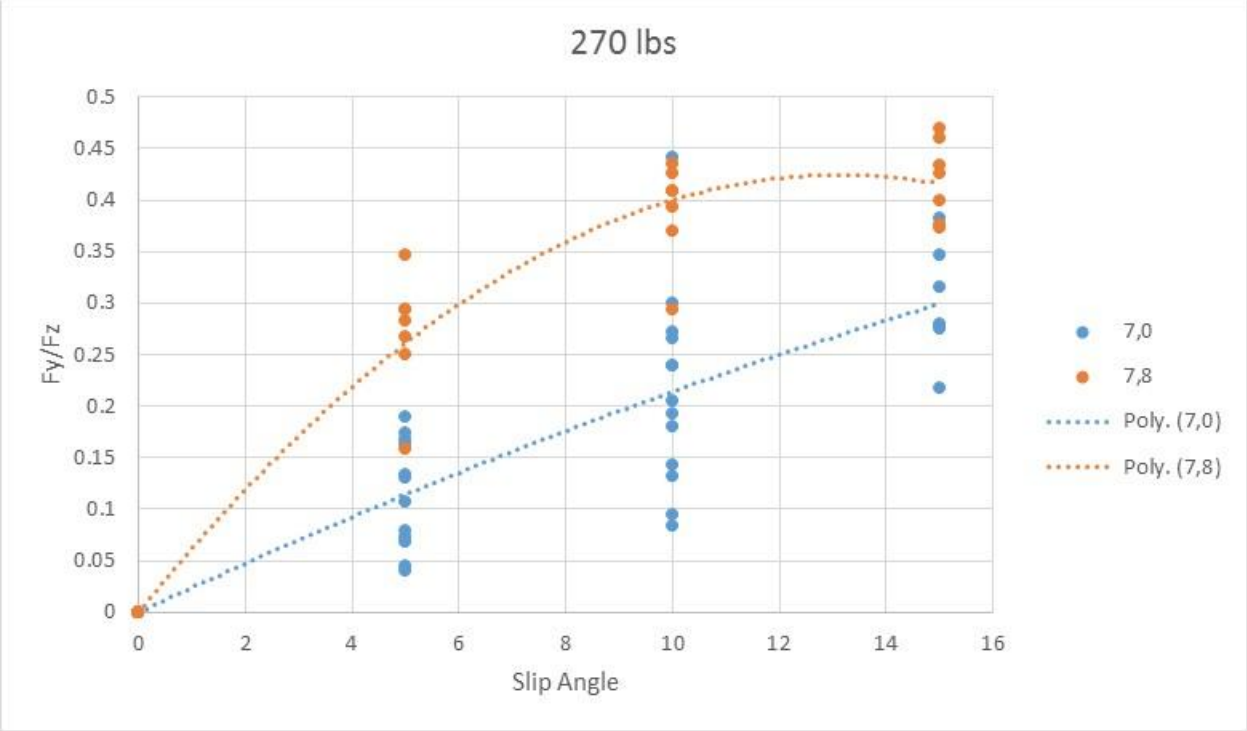

Figure 69. Change in lateral force caused by change in camber

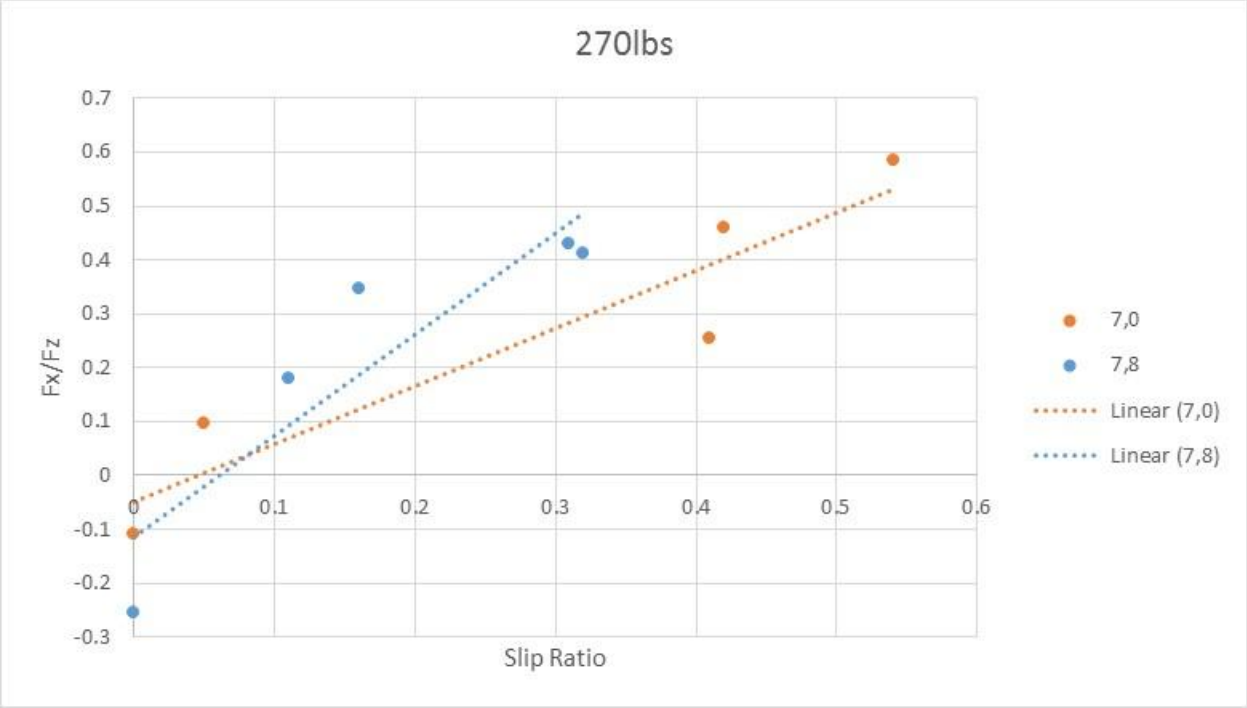

Figure 70. Change in traction force caused by change in camber

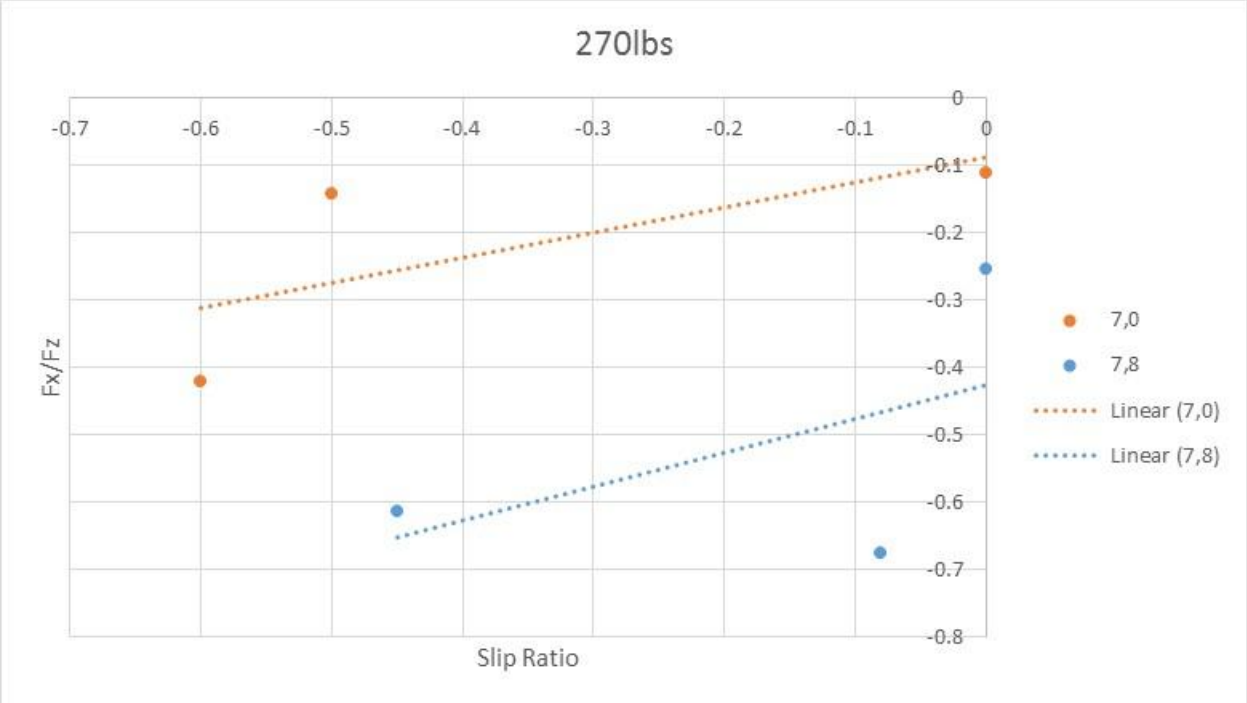

Figure 71. Change in braking force due to change in camber

The traction force is slightly reduced when camber is applied. The force reduction is most likely caused by the increase in internal friction due to carcass deformation from the camber and low inflation pressure. The braking force reaches a slightly greater value at greater negative slip ratios when camber is applied. Compare Figures 73 and 74 to Figures 69 and 70 which depict the traction and braking forces for both a cambered and un-cambered tire at 270 lbf (1201.0 N) additional normal load and 7 psi (48.3 kPa). The addition of the camber causes a significant increase in both the traction and braking force. Overall, the traction and braking forces are more sensitive to increases in inflation pressure and normal load when the tire is cambered.

The only camber settings that were tested for this study are the 0 and 8 degree settings. From the findings of Krueger [2], the test apparatus was unable to record a consistent difference in the force measurements for the intermediate camber settings.

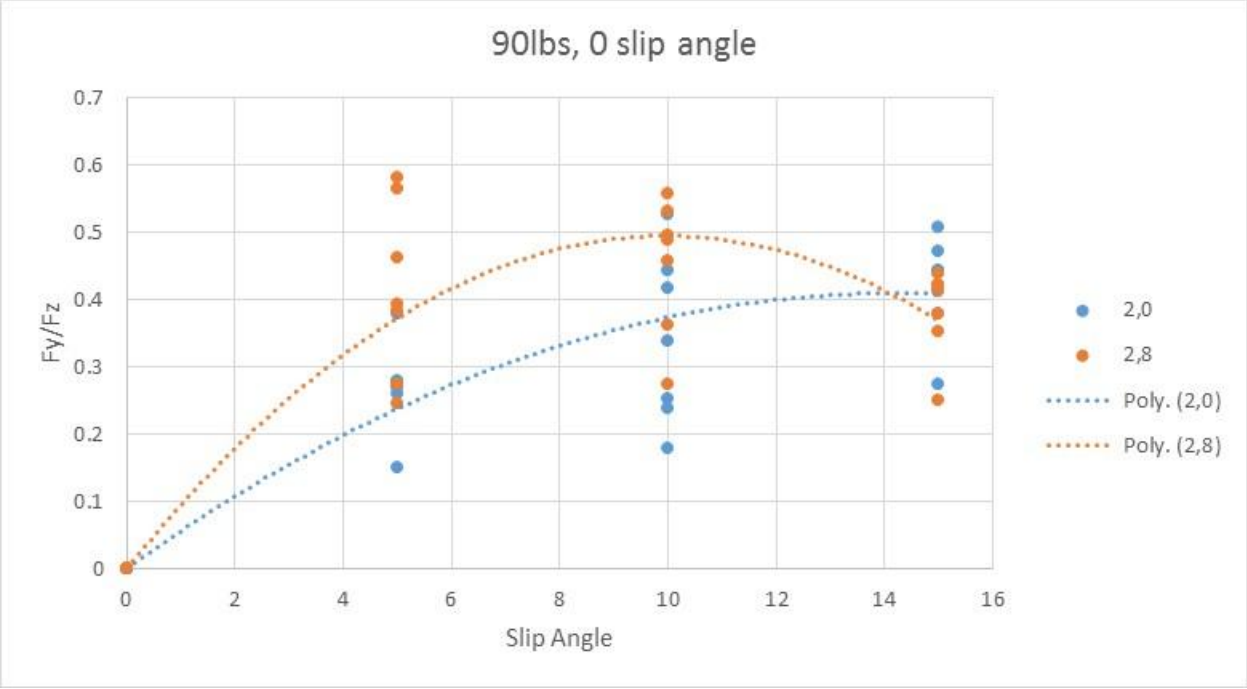

Figure 72. Change in lateral force caused by change in camber at low normal load

Figure 73. Change in traction force due to change in camber at low normal load

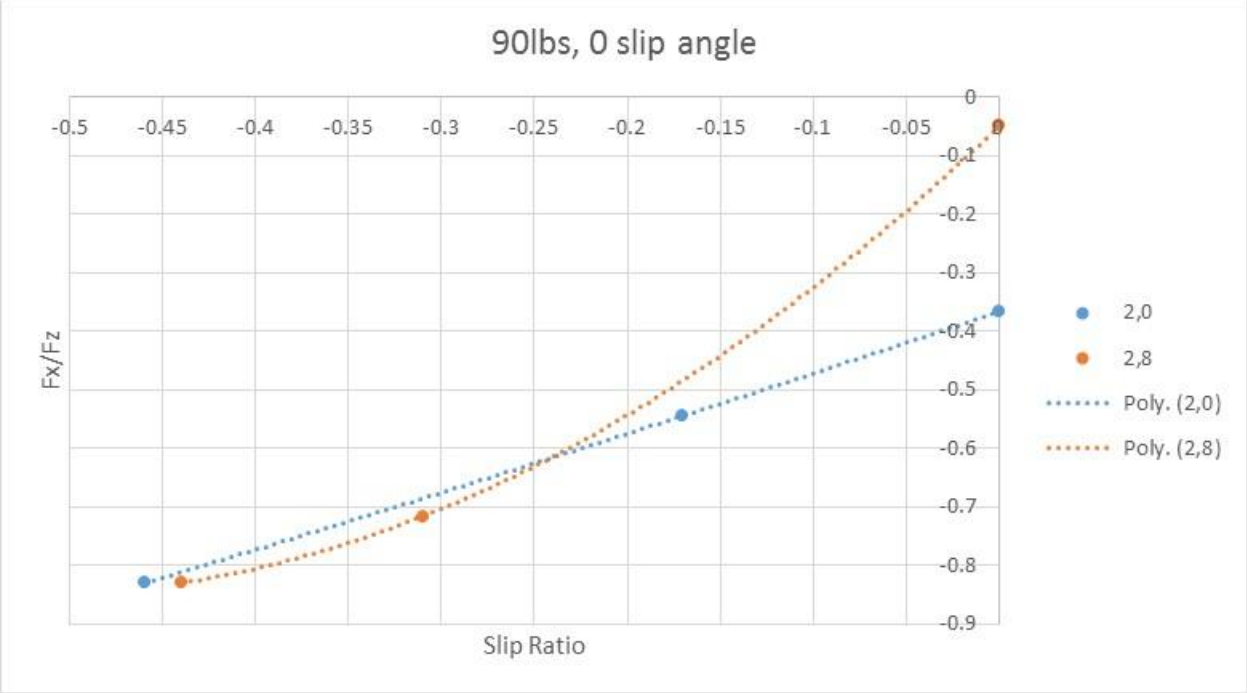

Figure 74. Change in braking force due to change in camber at low normal load

The inclinometer available for the study also possessed an error of ±5 degrees. The inclinometer's error made it difficult to accurately determine the camber angle for intermediate settings.

3.6 Cornering Stiffness

The cornering stiffness of the tire is an important parameter because it gives insight into the expected lateral performance of the tire as the slip angle is increased. The cornering stiffness also plays a significant role in a vehicle's overall handling and maneuvering characteristics. The cornering stiffness is the slope of the linear portion of the lateral force versus slip angle curves. The cornering stiffness depends on the carcass properties of the tire as well as the properties of the test surface. The amounts of traction or braking force being applied to the tire as well as changes in inflation pressure and camber also have an effect on the cornering stiffness. For the K299 tire, the inflation pressure and the camber angle were determined to cause the greatest change in the cornering stiffness. The cornering stiffness change due to applied traction was much less with approximately 1 lbf/deg (4.4 N/deg) increase for every 0.15 increase in slip ratio. The same trend was also observed for applied braking. A comparison of cornering stiffness for each inflation pressure and camber setting can be seen in Figure 75.

A greater cornering stiffness can be desirable for vehicles intended for higher speed operation. The greater the cornering stiffness, the faster the tire will respond to an increase in slip angle and the faster the lateral force will increase. The faster the lateral force increases the faster the cornering of a vehicle. A lower cornering stiffness can give a vehicle a smoother ride but will be less responsive to changes in slip angle [20].

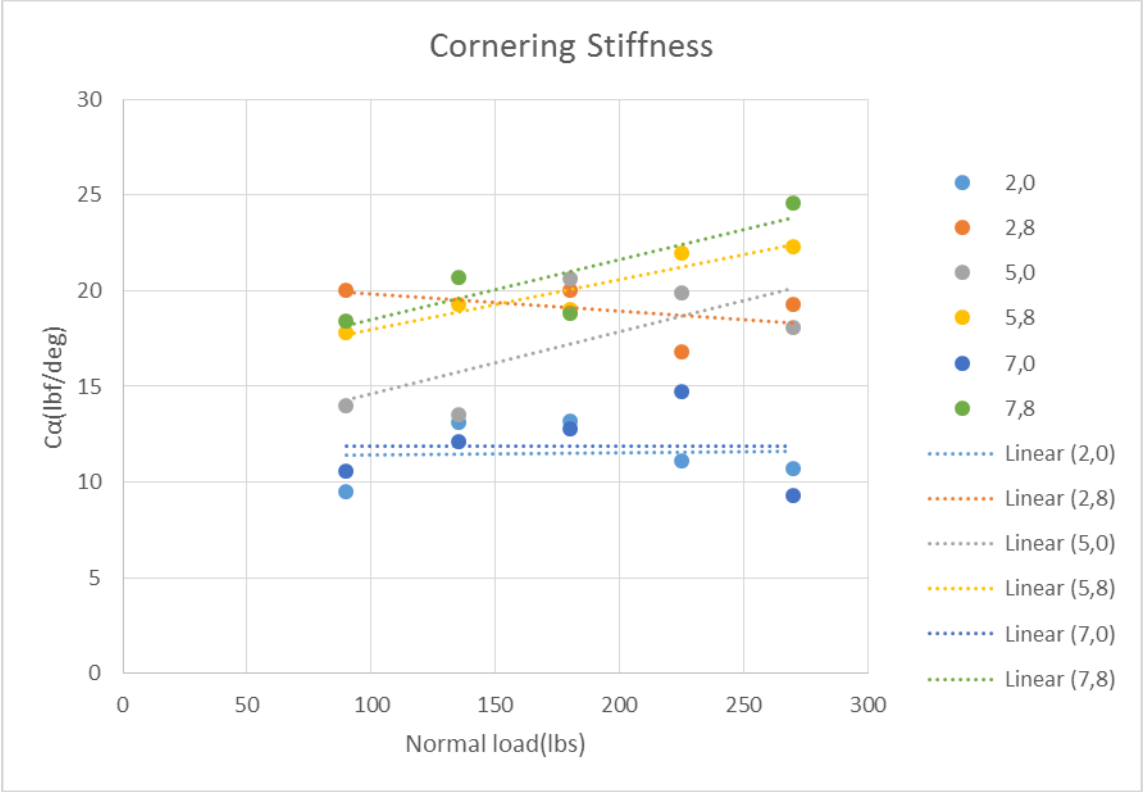

Figure 75. Changes in cornering stiffness caused by changes in inflation pressure and camber angle

The greatest cornering stiffness for the K299 occurs when it is cambered at 8 degrees. The 8 degree finding holds true for all tested normal loads and all tested inflation pressures. The effect of inflation pressure on cornering stiffness depends on the applied normal load. For normal loads up to 180 lbf (800.6 N), the 2 psi (13.8 kPa) inflation pressure has the greatest cornering stiffness values with values recorded at 5 psi (34.5 kPa) inflation pressure approximately 5-7 lbf/deg (22.2-31.1 N/deg) less. The cornering stiffness at 7 psi (48.3 kPa) tire inflation pressure for both the cambered and un-cambered tire is significantly less for the normal load range up to 180 lbf (800.6 N). The cornering stiffness at 7 psi (48.3 kPa) averaged 15-20 lbf/deg (66.7-89.0 N/deg) less than for the 2 psi (13.8 kPa) inflation pressure. The pressure relationship changed for applied normal loads of 225 lbf (1000.8 N) and greater. The 7 psi (48.3 kPa) inflation pressure

for the cambered tire produces the greatest cornering stiffness values. The next greatest values were determined at 5 psi (34.5 kPa) and 8 degrees camber. The observed trend does not, however, carry over to the un-cambered tire. The greatest cornering stiffness is found at 5 psi (34.5 kPa) inflation pressure and 0 camber. The cornering stiffness for 2 psi (13.8 kPa) and 7 psi (48.3 kPa) are very close to each other being separated by an average of 5 lbf/deg (22.241 N/deg) or less. The most likely cause for the similar behavior is the pneumatic characteristics of the tire. At low inflation pressures and high applied normal loads, the tire undergoes severe deformation resulting in increased internal friction. The carcass deformation decreases the overall force production of the tire and thus the cornering stiffness as well. The overall reduction in force output cancels any benefit that is gained from the increase in tire contact area. The observed phenomenon demonstrates the utility of adding camber for vehicles with higher normal loads. An addition of camber improves the vehicle's handling characteristics significantly above what would result from changes in tire pressure alone.

3.7 Tire Friction Ellipse

The tire friction ellipse is an excellent way to summarize all of the preceding tire force data into a single graph of tire performance. As was discussed in Chapter 1, the tire friction ellipse is a combination of the graphs of the tire’s lateral and longitudinal force data. Friction ellipse data is especially useful to vehicle designers since most off-road vehicles operational time is mostly in combined slip conditions. The combined slip conditions occur whenever a vehicle maneuvers or is pushed off course by changes in terrain.

Figure 76 depicts the friction ellipse for the un-cambered K299 tire. The vertical lines represent the forces that were recorded at constant slip angles as the slip ratio and inflation pressure are changed. The horizontal lines represent the tire forces at constant slip ratio as the slip angle and inflation pressure are changed. All of the force values were normalized by dividing by the normal load to allow direct comparison of the tire forces for each setting. The positive portion of the graph represents the tire with applied traction and the negative portion is the tire with applied braking. Only the right half of ellipse is shown because all of the applied slip angles are oriented for a right hand turn. The left half of the ellipse can be generally assumed to mirror the right half [4, 25]. The bold outermost line represents the tire's performance envelope estimated using equation 4. The performance envelope was fit to best encapsulate the maximum recorded tire forces. The coefficients of friction used in equation 5 were estimated from the best fit to the data as well. An initial inspection of Figure 76 indicates how the tire can support greater traction forces than it can braking forces. Greater traction forces are indicated by the friction ellipse being shifted up on the Y-axis. The lines of constant slip ratio also form more of a cardioid shape rather than a pure ellipse. The cardioid shape fits well with the experimental data presented by Brach and Brach [12]. It is also important to note the places where the constant slip angle lines cross the X-axis are mainly theoretical. It is almost impossible to place a tire into pure lateral slip conditions without having at least some longitudinal slip as well. The area around the X-axis should be thought of as a transitional area where the tire is switching from traction to braking. The idea of a transitional area is supported by the tendency of the data points to curl back towards the Y-axis as the X-axis is approached, which gives rise to the observed cardioid shape.

The next notable feature is the spacing of the lines of constant slip angle. The least combined forces are recorded at 7 psi (48.3 kPa) inflation pressure and the greatest are at 5 psi (34.5

kPa) inflation pressure. The 2 psi (13.8 kPa) lines fall between the 5 psi (34.5 kPa) and 7 psi (48.3 kPa) lines. The main reason for the spacing is a combination of the tire contact area and the tire's internal friction losses. Five psi (34.5 kPa) inflation pressure produces the greatest forces because it is at an optimum point for maximizing force production. The optimum point is a result of the increased contact area while still minimizing the internal friction losses caused by carcass deformation. The 7 psi (48.3 kPa) tire inflation pressure produces the least forces because, while it has the least internal frictional losses, the smaller contact area limits the tire's ability to effectively push on the ground. Two psi (13.8 kPa) tire inflation pressure produces forces between 5 psi (34.5 kPa) and 7 psi (48.3 kPa) because although it has the largest area for the traction and braking forces to be transmitted to the ground, the internal friction losses from carcass deformation are very high. The low inflation pressure prevents the tire from taking full advantage of its pneumatic characteristics.

The lines of constant slip ratio follow the same general trends that were previously noted about the pure longitudinal forces. The slip ratio lines begin on the Y-axis where the tire is in pure longitudinal slip. The combined forces then increase in a linear fashion and peak when they reach the 5 degree slip angle line for 5 psi (34.5 kPa) tire inflation pressure. The trend then decreases as the slip angle is increased to the maximum of 15 degrees. The slope of the linear portion for the constant slip ratio increases as the slip ratio is increased. The peak combined force is reached much more quickly at the greatest slip ratio. The greatest slip ratio line is also the closest to the tire's performance envelope so it is to be expected that the forces would increase at a faster rate. In physical terms, the tire at a greatest slip ratio is not capable of performing hard cornering without losing traction. The trends are very similar for both the traction and braking portions of the graph. The forces reach a peak slightly sooner when the tire is undergoing braking.

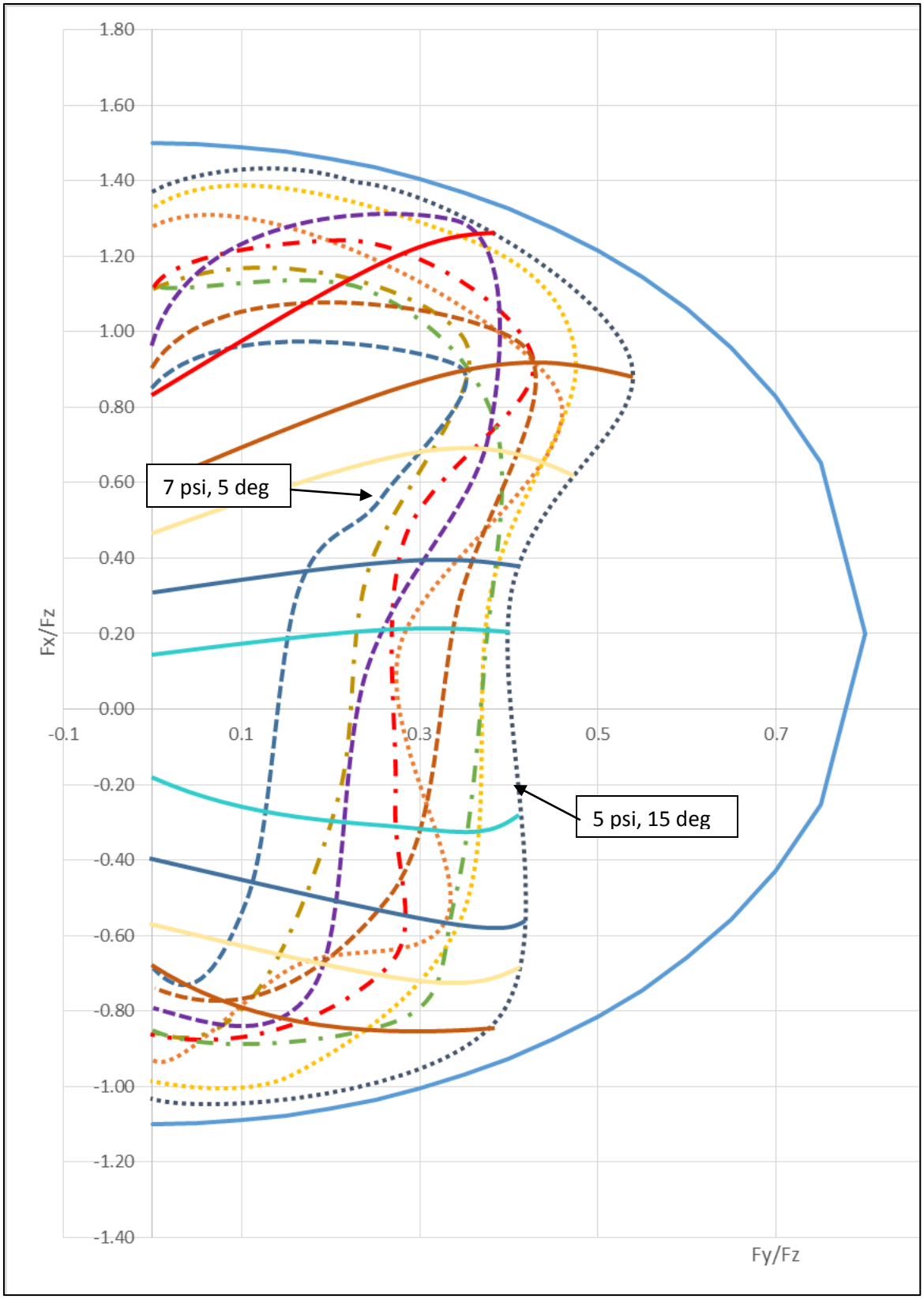

Figure 76. Friction ellipse for the un-cambered Kenda Bearclaw K299 tire

Figure 77 depicts the K299 tire friction ellipse when camber is applied to the tire. The first change that is noticed is the constant slip angle lines are now much closer together. The 5 psi (34.5 kPa) tire inflation pressure still produces the highest tire forces, but the difference with 7 psi (48.3 kPa) tire inflation pressure is now much smaller than with the un-cambered case. The increase in tire forces for the 7 psi (48.3 kPa) tire inflation pressure demonstrates how advantageous the addition of camber can be for an off-road vehicle. Applying camber also makes the tire less sensitive to changes in slip angle. The camber phenomenon can be seen in the way that the constant slip angle lines are closer together within each tire inflation pressure set. The performance envelope for the cambered case is shifted up on the Y-axis in a similar manner to the un-cambered case. The upward shift again shows that the tire can produce more force when under traction than braking before sliding occurs. Another change observed is extension of the performance envelope out the X-axis for a cambered tire. Further extension of the performance envelope indicates the cambered tire can produce more lateral force than an un-cambered tire can produce before sliding of the tire occurs. The same general cardioid shape for the lines of constant slip angle is also present. The maximum traction and braking coefficients are also greater than for the un-cambered tire.

The lines of constant slip ratio maintain similar trends to what was seen for the un-cambered tire. The main difference observed is the lines are less steeply sloped for slip ratios up to 0.4. After 0.4, the slip ratio lines display the same steep slopes as seen in the un-cambered case. The decrease in slope indicates that the combined force is not increasing as rapidly as the slip angle is increased for slip ratios less than 0.4.

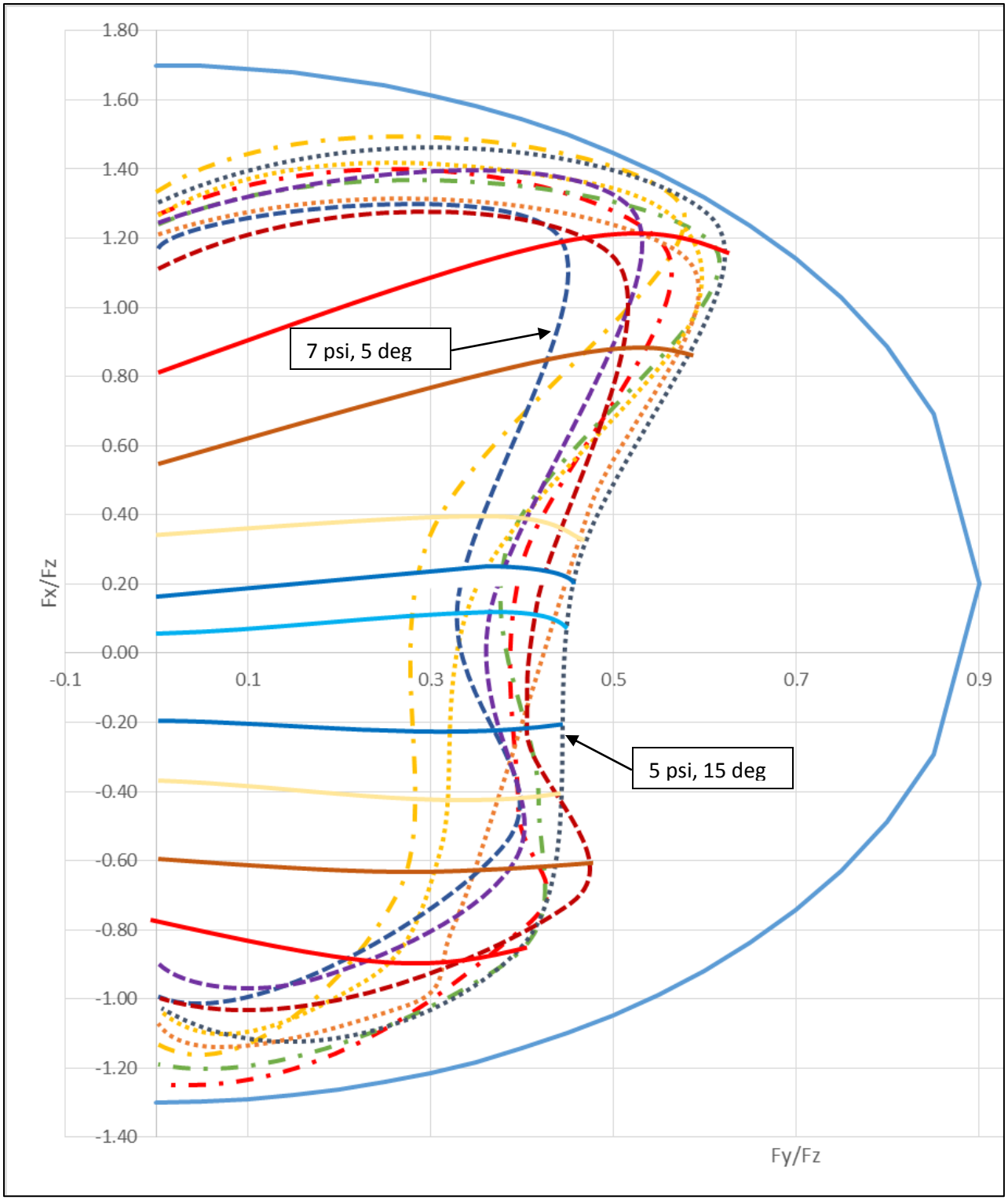

Figure 77. Friction ellipse for the cambered Kenda Bearclaw K299 tire

Chapter 4. Conclusions and Recommendations for Future Research

4.1 Conclusions

The collection and analysis of the lateral and longitudinal tire forces on a deformable surface have given greater insight into the performance of off-road vehicles. The findings of this study fit well with the conclusions of both Krueger [2] and Holloway *et al.* [1] with regards to the lateral tire forces produced by a free rolling wheel. The addition of a driven wheel in this study made possible collection of new and unique empirical data. For the first time, the effects changes in a tire inflation pressure, camber, slip angle, and normal load are discernible for an off-road tire subjected to varying positive and negative slip ratios. The study also showed the utility of using an instrumented wheel to collect both force readings and soil characteristics. Results of this study form an important basis for future research into off-road vehicle design and performance.

Results of this study have led to several conclusions about how off-road tires behave as the inflation pressure, camber angle, slip angle, and normal load are changed.

1. There is an optimum inflation pressure for a given tire that maximizes the tire contact area, and therefore the longitudinal and lateral force that can be produced, while minimizing the frictional losses due to carcass deformation. The optimum inflation pressure also extends to the tire's performance in combined slip conditions where the tire's performance envelope (the friction ellipse) was increased versus the other tested pressures. The optimum tire inflation pressure for the tested tire was found to be 5 psi (34.5 kPa).
2. The application of camber will improve the lateral and longitudinal force production for a tire with greater tire inflation pressure. Application of camber also extends to the com-

bined slip performance envelope. The addition of camber would be especially useful to a designer for improving the performance of heavier vehicles or in situations that required greater tire inflation pressures.

3. Increasing the slip angle decreases the longitudinal force coefficient, both traction and braking, when the tire is subjected to a driving torque. The expected corresponding increase and saturation point for the lateral force coefficient as the slip angle is increased is present and remains during both traction and braking. The Kenda Bearclaw K299 reaches its lateral force saturation point at approximately 15 degrees slip angle.
4. The normal load contributes most significantly to the tire force production by increasing the tire contact area by forcing the tire carcass to deform as the load is increased.
5. The normal load also reduces the traction, braking and lateral force coefficients as the load is increased.

Constructing a plot of a tire friction ellipse of an off-road tire on a deformable surface is a significant contribution to engineering knowledge of performance and design criteria of off-road vehicles. As was stated by Milliken [4], the data of this type is very rare for any type of vehicle. To date, the friction ellipses depicted in this study are the only ones that have been constructed for a tire operating on a deformable surface. Two important conclusions were drawn from examining the friction ellipses. First, the tire was able to produce a sustainable traction coefficient on the test surface that was higher than the maximum braking coefficient that could be achieved. Second, the tire was able to produce more longitudinal force overall on the test surface than lateral force. Further research will need to be conducted to determine the exact contribution from tire design and surface properties. The friction ellipses created from this study's data will provide

an important starting point for continued research into the behavior and performance of off-road tires.

The properties of the test soil surface were also a significant contributor to the tire's overall behavior. The soil surface limited the amount of traction and braking torque that could be applied. If too much of either was used, the tire would displace large amounts of the soil in the contact patch and no usable traction or braking force would be produced. The lateral force was also influenced by the soil properties. At high slip angles (>20 deg), the tire would cease rolling and would begin to dig a furrow similar to a plow. When this occurs, the controllability of the tire is severely reduced and may be lost altogether. The softer the soil, the more likely the digging scenario will occur. The exact influence of soil properties on tire forces would have to be obtained by conducting tire tests on surfaces with different soil types which was beyond the scope of this research. Each surface of different soil type will require the entire testing matrix be repeated to ensure sufficient data is collected.

The gross traction method of determining the surface properties proved to be both effective and easy to implement when utilizing an instrumented test wheel to record the tire forces. The gross traction method allowed the data necessary to determine the surface properties to be collected and analyzed using similar methods that were applied to the tire force data. Utilized in this way, the gross traction method eliminated the need for a separate surface property measurement device and simplified the amount of mathematical analysis that was necessary to extract the desired values. The gross traction method is highly recommended for use in future research involving an instrumented test wheel on natural surfaces.

4.2 Recommendations for Future Research

The research that was conducted on off-road tire forces in this study is by no means comprehensive. The main goal of this research was to broaden the understanding of how the different tire characteristics studied affected tire performance when a torque was applied to the wheel. There are still a multitude of avenues for future research into this topic.

The most straight forward approach to future research would be to continue with the tire test apparatus as it is and conduct the test matrix again on surfaces of different soil types as well as with different makes and models of tires. Data collection would allow for comparison of the effects of surface properties in addition to effects that tire design characteristics, as tread design and profile, have on lateral and longitudinal forces. Future research would be facilitated as the test apparatus and surface characterization method is already well established and only new test surfaces and test tires would need to be located or acquired.

Creation of a larger tire test apparatus that allows for the testing of large vehicle tires would also be an important avenue to follow. The testing of larger tires would allow a researcher to more thoroughly investigate the effects that higher normal load has on force production. The tests of larger tires will show if the conclusions reached in this study pertain to larger off-road vehicles or if there is a point where the trends will change once the normal load is high enough. A larger test apparatus could also be designed to be self-propelled to do away with the tow vehicle and possibly incorporate design features that would speed up testing. Additionally, designing a new apparatus will allow for the incorporation of a more accurate measurement of camber angle. Measuring the angle more precisely would facilitate moving beyond categorizing the data as greater or lesser camber.

An investigation of a refined empirical tire model could be pursued incorporating results of this study and previous studies. The tire model could potentially be used for tire and vehicle design, and it could also be used to facilitate further analysis into tire force data collected in the future. Development of a usable model could also make it easier to compare and incorporate data collected from past studies.

Another research possibility lies with investigating the effects that soil surface properties have on the tire force production in more depth. Especially useful would be development of a procedure or device that would allow a tire to be tested on a controlled deformable surface analogous to the Flat-Trac machine described in Chapter 1. Control over surface properties would greatly simplify the problem of determining exactly what is occurring at the tire soil surface interface. Such a device or process would also help to further diminish the experimental uncertainty inherent in testing on natural surfaces.

References

1. Holloway, D.C., Wilson, W.H., Drach, T.J. "Examination of ATV Tire Forces Generated on Clay, Grass, and Sand Surfaces", Society of Automotive Engineers, Warrendale, PA, 1989
2. Krueger, D. R., *Investigation of Lateral Performance of an ATV Tire on Natural, Deformable Surfaces*, M.S. Thesis, Auburn University, Auburn, AL, 2010
3. Milliken, W. F., Milliken, D. L., *Race Car Vehicle Dynamics*, Society of Automotive Engineers, Warrendale, PA, 1995
4. Plackett, C. W., "A Review of Force Prediction Methods for Off-road Wheels", *Journal of the British Society of Research in Agricultural Engineering* vol. 31, 1985
5. Smith, N. D., "Understanding Parameters Influencing Tire Modeling", Colorado State University, Fort Collins, CO, 2004
6. Wong, J. Y., *Theory of Ground Vehicles*, John Wiley and Sons, New York, 1978
7. Pacejka, H. B., *Tire and Vehicle Dynamics* 2nd ed., Society of Automotive Engineers, Warrendale, PA, 2006
8. Shoop, S. A., "Three Approaches to Winter Traction Testing", US Army Corps of Engineers, Cold Regions Research and Engineering Laboratory, Hanover, NH, 1993
9. El-Razaz, A. S. A., *Lateral Tyre Forces on Off-road Surfaces*, University of Leeds, Leeds, United Kingdom, 1988
10. Bekkar, M. G., *Off-the-road Locomotion: Research and Development in Terramechanics*, The University of Michigan Press, Ann Arbor, MI, 1960

11. van Ginkel, J., *Estimating the Tire-road Friction Coefficient Based on Tire Force Measurements*, M.S. Thesis, Delft University of Technology, Delft, The Netherlands, 2014
12. Brach, R., Brach, M., "The Tire Force Ellipse (Friction Ellipse) and Tire Characteristics", Society of Automotive Engineers, Warrendale, PA, 2011, doi: 10.4271/2011-01-0094
13. Ageikin, I. S., *Off-the-road Wheeled and Combined Traction Devices*, Amerind Publishing Co. Pvt. Ltd., New Dehli, India, 1987
14. Holtz, R. D., Kovacs, W. D., Sheahan, T. C., *An Introduction to Geotechnical Engineering* 2nd ed., Pearson Education Inc., Upper Saddle River, NJ, 2011
15. Wong, J. Y., *Terramechanics and Off-road Vehicles*, Elsevier, Amsterdam, The Netherlands, 1989
16. Shoop, S. A., "Terrain Characterization for Trafficability", US Army Corps of Engineers, Cold Regions Research and Engineering Laboratory, Hanover, NH, 1993
17. Karafiath, L. L., Nowatzki, E. A., *Soil Mechanics for Off-road Vehicle Engineering*, Trans Tech Publications, Clausthal, Germany, 1978
18. Shoop, S. A., "Comparison of Thawing Soil Strength Measurements for Predicting Vehicle Performance", US Army Corps of Engineers, Cold Regions Research and Engineering Laboratory, Hanover, NH, 1992
19. Okello, J. A., "A Review in Soil Strength Measurement Techniques for Prediction of Terrain Vehicle Performance", *Journal of the British Society of Research in Agricultural Engineering* vol. 50, 1991
20. Dixon, J. C., *Tires, Suspension, and Handling* 2nd ed., Society of Automotive Engineers, Warrendale, PA, 1996

21. Kenney, J. F., Keeping, E. S., *Mathematics of Statistics, Pt. 1, 3rd ed.* Princeton, NJ, 1962

22. Young, R. N., Ezzat, F. A., Skiadas, N., *Vehicle Traction Mechanics*, Elsevier, Amsterdam, The Netherlands, 1984

23. Shoop, S. A., "Precision Analysis and Recommended Test Procedures for Mobility Measurements Made with an Instrumented Wheel", US Army Corps of Engineers, Cold Regions Research and Engineering Laboratory, Hanover, NH, 1992

24. Richomd, P. W., Shoop, S. A., Blaisdell, G. L., "Cold Regions Mobility Models", US Army Corps of Engineers, Cold Regions Research and Engineering Laboratory, Hanover, NH, 1995

25. Nuthong, C., Regelungstechnik S., *Estimation of Tire-Road Friction Forces using Kalman Filtering for Advanced Vehicle Control*, Budeswehr University, Munich, Germany, 2008

26. Crolla, D. A., El-Razaz, A. S. A., "A Review of the Combined Lateral and Longitudinal Force Generation of Tyres on Deformable Surfaces", *Journal of Terramechanics* vol. 24, 1987

27. Svendenius, J., *Tire Modeling and Friction Estimation*, M.S. Thesis, Lund University, Lund, Sweden, 2007

Appendix A. Matlab Tire Force Analysis Program

```
%Tire force data reduction program
clear
%Import raw data from the data collector memory card
[ndata,tdata,rdata]=xlsread('dataruns.xlsm');
%Place data in arrays
nruns=length(tdata);
alpha=ndata(:,1);
fz=ndata(:,2);
tirepress=ndata(:,3);
traction=ndata(:,4);
n=1;
i=1;
fxadd=zeros(nruns);
fyadd=zeros(nruns);
%Convert voltage readings into lbf
while n<=nruns
    filename=char(tdata(n));
    volt=csvread(filename,3,0);
    ch5=volt(:,1);
    ch6=volt(:,2);
    ch7=volt(:,3);
    vscale=(.003*10)/500;
    ch5lbs=ch5/vscale;
    ch6lbs=ch6/vscale;
    ch7lbs=ch7/vscale;
    %Coordinate transfrom from vehicle frame to tire frame
    fx=-ch5lbs*cosd(alpha(n))-ch7lbs*cosd(alpha(n))-ch6lbs*sind(alpha(n));
    fy=ch5lbs*sind(alpha(n))+ch7lbs*sind(alpha(n))-ch6lbs*cosd(alpha(n));
    while i<=length(fx)
        fxraw(n,i)=fx(i);
        fyraw(n,i)=fy(i);
        i=i+1;
    end
    i=1;
    %Calculate max, min, mean, and mode for fx and fy
    rundataraw(n,1)=max(fx);
    rundataraw(n,2)=mean(fx);
    rundataraw(n,3)=mode(fx);
    rundataraw(n,4)=min(fx);
    rundataraw(n,5)=max(fy);
    rundataraw(n,6)=mean(fy);
    rundataraw(n,7)=mode(fy);
    rundataraw(n,8)=min(fy);
    n=n+1;
    clear volt ch5 ch6 ch7 fx fy;
end
%First attempt at filtering data, results needed improvement
lowerb=5;
j=1;
k=1;
m=1;
while j <= nruns
    while k <= length(fxraw)
        if abs(fxraw(j,k)) >= lowerb
```

```
        fxfilter(j,m)=fxraw(j,k);
        m=m+1;
        end
        k=k+1;
    end
    k=1;
    j=j+1;
    m=1;
end
j=1;
k=1;
m=1;
while j <= nruns
    while k <= length(fyraw)
        if abs(fyraw(j,k)) >= lowerb
        fyfilter(j,m)=fyraw(j,k);
        m=m+1;
        end
        k=k+1;
    end
    k=1;
    j=j+1;
    m=1;
end
n=1;
j=1;
while n <= nruns
    while fxfilter(n,j)~=0 & j<length(fxfilter)
        fxadd(n)=fxadd(n)+fxfilter(n,j);
        j=j+1;
    end
fxavg(n)=fxadd(n)/j;
fxmax(n)=max(abs(fxfilter(n,:)));
fxmin(n)=min(abs(fxfilter(n,:)));
fxmode(n)=mode(fxfilter(n,:));
n=n+1;
j=1;
end
n=1;
j=1;
while n <= nruns
    while fyfilter(n,j)~=0 & j<length(fyfilter)
        fyadd(n)=fyadd(n)+fyfilter(n,j);
        j=j+1;
    end
fyavg(n)=fyadd(n)/j;
fymax(n)=max(abs(fyfilter(n,:)));
fymin(n)=min(abs(fyfilter(n,:)));
fymode(n)=mode(fyfilter(n,:));
n=n+1;
j=1;
end
n=1;
%Improved data filtering utilizing Matlab's built in 1-D filter
windowsize=100;
while n<=nruns
    filterx(n,:)=filter(ones(1,windowsize)/windowsize,1,fxraw(n,:));
```

```
    filtery(n,:)=filter(ones(1,windowsize)/windowsize,1,fyraw(n,:));
    n=n+1;
end
n=1;
while n<=nruns
    fymax(n)=max(abs(filtery(n,:)));
    fymin(n)=min(abs(filtery(n,:)));
    fymode(n)=mode(filtery(n,:));
    n=n+1;
end
n=1;
while n<=nruns
    fxmax(n)=max(abs(filterx(n,:)));
    fxmin(n)=min(abs(filterx(n,:)));
    fxmode(n)=mode(filterx(n,:));
    n=n+1;
end
n=1;
%Produces the plots that were used to find the maximum and average force
%values
while n<=nruns
    figure(n)
    plot(filterx(n,:))
    title(char(tdata(n)))
    n=n+1;
end
```

Appendix B. Test Surface Location

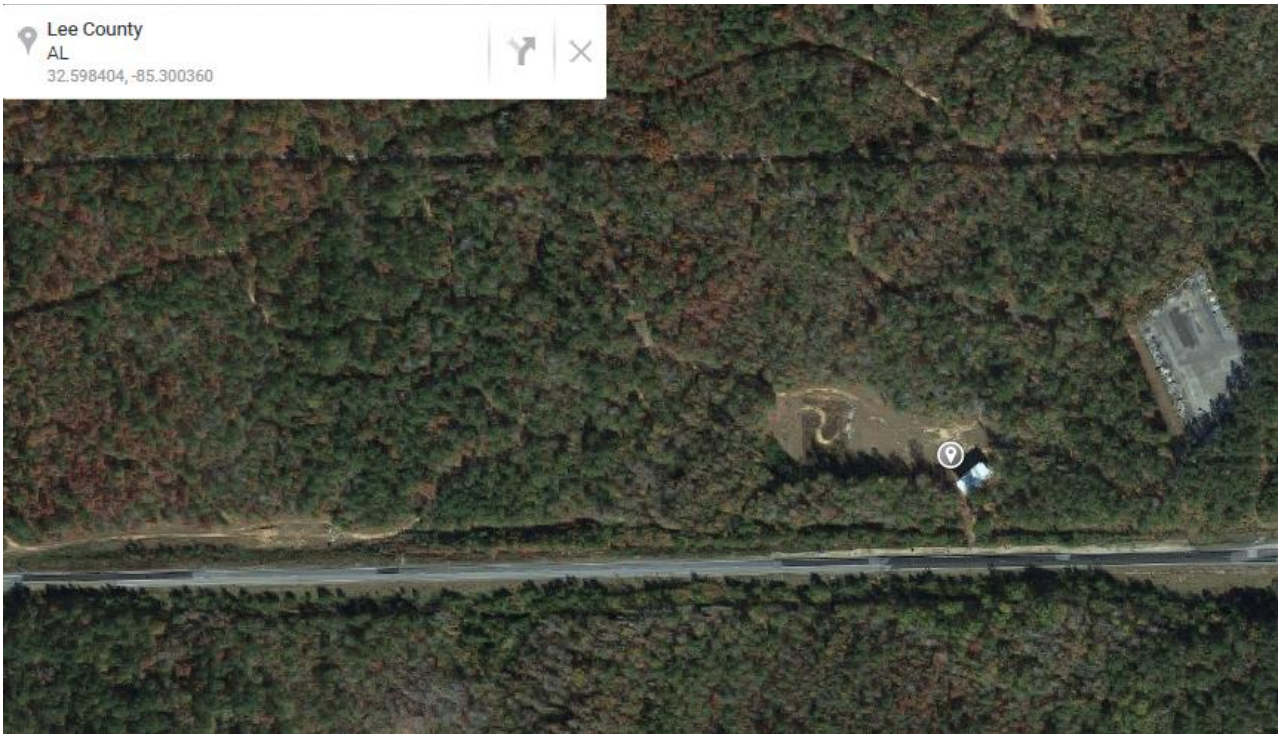

The test surface for the study is located at the National Center of Asphalt Technology in Lee County, Alabama. The test surface coordinates are 32.598° N 85.300°W. The soil in the area is the silty clay typically found throughout the Southeastern United States. Satellite imagery was taken from Google Earth.